UNIVERSITY OF VERONA

DEPARTMENT OF

BIOTECHNOLOGY

PHD SCHOOL

SCIENCE AND ENGINEERING

PHD IN

NANOSCIENCE AND ADVANCED TECHNOLOGIES

CYCLE / YEAR of initial enrolment   35th/2019

PHD THESIS TITLE

SYNTHESIS AND LUMINESCENCE SPECTROSCOPY OF INORGANIC MATERIALS DOPED WITH RARE EARTH IONS

S.S.D. (Disciplinary Sector) CHIM/03
(it is compulsory to indicate the disciplinary sector that the thesis comes under)*

Coordinator: Prof. Adolfo Speghini

Signature _____

Tutor: Prof. Fabio Piccinelli (ex Marco Bettinelli)
Signature _____

PhD candidate: Xiaowu Hu

Signature _____

Synthesis and luminescence spectroscopy of inorganic materials doped with rare earth ions –

Xiaowu Hu

PhD thesis

Verona, 6 March 2023

ISBN

RIASSUNTO

Matrici inorganiche drogate con ioni di terre rare sono sempre stati negli ultimi tempi un tema di ricerca molto diffuso a causa delle loro ampie applicazioni, ad esempio nella produzione di ceramiche trasparenti luminescenti, catalizzatori, sensori ottici di temperatura, materiali luminescenti per anticontraffazione, nonché diodi emettitori di luce bianca. Il trasferimento di energia che coinvolge gli ioni di terre rare trivalenti in questi solidi inorganici è stato, ed è tuttora, un campo fondamentale nella moderna ricerca sulla luminescenza, che svolge un ruolo essenziale nel migliorare le prestazioni ottiche del materiale.

I processi di trasferimento di energia sono stati intensamente studiati dall'inizio degli anni '60 e il contributo fornito dal professor George Blasse è stato prezioso per l'avanzamento della comprensione del trasferimento di energia e dei processi di migrazione che coinvolgono ioni luminescenti. In particolare, il Prof. Blasse ha studiato in dettaglio la migrazione dell'eccitazione in materiali concentrati, in particolare basati su Gd^{3+}, Eu^{3+} e Tb^{3+}. Tuttavia, questo tema attira ancora molta attenzione a causa di domande senza risposta sui meccanismi in gioco e sulle applicazioni tecnologiche di questo processo.

In questa tesi, i processi di trasferimento di energia dei tipi $Tb^{3+} \rightarrow Nd^{3+}$ e $Tb^{3+} \rightarrow Sm^{3+}$ sono stati studiati a temperatura ambiente in materiali a doppio fosfato di eulitite con stechiometria $Sr_3Tb_{0.99}Nd_{0.01}(PO_4)_3$ e $Sr_3Tb_{0.99}Sm_{0.01}(PO_4)_3$. Come già trovato per $(Ba,Sr)_3Tb_{1-x}Eu_x(PO_4)_3$, il trasferimento dell'energia di eccitazione dal Tb^{3+} al drogante è assistito da una migrazione di energia molto rapida nel sottoreticolo di ioni Tb^{3+} che implica il coinvolgimento dello stato eccitato $^5D_4$. Per questo motivo, l'efficienza di trasferimento è elevata rispetto a quanto osservato in altri casi. La presente indicazione dovrebbe chiaramente essere corroborata da dettagliati calcoli teorici.

Inoltre, la stechiometria $Sr_3Y_{1-x-y}Tb_xTm_y(PO_4)_3$ è stata studiata per esplorare i processi di trasferimento di energia che coinvolgono gli ioni Tb^{3+} e Tm^{3+}. Ha rivelato che il trasferimento di eccitazione $Tb^{3+}-Tm^{3+}$ potrebbe estinguere fortemente il livello $^5D_4$ di Tb^{3+} e che i processi interni di rilassamento incrociato $Tm^{3+} - Tm^{3+}$ avrebbero avuto luogo all'eccitazione nel livello emissivo $^5D_4$ (Tb^{3+}).

Uno studio dettagliato dei campioni di $LaInO_3:Bi^{3+}/Tb^{3+}$ e $LaInO_3:Tb^{3+}/Eu^{3+}$ doppiamente drogati e $LaInO_3:Bi^{3+}/Tb^{3+}/Eu^{3+}$ triplamente drogati ha rivelato che il trasferimento di energia $Bi^{3+} \rightarrow Tb^{3+}$ è dominato dai meccanismi di dipolo elettrico-dipolo elettrico (EDD) e che la

massima efficienza di trasferimento di energia può essere raggiunta aumentando la concentrazione di ioni lantanidi (Tb^{3+} e Eu^{3+}). La compresenza di luce colorata blu, verde e rossa nel giusto rapporto per ottenere luce bianca, è assicurata regolando le efficienze di trasferimento di energia $Bi^{3+} \rightarrow Tb^{3+}$ e $Tb^{3+} \rightarrow Eu^{3+}$. A loro volta, queste efficienze sono fortemente correlate alla quantità relativa dei tre ioni droganti e quindi alle loro distanze di interazione.

I materiali fluorurati sono considerati delle matrici interessanti per ospitare ioni lantanidi luminescenti grazie al loro alto indice di rifrazione, alla bassa energia fononica (< 350 cm^{-1}) e all'eccellente stabilità termica. I meccanismi di trasferimento di energia $Tb^{3+} \rightarrow Eu^{3+}$ sono stati esplorati nei campioni $NaBi_{1-x-y}Tb_xEu_yF_4$, ed è stato trovato che l'efficienza del trasferimento di energia è facilmente influenzata dai gruppi di quenching sulla superficie delle nanoparticelle. Inoltre, sono state proposte prestazioni di rilevamento della temperatura superiori per i campioni. Pertanto, i materiali potrebbero essere un candidato promettente per la determinazione del contenuto di acqua nei solventi organici e per la termometria ottica.

Il complicato sistema di meccanismi di trasferimento di energia consente un'esplorazione senza fine nel futuro. Anche con i frutti finora ottenuti si è dato un enorme contributo al miglioramento dell'intensità della luminescenza, alla regolazione dell'emissione del colore, nonché al raggiungimento della luce bianca. Ad ogni modo, il trasferimento di energia come fenomeno affascinante nei materiali luminescenti è vantaggioso per vari aspetti della nostra vita.

ABSTRACT

Inorganic hosts doped with rare earth ions have always been in recent times a research hotspot because of their broad applications, such as: luminescent transparent ceramics, catalyst, optical temperature sensor and fluorescent anti-counterfeit materials, as well as white light emission diodes and so on. The energy transfer involving trivalent rare earth ions in these inorganic solids has been and still is a fundamental field in modern luminescence research, which plays an essential role in improving luminescence performance.

The area of energy transfer has been intensively studied since the early 1960's, and the contribution provided by Professor George Blasse has been crucial for the advancement of the understanding of energy transfer and migration processes involving luminescent ions. Particularly, Prof. Blasse studied in detail the migration of excitation energy in concentrated materials, especially based on Gd^{3+}, Eu^{3+} and Tb^{3+}. But it still attracts a lot of attention due to unanswered questions regarding the mechanisms at play, and the technological applications of this type of process. For this reason, several studies have been performed here.

(a) Energy transfer processes of the types $Tb^{3+} \rightarrow Nd^{3+}$ and $Tb^{3+} \rightarrow Sm^{3+}$ have been studied at room temperature in eulytite double phosphate materials with stoichiometry $Sr_3Tb_{0.99}Nd_{0.01}(PO_4)_3$ and $Sr_3Tb_{0.99}Sm_{0.01}(PO_4)_3$. As already found for $(Ba,Sr)_3Tb_{1-x}Eu_x(PO_4)_3$, the transfer of excitation from the Tb^{3+} to the dopant is assisted by very fast energy migration in the $^5D_4$ subset of levels, and effectively occurs between nearest neighbor ions. It is for this reason that the transfer efficiency results to be compared to what observed in other hosts.

(b) The stoichiometry $Sr_3Y_{1-x-y}Tb_xTm_y(PO_4)_3$ have been studied to explore the energy transfer processes involving the Tb^{3+} and Tm^{3+} ions. It revealed that the $Tb^{3+} \rightarrow Tm^{3+}$ transfer of excitation could quench strongly the $^5D_4$ level of Tb^{3+}, and internal $Tm^{3+} \rightarrow Tm^{3+}$ cross relaxation processes would take place upon excitation in the emissive $^5D_4$ (Tb^{3+}) level.

(c) A detailed study of doubly doped $LaInO_3$: Bi^{3+}/Tb^{3+} and $LaInO_3$: Tb^{3+}/Eu^{3+} and triply doped $LaInO_3$: $Bi^{3+}/Tb^{3+}/Eu^{3+}$ samples showed that the $Bi^{3+} \rightarrow Tb^{3+}$ energy transfer is dominated by electric dipole- electric dipole (EDD) mechanisms, and the largest energy transfer efficiency can be achieved through increasing the concentration of lanthanide ions (Tb^{3+} and Eu^{3+}). The co-presence of blue, green, and red color light in the right ratio to obtain white light, is ensured by tuning the $Bi^{3+} \rightarrow Tb^{3+}$ and $Tb^{3+} \rightarrow Eu^{3+}$ energy transfer efficiencies. In turn, these efficiencies

are strongly related to the relative amount of the three dopant ions and therefore to their interaction distances.

(d) Fluoride materials have been broadly exploited as convenient hosts for rare earth dopant ions due to their high refractive index, low phonon energy (<350 cm^{-1}) as well as excellent thermal stability. The energy transfer mechanisms $Tb^{3+} \rightarrow Eu^{3+}$ ions have been explored in samples $NaBi_{1-x-y}Tb_xEu_yF_4$, and it has been found the energy transfer efficiency is easily influenced by the quenching groups on the surface of nanoparticles. Also, the superior temperature sensing performance for samples has been proposed. Therefore, the materials could be a promising candidate for determination of water content in organic solvents as well as optical thermometry.

(e) Taking advantage of the outstanding merits belonging to $CaAl_2O_4$: Eu, Nd (CAO) persistent phosphors, such as long-lasting afterglow as well as unique luminescence spectra, it was adopted as excitation source to irritate $Y_3Al_5O_{12}$: Ce phosphors. Based on this fact, one desired yellow emission persistent phosphor has been achieved by depositing these two kinds of phosphors as a polymer layer with a certain thickness. The process of radiative energy transfer from CAO to YAG has been indicated.

The complicated energy transfer mechanisms system allows an endless exploration in the future. Even with the results obtained so far, an enormous contribution towards the improvement of luminescence intensity, the regulation of emission color, as well as the achievement of white light have been made. Anyway, energy transfer as a fascinating phenomenon in luminescent materials, is beneficial for various aspects in our life.

Contents

Chapter 1

INTRODUCTION

1. Luminescence is seen everywhere

One question raised is 'are you familiar with luminescence?', the answer is no for most people. However, a quite affirmative answer when it comes to light, and sunlight is the first one that comes to mind naturally. As Southey who is a poet wrote, "It's sunlight that turns darkness into something pleasant", and sunlight is truly powerful energy and can light up the whole world. But the sunlight is not always there, the darkness brought by night makes another form of light is needed, that is related to luminescence. Over the past decades, luminescent materials have been increasingly developed and commercialized, like solid state lighting and LED displays. Besides, even many daily electronic products, such as mobile phone, TV set as well as computer; the commercial usage like shining billboard signs for advertising in street, and colorful architectural design; the medical fields, for instance, tumor detection and multimodal imaging. Of course, other closely related areas including anti-counterfeiting and agricultural production, all involve the application of luminescence. Although luminescence has been applied in a variety of realms, it still has potential benefits that need to be developed urgently, which requires us to pay more attention to the development and innovation of luminescence.

The production of luminescence involves the conversion of various types of energy into light. For example, the photoluminescence is due to the conversion of electromagnetic radiation, the cathodoluminescence is caused by energetic electrons, the chemiluminescence is a consequence of conversion with chemical reaction, the energy conversion in other forms could refer to references [1]. Particularly, photoluminescence is the main topic concerning this thesis. The in-depth process includes the absorption of excitation energy and emission of light, as shown in Fig.1 one transition from the initial (I) to final (F) states would take place after the excitation of luminescent center, which followed by a radiative (R) and non-radiative (NR) relaxation to the final state, and the emission light is the result of radiative transition [1].
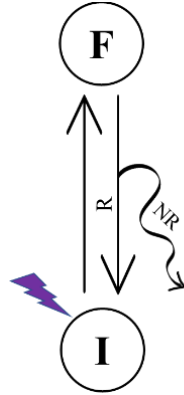
Fig. 1. The general process of light production.

2. Inorganic luminescent materials

The composition of inorganic luminescent materials generally contains two parts, namely host and dopant. Wherein, the host is the basic part of the material and plays a major role in yielding luminescence. It can not only provide certain lattice surrounding for dopant, but also in special cases absorb the incident radiation and transfer it to the activator ions, various kinds of hosts include oxides, sulfides, silicates, aluminates, phosphates and so on. Although some hosts could emit light alone, very few of them used for luminescent materials are capable of light emission independently. When it comes to this issue, we must mention another significant part, that is, dopant, which is a kind of component incorporated purposely into host. It can be roughly classified into two categories, and they are activator (A) and sensitizer (S).

The activator usually plays the role of luminescent centers in inorganic luminescent materials, and it can absorb the exciting radiation and emit specific luminescence. The common activators could be the transition metal and rare earth ions. The luminescent properties, such as spectral shape and luminescence intensity, can be greatly influenced by activators. Particularly, an excessive amount of activator can give rise to concentration quenching phenomenon, which is harmful for luminescence intensity. Thus, care should be taken to avoid it, and an optimal doping concentration is demanded. It has been stated that the mechanisms concerning concentration quenching consist of several processes. One is associated with the energy migration to killers in the cases of Eu^{3+} and Tb^{3+}, and cross relaxation is involved in Sm^{3+} and Dy^{3+}, but the situation of other remaining elements is in the middle [2]. With the purpose of advancing luminescent properties, sensitizer could be additionally doped with activator, which can greatly enhance the luminescence intensity as well as regulate the emission color. In this case, the sensitizer bears

2

primary responsibility for the absorption of excitation light, then energy transfer from sensitizer to activator happens as shown in Fig. 2, which results in the emission from activator even if it does not absorb any exciting radiation [3].
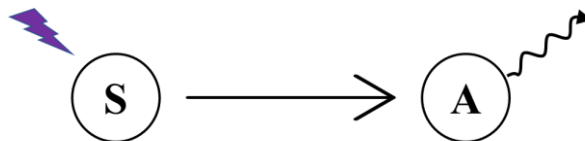
Fig. 2. An overview of the energy transfer from sensitizer to activator.

3. Lanthanide doped inorganic luminescent materials

As an important class of inorganic luminescent materials, lanthanide doped inorganic luminescent ones have attracted a lot of attention and are worthy of exploration. They possess striking luminescent properties because of the unique electronic configuration of rare earth elements. Generally, the scope of rare earth contains 17 elements as displayed in Fig. 3, which features with electronic configuration $[Xe]4f^n5d^m6s^2$ (n = 1-14 and m = 0 or 1) [4]. The luminescence could result from Ln^{2+} and Ln^{3+} ions, but Ln^{3+} ion with electronic configuration $[Xe]4f^n$ dominates the luminescence in this thesis. Particularly, Sc^{3+}, Y^{3+} and La^{3+} as well as Lu^{3+} can not emit light because of their special closed-shell, and thus they are most used for host component. Yet other remaining elements are capable of different color emission, some of them showing broad band emission stemming from the 4f-5d transitions, example is Ce^{3+} ion. However, most emissions are line shaped, which is mainly associated with 4f-4f transitions. Because 4f electrons are situated in shielded orbitals, therefore, the interference from surroundings like electric field, magnetic field and crystal coordination could be avoided. As a result, parallel potential energy curves are involved in configurational coordinate diagram [5], a sharp line emission thus can be observed.
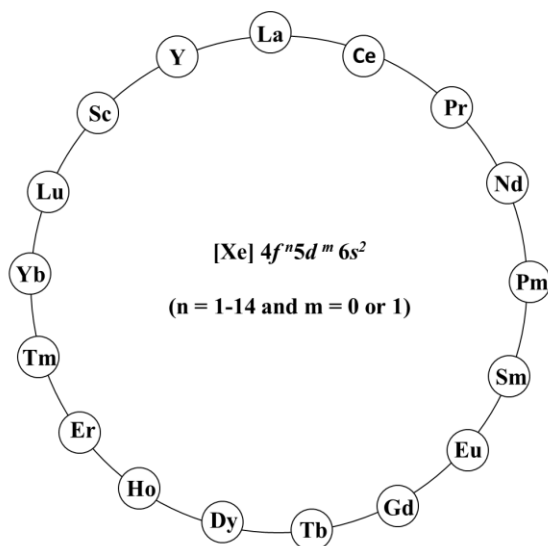
Fig. 3. A schematic diagram of a Ferris wheel-shaped 17 rare earth elements.

Besides, lanthanide doped inorganic luminescent material has a great significance in the historical evolution of the optical discipline. Since the 1950's, the development of red-emission phosphors Y(P,V)O$_4$: Eu, Y$_2$O$_3$: Eu and Y$_2$O$_2$S: Eu [6]–[8] for fluorescent lamps and LEDs, as well as the rapid growth of rare earth ions doped persistent [9]–[12] and up-conversion luminescent materials [13]–[16], which remarkably expands its application scale. At the beginning of the 21st century, white light LEDs were highly sought after, which created another research boom [17]–[21]. At present, a variety of lanthanide doped inorganic luminescent materials have been researched, and a wide application has been achieved as well. Meanwhile, the vigorous development of lanthanide doped inorganic luminescent material is one of the best paths to highlight the value of rare earth ions.

4. Energy transfer: a fascinating phenomenon in luminescent materials

Energy transfer process as a very interesting phenomena has multiple ranges of application, some typical examples are fluorescent lamps, dyes, and pigments as well as photosynthesis. With the development of technology, some innovative properties are introduced to promote its crucial contribution in new fields, like solar cells [22]–[24], nanothermometers [25]–[28], optical bioimaging and display devices [29]–[32]. Energy transfer could be divided into two main categories: radiative and non-radiative, both require an overlap between the emission of donor and the absorption of acceptor. Radiative energy transfer is dominant when the distance between donor and acceptor is long, but non-radiative arises at short range. Non-radiative energy transfer

process could be interpreted broadly to contain multiple classifications, such as resonant and non-resonant transfer, excitonic transfer, Auger transitions, and charge transport [2], but resonant and non-resonant transfer is most extensively studied. Resonant energy transfer usually happens between two ions with same energy level transition, but non-resonant energy transfer also called as phonon assisted energy transfer, which specially needs phonons to bridge the energy mismatch [2].

The most common description of energy transfer usually involves two species, and they are donor (D) and acceptor (A) in scientific terms. After excitation, the donor has absorbed a certain amount of energy, as a result, which populates excited states. Subsequently, it transfers energy by the way of non-radiative process to acceptor, which is followed by a transition of acceptor from ground to a higher energy state while the donor in an excited state relaxes to a lower state [3], [33].

The mechanisms of energy transfer have been remarkably developed during the past years, and Andrews has stated in reference [34] that the mechanism for radiative and non-radiative process is indistinguishable. Generally accepted one for non-radiative energy transfer explained by Förster is for organic molecules, hereafter Dexter reformulated this theory and applied it to inorganic materials [2]. Energy transfer requires a certain interaction between donor and acceptor, and a suitable distance is thus demanded for this interaction. Based on the type of interaction, R^{-s} was introduced in the role of electric multipolar interaction, where s = 6, 8, 10 for electric dipole-electric dipole (EDD), electric dipole-electric quadrupole (EDQ) and electric quadrupole-electric quadrupole (EQQ), respectively. The exchange interaction has been found to be related to the wavefunction overlap [35].

An energy transfer model has been described by Bettinelli in reference [36], in which the surroundings of donor and acceptor ions are regarded as random distribution of numerous D and A ions instead of an isolated ions pair. The interaction between D-D is supposed to happen in this case except that of between D-A, which is named migration process as shown in Fig. 4. One consideration is to assess how the migration process of donors would be affected by the interionic distances. Based on the above contexts, the relevant information of D-A energy transfer is summarized in Table 1.
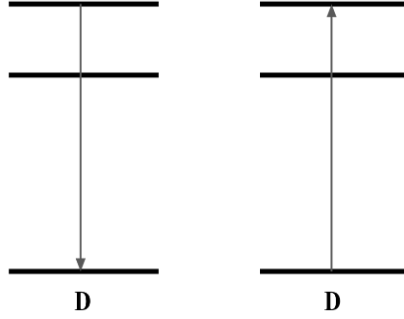
Fig. 4. The migration process between donor ions.

Table 1. The information of D-A energy transfer process

	low concentration of donors	high donor concentration	the intermediate regime
D-D migration	No	Yes	comparable with D–A transfer rates
decay profile	non-exponential	exponential	non-exponential for short times but an exponential profile for long times
the time evolution of I_{em}	$I(t) = I_0 exp\left(-\frac{t}{\tau_0} - \alpha\left(\frac{t}{\tau_0}\right)^{3/s}\right)$	$I(t) = I_0 exp\left(-\frac{t}{\tau_0} - k_{ET}t\right)$	$I(t) = I_0 exp\left(-\frac{t}{\tau_0} - \gamma\sqrt{t} - Wt\right)$

a. $\alpha = \frac{4}{3}\pi\Gamma\left(1 - \frac{3}{s}\right)N_A R_c^3$, Γ is the gamma function, and N_A is the acceptor concentration. R_c is defined as the critical distance for which the transfer rate of D-A equals that of the isolated donor.

b. k_{ET} is the total energy transfer probability.

c. $\gamma = \frac{4}{3}\pi^{3/2}N_A C_{DA}^{1/2}$ (When s = 6), W is the migration parameter.

5. Thesis Outline

The main work of this thesis is related to the research in the following aspects:

i.   Various energy transfer processes in eulytite-type materials.

In chapter 2 the energy transfer $Tb^{3+}\rightarrow Ln^{3+}$ (Ln = Nd or Sm) in concentrated $Sr_3Tb(PO_4)_3$ have been explored by the means of optical spectroscopy and excited state dynamic. Also, the energy transfer $Tb^{3+}\rightarrow Tm^{3+}$ in $Sr_3Y(PO_4)_3$ doped with various amounts of the two Ln^{3+} ions have been investigated.

6

ii.   The distinct energy transfer processes in indate materials.

In chapter 3 the energy transfer processes in $LaInO_3$ doped with Bi^{3+}, Tb^{3+} and Eu^{3+} have been studied by way of luminescence spectroscopy and decay kinetics of Bi^{3+} excited state and of the $^5D_4$ excited state of Tb^{3+}. Besides, the possibility of white light emission has been examined.

iii.   Energy transfer processes in Fluoride materials.

Chapter 4 includes the discussion about the energy transfer processes in $NaBiF_4$ doped with Tb^{3+} and Eu^{3+}. Moreover, the luminescence properties in aqueous phase have been studied.

iv.   Radiative energy transfer processes for achieving yellow emission persistent phosphor. Chapter 5 describes one desired yellow emission persistent phosphor that has been achieved by depositing $CaAl_2O_4$: Eu, Nd (CAO) persistent phosphors and $Y_3Al_5O_{12}$: Ce as a polymer layer with a certain thickness. White light emission persistent phosphor can also be attained in a proper way.

Chapter 2

(a) Energy transfer processes in $Sr_3Tb(PO_4)_3$ eulytite-type materials singly doped with Nd^{3+} and Sm^{3+}

Abstract: In this study, the optical spectroscopy, the excited state dynamics and in particular the energy transfer $Tb^{3+} \rightarrow Ln^{3+}$ (Ln = Nd or Sm), have been investigated in detail in eulytite double phosphate hosts of the type $Sr_3Tb(PO_4)_3$ doped with 1 mol% Ln^{3+}. It has been found that for Ln = Nd and Sm, the energy transfer efficiency (η_T) is 0.76 and 0.73, respectively, thanks to the assistance of fast migration in the Tb^{3+} $^5D_4$ level. The pathway responsible for the transfer of excitation has been unambiguously identified in the case of $Sr_3Tb_{0.99}Nd_{0.01}(PO_4)_3$, whilst the situation is more complex for $Sr_3Tb_{0.99}Sm_{0.01}(PO_4)_3$, due to high density of the final Sm^{3+} states that could be involved. The $Tb^{3+} \rightarrow Nd^{3+}$ energy transfer has been tentatively attributed to the exchange interaction based on the short transfer distance and multipolar selection rules.
Keywords: Energy transfer, Lanthanide ions, Luminescence, Phosphate materials

1. Introduction

In the last years, a lot of investigations have been launched into energy transfer processes involving trivalent rare earth ions in inorganic solids. And a thorough study has been performed by us regarding the mechanisms responsible for the $Tb^{3+} \rightarrow Eu^{3+}$ energy transfer [[37]–[40]] in concentrated eulytite compounds of the type $A_3Tb(PO_4)_3$ (A = Sr, Ba), belonging to a class of luminescent materials that was studied for the first time by Prof. Blasse [41]. In these materials, fast energy migration occurs among the $^5D_4$ level of Tb^{3+} ions. For these reasons, we found it is interesting to extend the previous studies to energy transfer processes involving Tb^{3+} and other lanthanide ions, such as Nd^{3+} and Sm^{3+}, present as dopants in the eulytite $A_3Tb(PO_4)_3$, with the aim of understanding the impact of the various electronic structures of the co-dopants on the transfer mechanisms and rates. The results of this new investigation are presented and discussed here.

2. Experimental and structural data

The eulytite-type compounds $Sr_3Tb(PO_4)_3$ and $Sr_3Tb_{0.99}Ln_{0.01}(PO_4)_3$ (Ln = Nd, Sm) were obtained by solid state reaction at high temperature (1250 °C, 48 h) as described in Ref. [37].

X-ray diffraction patterns were measured using a Thermo ARL X'TRA powder diffractometer, in Bragg-Brentano geometry, with a Cu-anode as X-ray source and a Peltier Si (Li) cooled solid state detector. The XRD patterns were collected with a scan rate of 1.2°/min and an integration time of 1.5 s in the 5–90° 2θ range.

Luminescence spectra and decay curves were collected at room temperature with a Fluorolog 3 (Horiba-Jobin Yvon) spectrofluorometer. Time correlated single photon counting technique (TCSPC) was used to measure the decay curves, with a xenon microsecond pulsed lamp as excitation source. For the IR measurements, a linear InGaAs detector working up to 1700 nm was used (512 pixels, 50x500 μm).

3. Results and discussion

3.1 Structural investigation

Single eulytite-type phases were obtained for all the synthesized eulytite double phosphates [$Sr_3Tb(PO_4)_3$ and $Sr_3Tb_{0.99}Ln_{0.01}(PO_4)_3$, Ln = Nd and Sm], as confirmed by powder X-ray diffraction (XRD). In Fig. 1, the patterns of the samples are presented; all the diffraction peaks belong to eulytite structure, and no impurity phases are observed in comparison with the standard XRD pattern of $Sr_3Tb(PO_4)_3$.
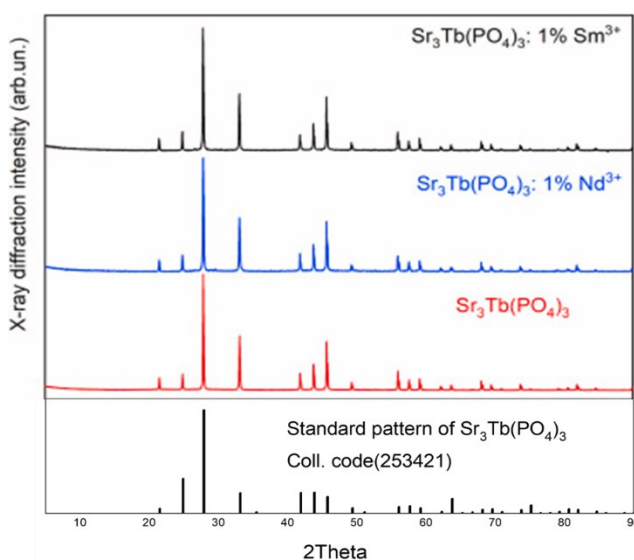
Fig. 1. X-ray diffraction powder patterns of undoped and doped $Sr_3Tb(PO_4)_3$ samples.

It is well known that eulytite double phosphates with the formula $A_3M(PO_4)_3$ (A = Ca, Sr, Ba; M = La-Lu, Y, Bi) are cubic (space group) and isomorphous with the mineral eulytine (Bi_4Si_3O12) [41], [42]. The crystal structures of the materials under investigation have been recently described [39]. The partial substitution of Tb^{3+} with 1 mol% of another lanthanide ion (in the present study Nd^{3+} or Sm^{3+}) has a negligible impact on the cell parameter of the doped phase with respect to the undoped one.

3.2 Luminescence spectroscopy

3.2.1. $Sr_3Tb(PO_4)_3$ eulytite doped with Nd^{3+}

The luminescence spectra of the $Sr_3Tb_{0.99}Nd_{0.01}(PO_4)_3$ eulytite are shown in Fig. 2(a) and (b) in the visible and NIR regions, respectively.
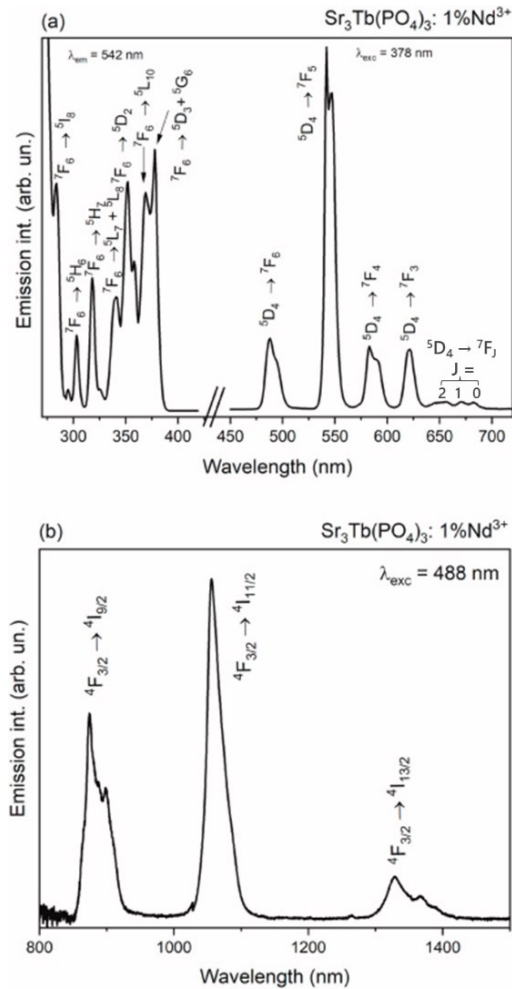
Fig. 2. (a) The RT excitation (λ_{em} = 542 nm) and visible emission (λ_{ex} = 378 nm) spectra of $Sr_3Tb_{0.99}Nd_{0.01}(PO_4)_3$. (b) NIR RT emission spectrum of $Sr_3Tb_{0.99}Nd_{0.01}(PO_4)_3$ with excitation at 488 nm.

The excitation spectrum of the emission observed at 542 nm is shown in Fig. 2(a). Irradiation in the near UV is bound to excite in practice only Tb^{3+}, since its concentration is 99 times higher than the one of Nd^{3+}. The visible emission spectrum obtained upon excitation in the levels above $^5D_3$ (close to 350 nm) is dominated by emission from the $^5D_4$ level of Tb^{3+} to lower lying ^7F_J ($J = 0$-5) (Figure 2a); no emission from $^5D_3$ is observed due to efficient cross relaxation leading to fully non-radiative $^5D_3 \rightarrow {}^5D_4$ decay. Conversely, excitation at the same wavelength gives rise to emission bands in the NIR region that are clearly assigned to transitions originating from the $^4F_{3/2}$ level of Nd^{3+} to lower lying ^4I_J ($J = 9/2, 11/2, 13/2$) (Figure. 2(b). This indicates that $Tb^{3+} \rightarrow Nd^{3+}$ energy transfer is present. The $^4F_{3/2}$ emission level is populated by multiphonon relaxation from $^4G_{5/2}$ (see below) across the levels located in between, since the eulytite phosphate host has high energy phonons available (up to 900 cm^{-1}) [43].

This observation agrees with the conclusions drawn by Nakazawa and Shionoya in their study about energy transfer between rare earth ions in Ca(PO$_3$)$_2$ glass [44], who attributed this process to the resonant mechanism:

$$(1) \qquad {}^5D_4\,(Tb^{3+}) + {}^4I_{9/2}\,(Nd^{3+}) \rightarrow {}^7F_4\,(Tb^{3+}) + {}^4G_{5/2}\,(Nd^{3+})$$
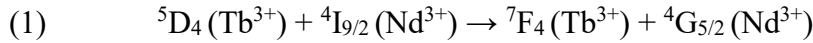
In Fig. 3, the mechanism responsible for the population of Nd^{3+} $^4F_{3/2}$ emission level by energy transfer from $^5D_4$ level of Tb^{3+} is depicted.
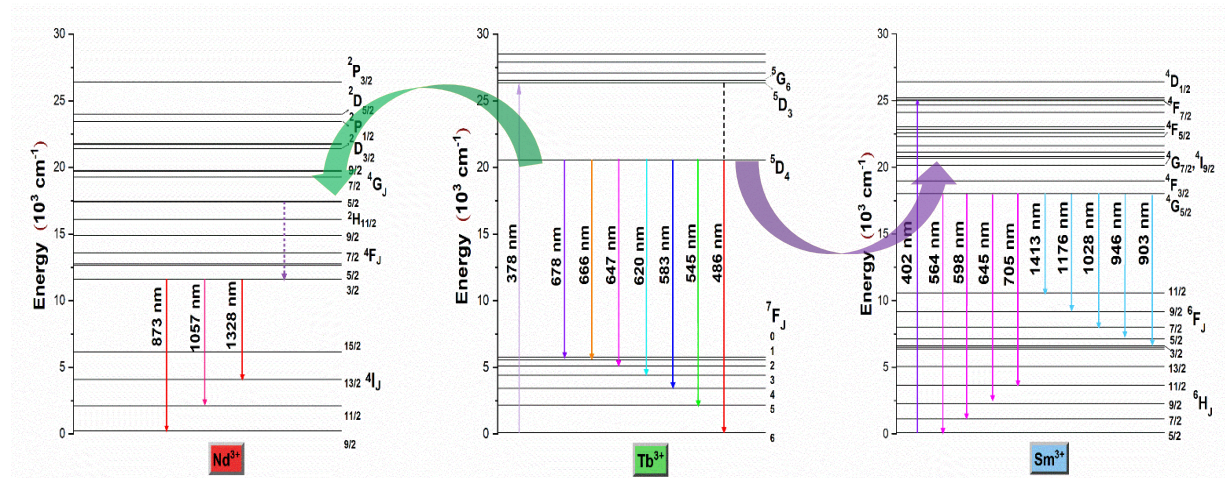
Fig. 3. The energy levels arise from $4f^n$ configurations of Nd^{3+}, Tb^{3+} and Sm^{3+}. The population mechanism of the Nd^{3+} $^4F_{3/2}$ and Sm^{3+} $^4G_{5/2}$ emission levels by energy transfer from the $^5D_4$ level of Tb^{3+} is also reported.

The decay curve of the $^5D_4$ level of Tb^{3+}, measured upon pulsed excitation at 378 nm, is shown in Fig. 4.
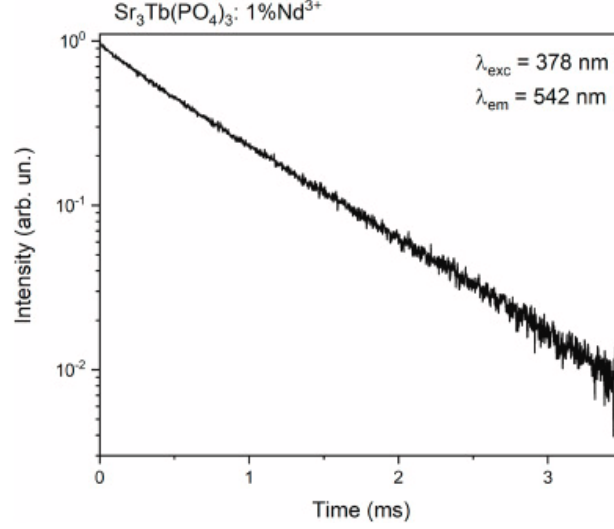
Fig. 4. Room temperature $^5D_4$ decay curve of Tb^{3+} (λ_{exc} = 378 nm) in $Sr_3Tb_{0.99}Nd_{0.01}(PO_4)_3$.

The profile is exponential with a decay constant τ_{Tb-Nd} = 0.64 ms, compared with the value τ_{Tb} = 2.68 ms obtained for neat $Sr_3Tb(PO_4)_3$ [37]. This indicates that the $Tb^{3+} \rightarrow Nd^{3+}$ occurs following fast energy migration in the Tb^{3+} subset of ions ($^5D_4$ level) [39], [45].

The effective energy transfer probability k_{ET} can be estimated from the expression [46]:

$$(2) \qquad 1/\tau_{Tb-Nd} = 1/\tau_{Tb} + k_{ET}$$

where τ_{Tb} and τ_{Tb-Nd} are the $^5D_4$ decay times in the absence and in the presence of the Nd^{3+} dopant. The resulting value is k_{ET} (Tb→Nd) = 1.19×10^3 s^{-1}. Additionally, the energy transfer efficiency η_T can be estimated using [47]:

$$(3) \qquad \eta_T = 1 - \tau_{Tb-Nd}/\tau_{Tb}$$

and the value η_T (Nd) = 0.76 is found. The transfer efficiency is relatively high; slightly larger values were found for $Sr_3Tb(PO_4)_3$ and $Ba_3Tb(PO_4)_3$: Eu^{3+} in which the doping level was ten times higher [40]. The material could convert UV-visible excitation to NIR emission from $^4F_{3/2}$, but it must be noted that significant non-radiative losses are predicted to occur through the almost resonant back-transfer process:

$$(4) \qquad {}^7F_6\,(Tb^{3+}) + {}^4F_{3/2}\,(Nd^{3+}) \rightarrow {}^7F_1\,(Tb^{3+}) + {}^4I_{15/2}\,(Nd^{3+}).$$
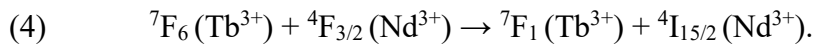
The study of this transfer lies beyond the scope of this paper, as our present experimental facilities do not allow us to measure the decay of $^4I_{15/2}$ (Nd^{3+}) upon pulsed excitation.

3.2.2. Sr₃Tb(PO₄)₃ eulytite doped with Sm³⁺

As shown in Figure 5a, the room temperature visible emission spectrum of $Sr_3Tb_{0.99}Sm_{0.01}(PO_4)_3$ measured upon excitation at 402 nm ($^4F_{7/2}$ level of Sm^{3+}) shows four well defined emission bands assigned to transitions from the $^4G_{5/2}$ level of Sm^{3+}, which is populated by multiphonon relaxation, and terminating onto the final levels ^6H_J, with $J = 5/2$ (peaking at 564 nm), 7/2 (598 nm), 9/2 (645 nm) and 11/2 (705 nm) [48].
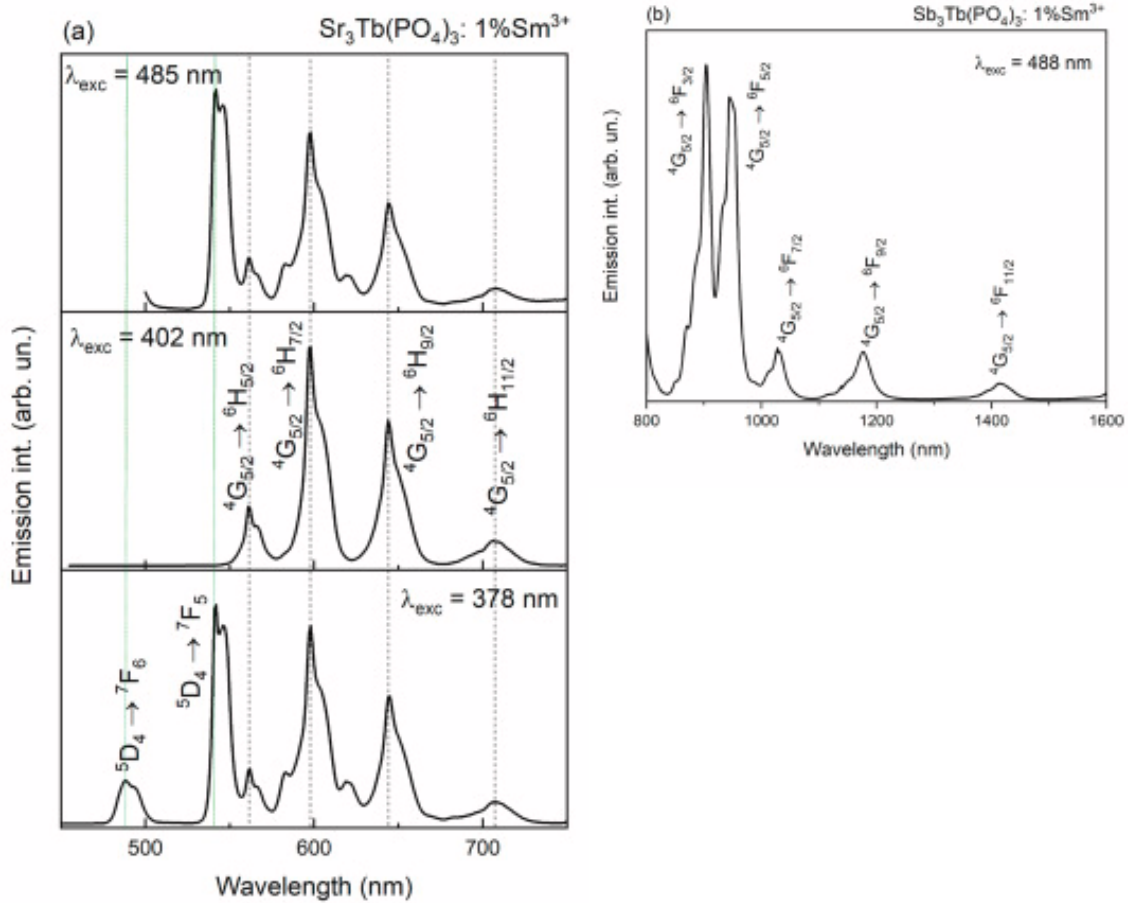
Fig. 5. (a) Visible RT emission spectrum of $Sr_3Tb_{0.99}Sm_{0.01}(PO_4)_3$ with excitation at 378, 402 and 485 nm. (b) NIR RT emission spectrum of $Sr_3Tb_{0.99}Sm_{0.01}(PO_4)_3$ with excitation at 488 nm.

On the other hand, the emission spectrum excited at 378 nm shows two additional main bands, peaking at 488 and 542 nm and assigned to the $^5D_4 \rightarrow {}^7F_6$ and $^5D_4 \rightarrow {}^7F_5$ transitions of Tb^{3+}, respectively. The emission spectrum obtained upon excitation at 485 nm shows the same bands as for $\lambda_{exc} = 378$ nm, apart from the $^5D_4 \rightarrow {}^7F_6$ which is resonant with the excitation. Sm^{3+} does not appear to be excited at this latter wavelength, although absorption in this region has been

reported [49]. As noted above in the case of Nd^{3+}-doped sample, Tb^{3+} concentration is 99 times higher than the one of Sm^{3+}, and therefore its excitation can be considered as negligible. Figure. 5b shows the NIR emission spectrum measured at RT upon excitation at 488 nm. The bands peaking at 903, 946, 1028, 1176 and 1413 nm are assigned to transitions from the $^4G_{5/2}$ level of Sm^{3+} to the levels ^6H_J (J = 5/2 – 11/2) respectively [50].

Figure. 6 shows the excitation spectrum of the sample under investigation measured with λ_{em} = 542, 598 and 645 nm.
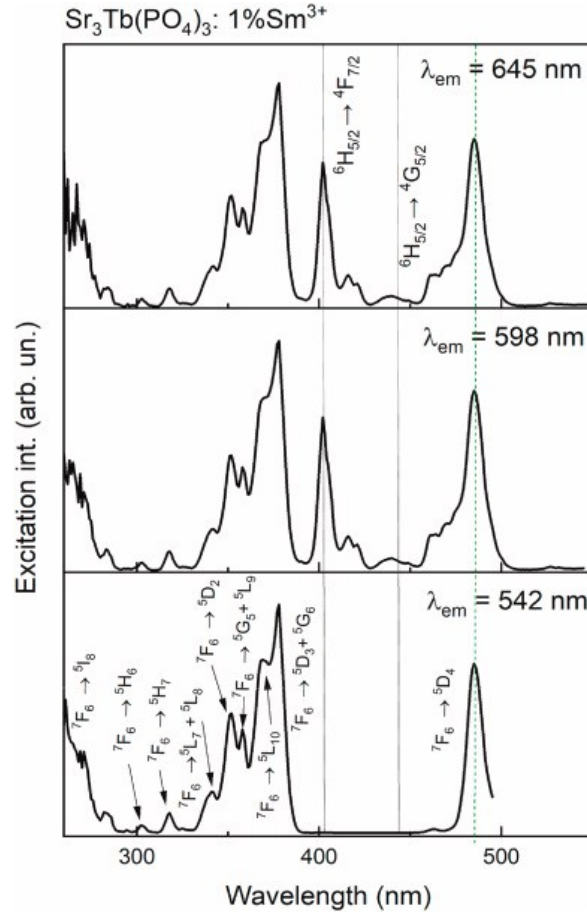
Fig. 6. RT excitation spectrum of $Sr_3Tb_{0.99}Sm_{0.01}(PO_4)_3$ measured with λ_{em} = 542, 598 and 645 nm.

The emission at 542 nm does not correspond to any excitation transition related to Sm^{3+}, and the relevant excitation spectrum presents the typical features of Tb^{3+} in eulytites [37], with dominant peaks at 378 and 488 nm, corresponding to transitions to the $^5D_3$ and $^5D_4$ levels. On the other hand, the excitation spectra measured with λ_{em} = 598 and 645 nm shows both Sm^{3+}-related features, such as the peak at 402 nm ($^6H_{5/2} \rightarrow {}^4F_{7/2}$) and the structure located in the region 420 –

475 nm, and Tb^{3+}-related peaks, such as the ones in the UV region, and especially at 378 and 488 nm. It is therefore clear that $Tb^{3+} \rightarrow Sm^{3+}$ energy transfer takes place, as documented for other oxide materials (see for example [49], [51]).

The mechanism responsible for the energy transfer process is assigned as

$$(5) \qquad {}^5D_4\,(Tb^{3+}) + {}^6H_{5/2}\,(Sm^{3+}) \rightarrow {}^7F_6\,(Tb^{3+}) + {}^4I_{9/2}, {}^4G_{7/2}\,(Sm^{3+}),$$
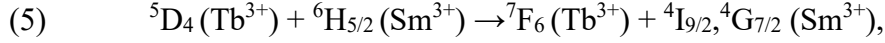
based on the energy level diagrams of the two ions [52], and the spectral overlap between the excitation of Sm^{3+} and the emission of Tb^{3+} in the region between 480 and 500 nm [49]. The ${}^4I_{9/2}$, ${}^4G_{7/2}$ rapidly relax to the ${}^4G_{5/2}$ emission level through multiphonon relaxation (see Figure. 3).

The room temperature decay curves of the luminescence in the visible region, after pulsed excitation of $Sr_3Tb_{0.99}Sm_{0.01}(PO_4)_3$, are shown in Figure. 7.
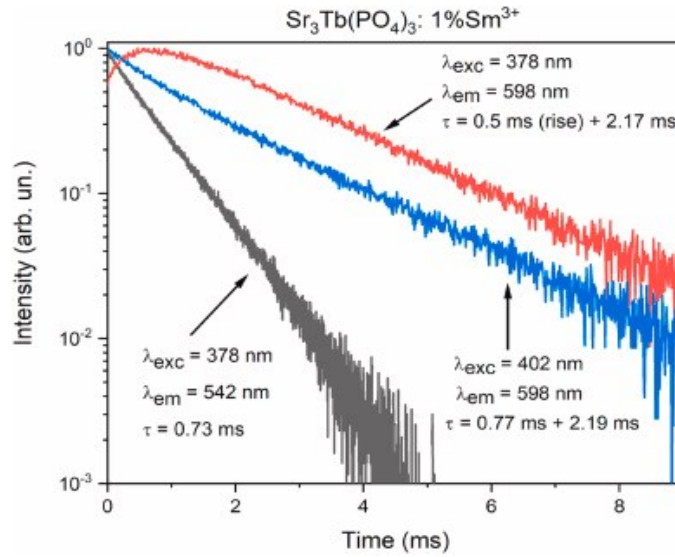
Fig. 7. RT decay curves of the luminescence in the visible region, after pulsed excitation of $Sr_3Tb_{0.99}Sm_{0.01}(PO_4)_3$.

The decay profile of the ${}^5D_4$ level of Tb^{3+} is almost perfectly exponential with a decay constant of 0.73 ms. The decay is significantly faster than for neat $Sr_3Tb(PO_4)_3$ (2.68 ms) due to energy transfer to Sm^{3+}. As expected, the exponential profile clearly indicates that the transfer process occurs in the presence of fast migration among the ${}^5D_4$ levels of Tb^{3+}. Using equations (2), (3) the values $k_{ET}\,(Tb \rightarrow Sm) = 9.97 \times 10^2$ s^{-1} and $\eta_T\,(Sm) = 0.73$ are obtained, quite similar to the ones obtained for the transfer involving the Nd^{3+} dopant.

As for the RT decay curves of the ${}^4G_{5/2}$ level of Sm^{3+}, the one obtained upon direct excitation at 402 nm, corresponding to the ${}^4F_{7/2}$ level, and observation at 598 nm (transition ${}^4G_{5/2} \rightarrow {}^6H_{7/2}$)

is almost exponential with a decay constant for $^4G_{5/2}$ of 2.19 ms, with a minor faster component at short times of about $0.7 - 0.8$ ms, attributed to a small degree of overlapping with the $^5D_4 \rightarrow {}^7F_4$ transition of Tb^{3+}. For the sake of comparison, the decay of $^4G_{5/2}$ in diluted $Sr_3Y(PO_4)_3$: 1 mol% Sm^{3+} was measured by us to be exponential with a decay time of 2.74 ms, whilst in the similar host $Ba_3Lu(PO_4)_3$: 1 mol% Sm^{3+} it was estimated to be 2.32 ms [45]. The temporal profiles of the $^4G_{5/2}$ emission upon excitation at 378 ($^5D_3$) and 488 nm ($^5D_4$) are perfectly superimposable, and show a well evident rise, followed by an exponential decay with a time constant of 2.17 ms. The exponential build-up of the emission at short times after the pulsed excitation has a time constant of about 0.50 ms and is attributed to the feeding of $^5D_4$ due to the energy transfer process; this confirms the conclusions drawn above about the transfer process. It is worth noting that the emission from the $^4G_{5/2}$ level of Sm^{3+} cannot be quenched from any efficient back energy transfer to Tb^{3+}, due to energy mismatch of the states involved.

A comparison between the resulting colors in the two materials is shown in the CIE diagrams (Fig. 8).
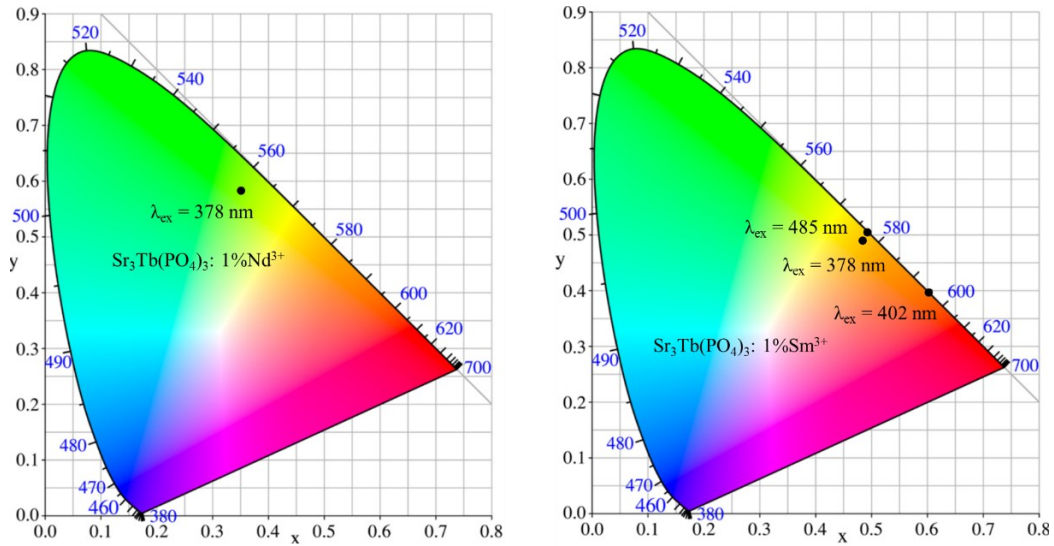
Fig. 8. CIE diagrams for (a) $Sr_3Tb_{0.99}Nd_{0.01}(PO_4)_3$ and (b) $Sr_3Tb_{0.99}Sm_{0.01}(PO_4)_3$ samples.

Since Nd^{3+} presents emission only in the NIR region upon excitation into the $^5D_3$ level of Tb^{3+}, only the green feature of Tb^{3+} is obtained for Nd^{3+}-doped material. Conversely, upon the same excitation, both Tb^{3+} and Sm^{3+} emissions are presented in the visible region, with a domination of the latter. Therefore, the obtained color is presented in the orange region. Similar CIE are

obtained when the same sample is excited at 485 nm as in this case, clearly the emission band at 485 nm, that is resonant with the excitation, does not contribute to the final emission spectrum, leading to a slight shift in the CIE coordinates but always in the orange region. Finally, at 402 nm, Sm^{3+} ion is selectively excited and the final spectrum in the visible region results in a red color due to sole emission of this ion.

3.2.3. Impact of the crystal structure on the energy transfer mechanism

Details about the crystal structure of the materials under investigation have been reported before [39], [40], [42]. There is only one site for both divalent and trivalent cations with coordination number 9 and point symmetry C_3. The A^{2+}/M^{3+} cations are presented in a disordered way in a single crystallographic site, with a relative occupation of 0.75/0.25. As reported above, the lattice parameters are in practice constant after dilute substitution of Tb^{3+} with Nd^{3+} or Sm^{3+} (doping) due to the close similarity of their ionic radii (1.095 Å for Tb^{3+}, 1.163 Å for Nd^{3+} and 1.132 Å for Sm^{3+} in 9-fold coordination) [53].

As for the local environment of the cations, each A^{2+}/M^{3+} ion is surrounded by other identical 11 nearest neighbor A^{2+}/M^{3+} cationic sites. Therefore, due to the abovementioned occupation factors, one trivalent ion on average is surrounded by $11 \times 0.25 = 2.75$ trivalent near neighbor ions. This implies that in the neat terbium eulytite each Tb^{3+} ion has 2.75 Tb^{3+} nearest neighbors, and in the Tb/Ln materials 2.722 Tb^{3+} and 0.028 Ln^{3+} ions nearest neighbor ions (Ln = Nd, Sm). In the presence of the Ln^{3+} dopant the crystallographic positions of the atoms are unchanged and so the distances $Tb^{3+} - Tb^{3+}$ and $Tb^{3+} - Ln^{3+}$ are considered identical. In a previous paper [40] we have reported that in the same host the distances between a reference cation and the nearest neighbor ones have three possible values, i.e. 3.971(2) Å (x3), 4.378(1) Å (x2) and 4.754(1) Å (x6). We can safely adopt these values for the nearest neighbor $Tb^{3+} - Nd^{3+}$ and $Tb^{3+} - Sm^{3+}$ distances in the materials under investigation. As migration among the $^5D_4$ levels of Tb^{3+} is very fast, the excitation will reach a donor ion which has at least one Nd^{3+} or Sm^{3+} ion in a nearest neighbor position. This implies that the energy transfer process presumably occurs across a short distance (3.971 – 4.754 Å), and that short-range interactions, such as electric quadrupole-electric quadrupole (EQ-EQ) and/or exchange, could play a dominant role.

In fact, in the case of the $Tb^{3+} \rightarrow Eu^{3+}$ energy transfer in Sr, Sr/Ba and Ba-eulytites, Carneiro Neto et al. have recently shown, through the comparison of detailed theoretical calculations and experimental data derived from luminescence spectroscopy, that these hypotheses are indeed

correct [40]. Presumably, a similar situation occurs for the materials under investigation. At this stage, a few comments can be made. In the case of the $Tb^{3+} \rightarrow Sm^{3+}$ transfer, the final states for Sm^{3+} lie in an energy region that very dense with levels, and at least two states $[^4I_{9/2}, ^4G_{7/2}$ $(Sm^{3+})]$ are involved; this makes a simple analysis unfeasible in the absence of detailed theoretical calculations. On the other hand, the $Tb^{3+} \rightarrow Nd^{3+}$ is much simpler and more amenable to some considerations.

The transfer mechanism (1) in the past has been assigned, in a $Ca(PO_3)_2$ glass doped with low amounts of Tb^{3+} (3%) and Nd^{3+} (0.1 – 3%), to the electric dipole-electric quadrupole interaction [44], [54]. In the present case, given the short transfer distance and the previous theoretical results on the $Tb^{3+} \rightarrow Eu^{3+}$ case, this mechanism presumably is not the dominant one. On the other hand, the low values of the squared reduced matrix elements of the unit tensor operator $<\|U(\lambda)\|>2$ (for $\lambda = 2, 4, 6$) for the $^5D_4 \rightarrow ^7F_4$ of Tb^{3+} [52] do not appear to be compatible with an EQ-EQ interaction, since this requires high values of $<\|U(2)\|>2$ for the transitions involved in the two optical centers [55]. For this reason, we tentatively attribute the transfer to exchange interaction, being aware that detailed theoretical calculations are required to obtain a full understanding of the transfer mechanism.

4. Conclusions

The energy transfer mechanisms have been identified for dopant ions in $Sr_3Tb_{0.99}Nd_{0.01}(PO_4)_3$ and $Sr_3Tb_{0.99}Sm_{0.01}(PO_4)_3$, in the simpler case of the Nd^{3+} acceptor, there are indications that the short-range transfer process, occurring for distances close to 4 Å, is mainly due to the exchange interaction requiring wavefunction overlap. This agrees with the rule of thumb proposed by Blasse and Grabmaier for Ln^{3+} ions, allowing exchange for donor-acceptor distances lower than 5 Å [45]. As a last remark, we note that in the materials under investigation, downshifting from the near UV and the visible regions to the near IR [56] could be obtained. The efficiency of this process remains to be ascertained in the case of the eulytite activated with Nd^{3+}.

(b) Energy Transfer Processes in Sr$_3$Y(PO$_4$)$_3$ Eulytite Singly Doped and Co-Doped with Tb^{3+} and Tm^{3+}

(This finding has been published as "*Energy transfer between Tb^{3+} and Tm^{3+} in eulytite materials of the type Sr$_3$Ln(PO$_4$)$_3$ [Ln=trivalent lanthanide ion(s)], Special issue of «Optics and Spectroscopy» dedicated to the anniversary of professor Marina Popova*")

Abstract: In this work the optical spectroscopy and the energy transfer processes involving the Tb^{3+} and Tm^{3+} ions, have been studied in eulytite double phosphate hosts of the type Sr$_3$Y(PO$_4$)$_3$ doped with various amounts of the two lanthanide ions. It has been found that several energy transfer and cross-relaxation processes are active in this class of materials, upon excitation in the ^{5}D$_4$ level of Tb^{3+}, and in the ^{1}G$_4$ one of Tm^{3+}. Particularly, a Tb$^{3+} \rightarrow$ Tm^{3+} transfer of excitation has been found to quench strongly the ^{5}D$_4$ level of Tb^{3+}. This process occurs with a transfer efficiency increasing from 0.08 to 0.62, for a donor concentration of 2 mol%, and an acceptor concentration increasing from 2 to 15 mol%. The emission spectra are strongly affected by the presence of Tb$^{3+} \rightarrow$ Tm^{3+} energy transfer, and Tm$^{3+} \rightarrow$ Tm^{3+} cross relaxation processes.
Keywords: Energy transfer, Lanthanide ions, Luminescence, Phosphate materials, Optical spectroscopy

1. Introduction

The energy transfer Tb$^{3+} \rightarrow$ Tm^{3+} has been documented and investigated in the past, but special emphasis was given to the use of these ions in crystalline or non-crystalline materials in order to produce white light (when co-doped with other suitable ion(s)) [57]–[59], or enhanced emission in the near IR region [60]. Apart from these studies pointing at interesting applications of these phenomena, not many investigations have dealt in a detailed way with the basic mechanisms dealing with the transfer mechanisms involving Tb^{3+} and Tm^{3+} [[59], [60], [61], [62]–[69], [70]–[72]].

In recent times, our group has studied energy transfer processes involving Tb and another lanthanide ion in eulytite-type cubic materials with formula A$_3$M(PO$_4$)$_3$ (A = divalent cation, M = trivalent cation) [37], [38], [40], [74] . We found it is interesting to extend these investigations to (Tb, Tm) co-doped eulytites to contribute to the understanding of the Tb$^{3+} \rightarrow$ Tm^{3+} transfer processes, and evidence the impact of the crystal structure on the transfer efficiency and

mechanism. In this contribution we shall focus on the energy transfer from the donor $^5D_4$ level of Tb^{3+} to the acceptor Tm^{3+} ion.

2. Experimental

A series of singly doped and co-doped eulytites $Sr_3Y_{1-x-y}Tb_xTm_y (PO_4)_3$, ($x = 0, 0.01, 0.02$; $y = 0, 0.01, 0.02, 0.03, 0.05, 0.07, 0.10, 0.15$) was synthesized in polycrystalline form by solid state reaction at high temperature (1250 ℃, 48 h) as previously described [73]. X-ray diffraction patterns, luminescence spectra and decay curves were measured as described in ref. [77].

3. Results and discussion

All samples under investigation were found by powder X-ray diffraction (PXRD) to be single phase with a cubic eulytite phases (space group *I-43d*) [42]. No impurity phases were observed.

The energy level diagram of the Tb^{3+} and Tm^{3+} ions is shown in Fig. 1. The emission and excitation spectra of the singly doped eulytites are presented in Fig. 2 and 3.
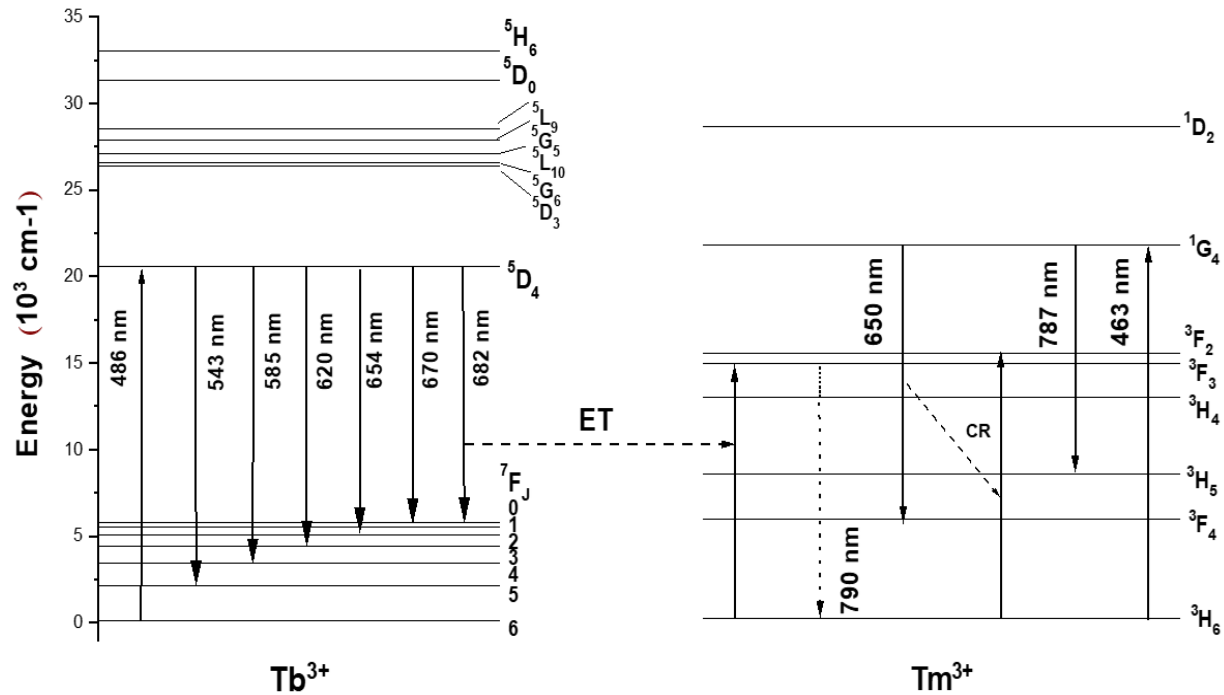
Figure 1. Scheme of energy levels, energy transfer and cross-relaxation pathways for Tb^{3+} and Tm^{3+} ions discussed in the text.
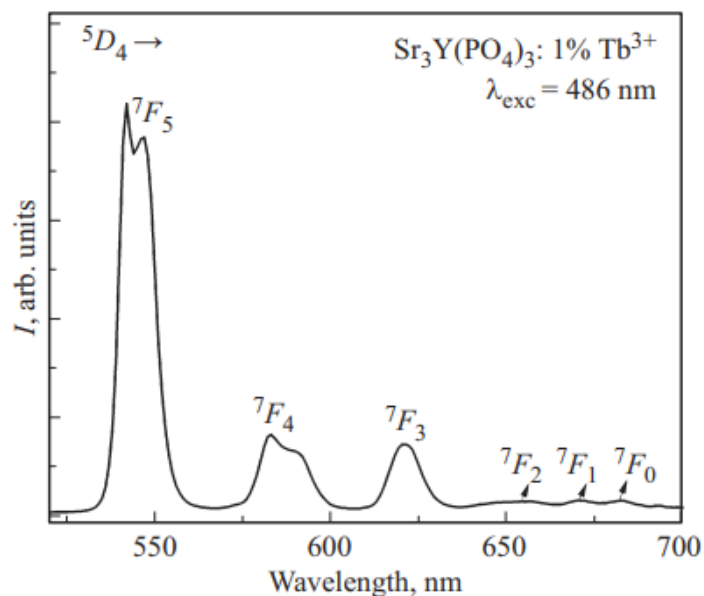
Figure 2. Luminescence spectra of $Sr_3Y_{0.99}Tb_{0.01}(PO_4)_3$ at room temperature at excitation at a wavelength of 486 nm.
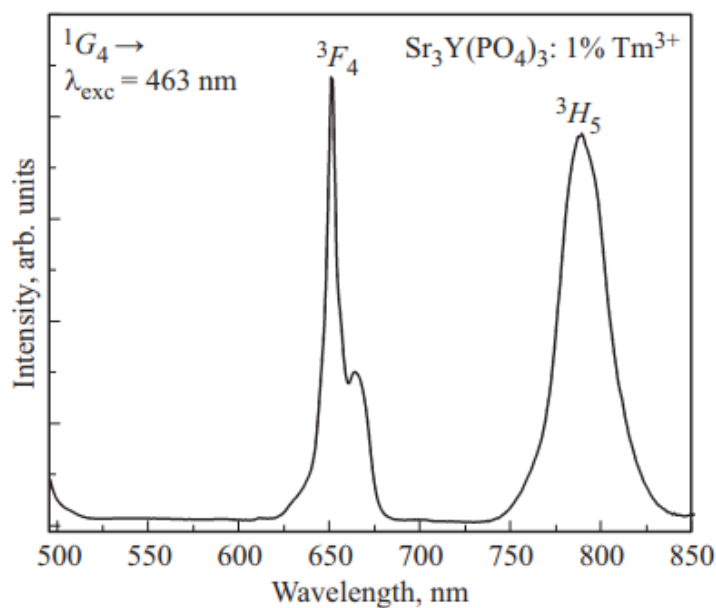
Figure 3. Luminescence spectra of $Sr_3Y_{0.99}Tm_{0.01}(PO_4)_3$ at room temperature at excitation at wavelength of 463 nm.

Following excitation at 486 nm (20580 cm^{-1}) in the $^5D_4$ level, the sample $Sr_3Y_{0.99}Tb_{0.01}(PO_4)_3$ shows the usual emission transitions $^5D_4 \rightarrow ^7F_J$ (J = 0−5) in the region 520−700 nm (Fig. 2), whilst upon 463 nm excitation (21598 cm^{-1}, in the $^1G_4$ level) $Sr_3Y_{0.99}Tm_{0.01}(PO_4)_3$ gives rise to two

bands assigned to the transitions $^1G_4 \to {}^3F_4$, and $^1G_4 \to {}^3H_5$, located at 650 and 787 nm (15380 and 12710 cm^{-1}) respectively (Fig. 3). The latter assignment [75] is proposed assuming that cross-relaxation has a minor impact and multiphonon relaxation from $^1G_4$ is negligible, due to the low concentration of Tm, and to the fact that the Raman spectrum of the phosphate eulytites has typically a high energy peak in the range from 950 to 990 cm^{-1} [76], implying that more than six vibrational quanta are required to bridge the $^1G_4$–$^3F_2$ energy gap of Tm^{3+}, amounting to almost 6200 cm^{-1} [52]. The decay curve of the $^5D_4$ level of Tb^{3+} in Sr$_3$Y$_{0.99}$Tb$_{0.01}$(PO$_4$)$_3$ was measured at RT upon excitation at 486 nm and emission at 543 nm. It is perfectly exponential with an observed decay time of 2.79 ms (Fig. 4). Conversely, the RT decay profile of $^1G_4$ of Tm^{3+} in Sr$_3$Y$_{0.99}$Tm$_{0.01}$(PO$_4$)$_3$, measured upon excitation at 464 nm and with emission at 650 nm (Fig. 5) is distinctly non-exponential, presumably due to several almost resonant cross-relaxation mechanisms such as:

$$^1G_4\,(\text{Tm}) + {}^3H_6\,(\text{Tm}) \to {}^3F_2\,(\text{Tm}) + {}^3F_4\,(\text{Tm}) \qquad (1)$$
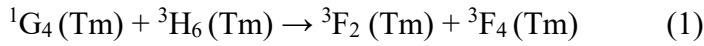
already operative at low Tm concentrations [76], [77]. The first e-folding time of this decay is 0.33 ms. For the sake of comparison, the radiative lifetime of $^1G_4$ in cubic Y$_2$O$_3$ is 0.408 ms [47].
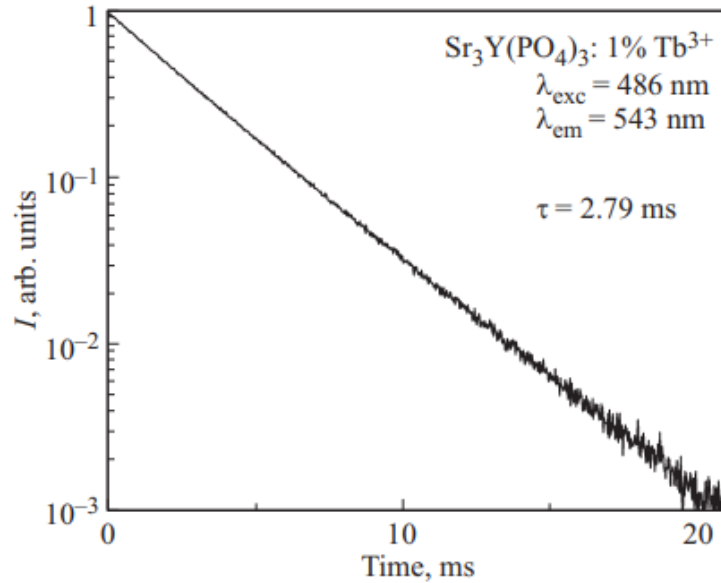
Figure 4. Luminescence decay curve of Sr$_3$Y$_{0.99}$Tb$_{0.01}$(PO$_4$)$_3$ at room temperature. Exciting light wavelength is 486 nm, registered luminescence — 543 nm.
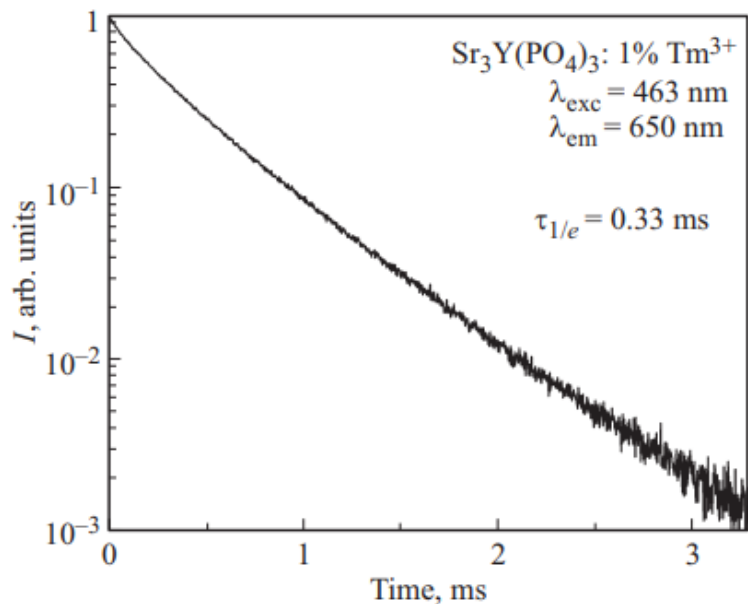
Figure 5. Luminescence decay curve of $Sr_3Y_{0.99}Tm_{0.01}(PO_4)_3$ at room temperature. Exciting light wavelength is 463 nm, registered luminescence — 650 nm.

The RT emission spectrum in the region 515−850 nm of a representative Tb/Tm co-doped sample is shown in Fig. 6 upon excitation at 486 nm into $^5D_4$ (Tb).
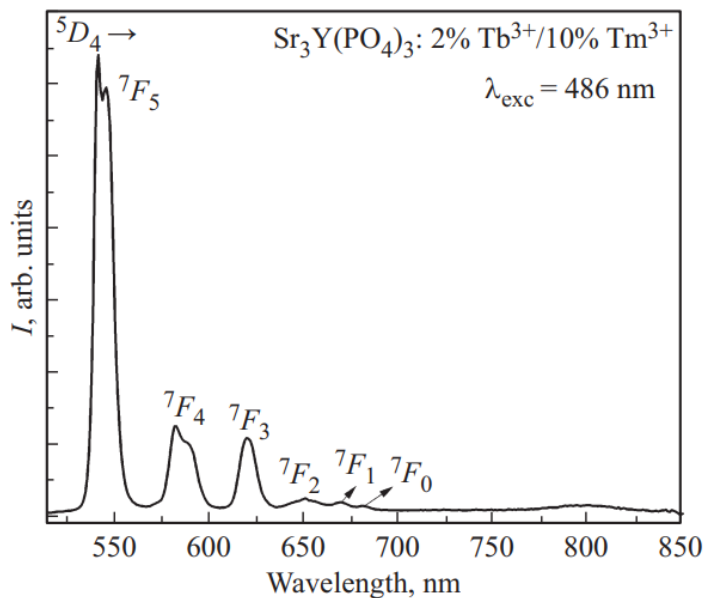
Figure 6. Luminescence spectra of $Sr_3Y_{0.88}Tb_{0.02}Tm_{0.10}(PO_4)_3$ at room temperature during excitation at wavelength of 486 nm.

The spectrum is composed of emission bands assigned to the $^5D_4 \rightarrow {}^7F_J$ transitions of Tb^{3+} discussed above, without clear evidence of bands ascribable to Tm^{3+}. On the other hand, the $Tb^{3+} \rightarrow Tm^{3+}$ energy transfer was previously found to occur based on the resonant mechanism [62]:

$$^5D_4 \,(Tb) + {}^3H_6 \,(Tm) \rightarrow {}^7F_0 \,(Tb) + {}^3F_3 \,(Tm) \qquad (2)$$

This mechanism populates the $^3F_3$ level of Tm^{3+}, which then relaxes rapidly in a non-radiative way to the $^3H_4$ level, which in principle should give rise to emission around 790 nm, due to the $^3H_4 \rightarrow {}^3H_6$ transition. This transition is not clearly visible in the present emission spectra, presumably because an additional energy transfer ($Tm^{3+} \rightarrow Tb^{3+}$) process takes place, which depopulates the $^3H_4$ level [63]:

$$^7F_6 \,(Tb) + {}^3H_4 \,(Tm) \rightarrow {}^7F_0 \,(Tb) + {}^3F_4 \,(Tm) \qquad (3)$$
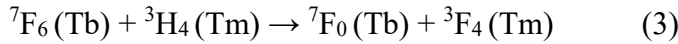
The eventual detection of emission from $^3F_4$ (around 1.75 µm) is prevented by spectral limitations of our equipment.

The decay curves of the $^5D_4$ emission of Tb^{3+}, obtained upon excitation at 486 nm, are shown in Fig. 7, for all samples containing 2 mol% of Tb, and 0, 2, 3, 5, 7 10 and 15 mol% of Tm.
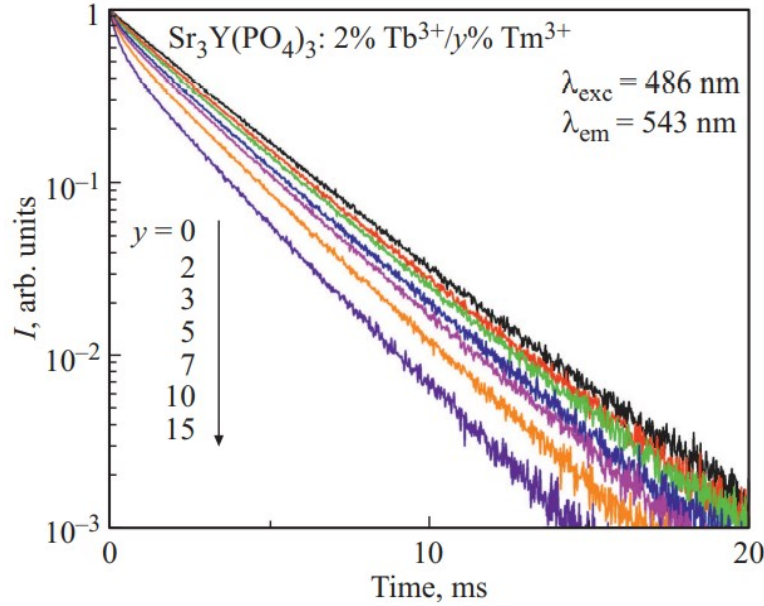
Figure 7. Radiation decay curves from the level $^5D_4$ of the Tb^{3+} ion, obtained upon excitation at wavelength of 486 nm, for all samples containing 2 mol% Tb^{3+} and 0, 2, 3, 5, 7, 10 and 15 mol.% Tm^{3+}.

Clearly, co-doping with Tm^{3+} quenches the Tb^{3+}, and therefore the mechanism (2) described above is operative. The e-folding times of the $^5D_4$ decays are reported in Table 1. Initial luminescence decay time ($\tau_{1/e}$) from the level $^5D_4$ and efficiency η_T of energy transfer $Tb^{3+} \rightarrow Tm^{3+}$ described by equation (3), in samples $Sr_3Y_{0.98-y}Tb_{0.02}Tm_y$ $(PO_4)_3$.

Table 1. The e-folding times of the $^5D_4$ decays

y	$\tau_{1/e}(^5D_4)$/ms	η_T
0	2.78	-
0.02	2.55	0.08
0.03	2.39	0.14
0.05	2.11	0.24
0.07	1.88	0.32
0.10	1.53	0.45
0.15	1.05	0.62

The energy transfer efficiencies η_T can be approximately estimated using [34]:

$$\eta_T = 1 - \tau_{Tb-Tm}/\tau_{Tb} \qquad (4)$$

where τ_{Tb-Tm} is the e-folding time of the $^5D_4$ decay in the presence of Tm^{3+}. Values for various samples are also reported in Table 1.

Inspection of the Table 1. shows that in the presence of a relatively low Tb^{3+} donor concentration the energy transfer efficiency seems to increase significantly with the increasing concentration of the Tm^{3+} acceptor. This is indicative of the fact that the assistance of energy migration is not necessary to realize relatively fast $Tb^{3+} \rightarrow Tm^{3+}$ energy transfer, in agreement with previous studies [62].

4. Conclusions

Energy transfer processes involving the Tb^{3+} and Tm^{3+} ions have been studied at room temperature in eulytite double phosphate materials with stoichiometry $Sr_3Y_{1-x-y}Tb_xTm_y$ $(PO_4)_3$, ($x = 0, 0.01, 0.02$; $y = 0, 0.01, 0.02, 0.03, 0.05, 0.07, 0.10, 0.15$). The spectroscopic results and the excited state dynamics have shown that, in the present experimental conditions, the $Tb^{3+} \rightarrow Tm^{3+}$ energy transfer and internal $Tm^{3+} \rightarrow Tm^{3+}$ cross relaxation processes take place upon

excitation in the emissive $^5D_4$ (Tb^{3+}) level belonging to the $4f^8$ configuration. The quenching of the $^5D_4$ (Tb^{3+}) emission by the Tm^{3+} acceptor appears to be rather efficient for a donor (Tb^{3+}) concentration of 2 mol%, additional channels of excitation transfer occurring upon excitation in other energy levels, such as $^1G_4$ of the Tm^{3+} ion. It is anyway already possible to conclude that the Tb/Tm system is characterized by a multitude of relaxation pathways, possibly more complex than for other pairs of lanthanide ions.

Chapter 3

White light emission and energy transfer processes in LaInO$_3$ doped with Bi^{3+}, Tb^{3+} and Eu^{3+}

Abstract：A series of LaInO$_3$ bulk materials doped with Bi^{3+}, Tb^{3+} and Eu^{3+} ions have been synthesized via a flux solid-state reaction technique, characterized by powder X-ray diffraction (PXRD) and investigated by luminescence spectroscopy. The compounds exhibit the pure crystal phase of LaInO$_3$ (JCPDS No. 08-0148), and the structure is not affected by the presence of the dopants. The Bi^{3+}→Tb^{3+} and Tb^{3+}→Eu^{3+} energy transfer phenomena have been studied by means of luminescence spectroscopy and decay kinetics of Bi^{3+} excited state and of the $^5D_4$ excited state of Tb^{3+}. White light emission is attained via altering the concentration of dopant, and the obtained color coordinate (0.3248, 0.3030) is close to standard white light (0.313, 0.329). The energy transfer process is crucial for the purpose of tuning the color of the emitted light.

Keywords: white light, energy transfer, rare earth ion, luminescence
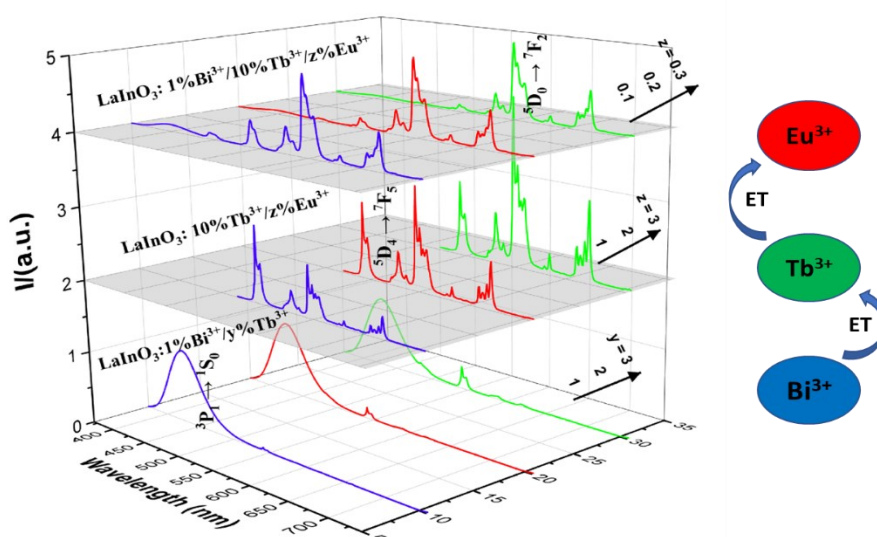
Graphical Abstract

1. Introduction

The energy transfer processes involving $Tb^{3+} \rightarrow Ln^{3+}$ (Ln = Eu, Tm, Nd and Sm) have been reported by our group in several published papers [38], [74], [78], [79], [84]. The research results suggest that not only the luminescence efficiency but also the emitted color is affected by energy transfer processes. Hence, it is meaningful to conduct in-depth exploration of energy transfer processes involving rare earth ions in inorganic hosts.

$LaInO_3$ as one member of the indates families with the perovskite structure, and often serves as model in the research about the physical properties of inorganic solids, due to its relatively simple crystal structure; the study of luminescence properties is quite important in this context. In recent years, the group led by Jun Lin has reported the photoluminescence and cathodoluminescence properties of $LaInO_3$ materials singly-doped with Tb^{3+} and Eu^{3+} prepared through a Pechini-type sol-gel process [80], [81]. Another significant paper has confirmed that Bi^{3+} single-doped $LaInO_3$ is an efficient blue-emission luminescent material [82]. These results demonstrate how $LaInO_3$ can be an excellent host for rare earth ions and Bi^{3+}. For this reason, we have prepared several samples of $LaInO_3$ doped with Bi^{3+}, Tb^{3+} and Eu^{3+} ions via a flux solid-state reaction technique and investigated them by PXRD and optical spectroscopy.

2. Experimental and Characterization

2.1. Materials

A series of $LaInO_3$: $y\%Tb^{3+}$ ($y = 1, 2, 5, 10, 20, 50$), $LaInO_3$: $1\%Bi^{3+}/y\%Tb^{3+}$ ($y = 0, 1, 2$ and 3), $LaInO_3$: $10\%Tb^{3+}/z\%Eu^{3+}$ ($z = 1, 2, 3$), $LaInO_3$: $x\%Bi^{3+}/10Tb^{3+}/z\%Eu^{3+}$ ($x = 1, z = 0.1, 0.2, 0.3$) were synthesized via a flux solid-state reaction technique as described in ref. [83]. The dopant ions substituted for La^{3+}.

2.2. Experimental methods

X-ray diffraction (XRD) patterns were collected using a Thermo ARL X'TRA powder diffractometer, in Bragg-Brentano geometry, with a Cu-anode as X-ray source and a Peltier Si (Li) cooled solid state detector with a scan rate of 1.2°/min and an integration time of 1.5 s in 5-90° 2θ range. Luminescence spectra and decay curves were measured by a Fluorolog 3 (Horiba-Jobin Yvon) spectrofluorometer. The equipment was composed of a Xe lamp, a double excitation monochromator and a single emission monochromator (mod. HR320). The emitted signal was detected by means of photomultiplier in the photon counting mode. For the measurement of the decay curves, time correlated single photon counting technique (TCSPC) was used, with a xenon

microsecond pulsed lamp as excitation source. The decay curves were fitted by appropriate software. All the measurements were performed at room temperature.

3. Results and discussion

3.1. Structural investigation

Neat $LaInO_3$ crystallizes in the orthorhombic Pnma (62) space group [PDF card No. 08-0148]. As shown in Figure. 1, the In^{3+} ion is 6-fold coordinated and lies on a center of symmetry, whilst the La^{3+} ion is 8-fold coordinated lying on a plane of symmetry.
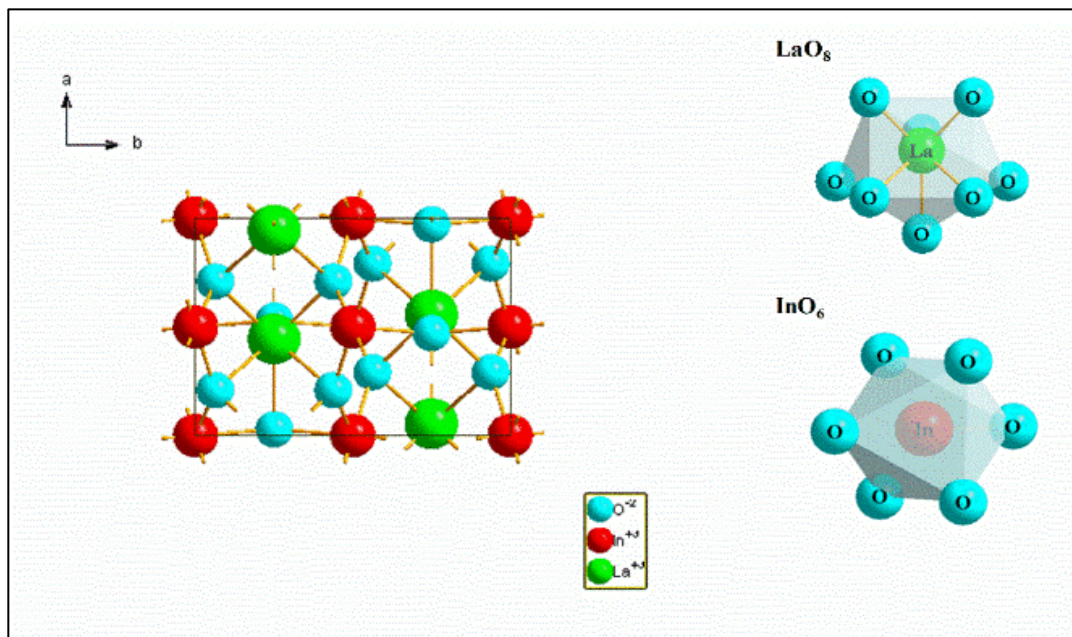
Figure. 1. The crystal structure of $LaInO_3$.
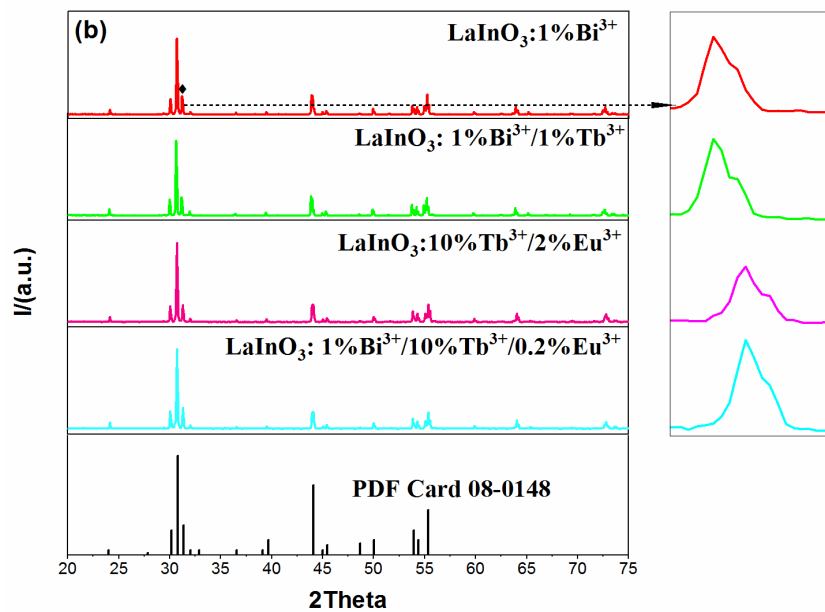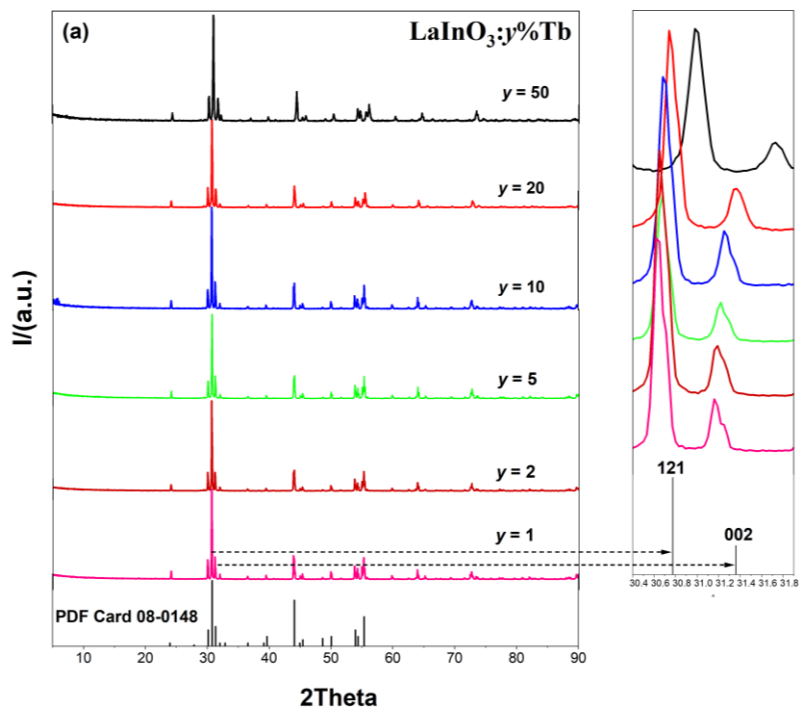
Figure. 2. (a) PXRD patterns of LaInO$_3$: y% Tb^{3+} (y = 1, 2, 5, 10, 20, 50); (b) PXRD patterns of LaInO$_3$: 1%Bi^{3+}/y%Tb^{3+} (y = 0, 1) and LaInO$_3$: x%Bi^{3+}/10%Tb^{3+}/z%Eu^{3+} (x = 0, z = 2; x = 1, z = 0.2).

The effective ionic radii of La^{3+} and In^{3+} are 1.16 Å (CN = 8) and 0.8Å (CN = 6), respectively [53]. Considering the valence states and ionic radii of dopant and substituted ions, the Bi^{3+} dopant (whose effective ionic radii is 1.17 Å, CN = 8) can easily substitute La^{3+} ions in the $LaInO_3$ host. With a similar reasoning, we expect the La^{3+} substitution also in the case of Tb^{3+} and Eu^{3+} dopant ions, in fact, the radii of Tb^{3+} and Eu^{3+} are 1.04 Å and 1.066 Å (CN = 8), respectively. As shown in Figure. 2, the obtained compounds are all pure phases as no extra peaks belonging to impurities are detected. Furthermore, the desired Tb (Eu)/La substitution is confirmed by the shift of the diffraction peaks towards higher 2θ values, as the percentage of dopants increase (see figure 2). This behavior is compatible with a shrinking of the crystal lattice in agreement with the smaller ionic radii of Tb^{3+} and Eu^{3+} with respect to that of La^{3+}.

3.2. Luminescence spectroscopy

3.2.1. Energy levels of luminescent ions

The energy level diagram of Bi^{3+}, Tb^{3+} and Eu^{3+} ions are shown in Figure. 3. It is well-known that the luminescence behavior of Bi^{3+} ions is greatly influenced by the surrounding lattice [84], but it always emits blue light in the $LaInO_3$ host.
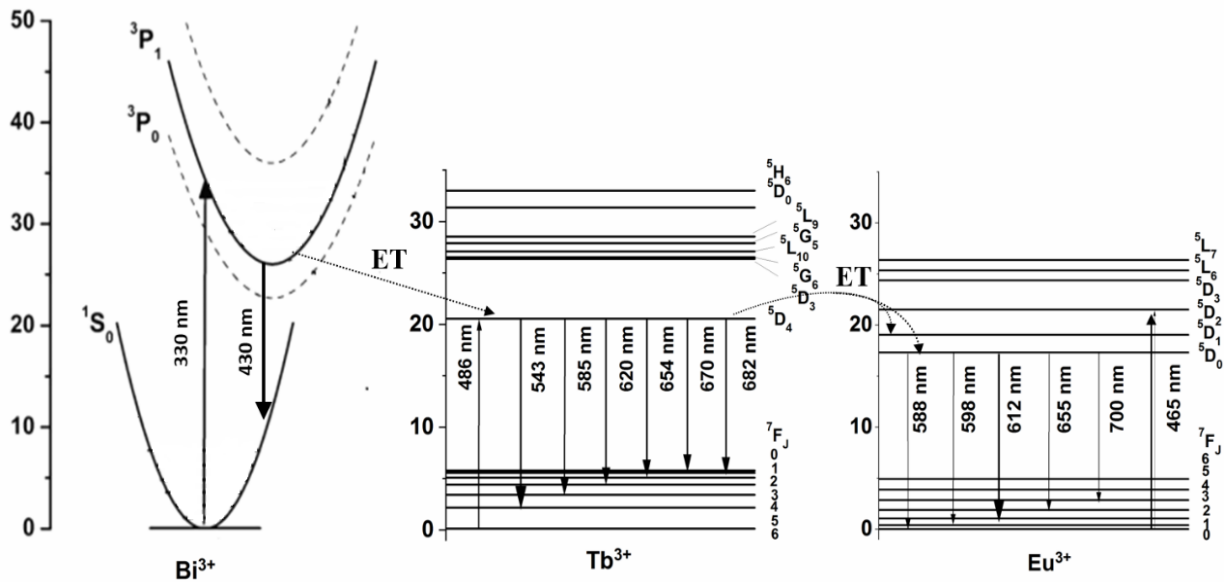
Figure. 3. The energy level diagrams of Bi^{3+}, Tb^{3+} and Eu^{3+} ions in the host $LaInO_3$.

Bi^{3+} ions absorb excitation energy at 330 nm, which induced the transition from the ground state $^1S_0$ to the excited $^3P_1$ state, and then relax to the $^1S_0$ level with blue emission at 430 nm.

When the Tb^{3+} ions are co-doped, the energy transfer occurs between $Bi^{3+} \rightarrow Tb^{3+}$ ions. The excitation energy of Bi^{3+} ion is transferred to Tb^{3+} $^5D_4$ level instead of $^5D_3$ level, as no significant peaks of blue emission can be observed. Subsequently, the electrons $^5D_4$ level relax to the ^7F_J level (J = 5, 4, 3), resulting in the green emission of Tb^{3+}. Besides, the energy transfer $Tb^{3+} \rightarrow Eu^{3+}$ ions can occur from the $^5D_4$ level of Tb^{3+} to $^5D_1$ and $^5D_0$ levels of Eu^{3+}, the main mechanisms involving in this process are $^5D_4$ (Tb^{3+}) + $^7F_0$ (Eu^{3+}) $\rightarrow$ $^7F_6$ (Tb^{3+}) + $^5D_1$ (Eu^{3+}) and $^5D_4$ (Tb^{3+}) + $^7F_0$ (Eu^{3+}) $\rightarrow$ $^7F_4$ (Tb^{3+}) + $^5D_0$ (Eu^{3+}). This emission originates from $^5D_0$ level to ^7F_J (J = 1, 2, 3, 4), which gives rise to a visually dominant red color. Based on this interpretative scheme, the luminescence spectroscopy of the materials under investigation is discussed in the sections below for the various doping schemes.

3.2.2. LaInO$_3$ singly doped with Bi^{3+} and Tb^{3+} ions

The excitation and emission spectra of $LaInO_3$: 1%Bi^{3+} and $LaInO_3$: 10%Tb^{3+} are shown in Figure. 4. It can be seen from Figure. 4(a) that the excitation and emission spectra of Bi^{3+} ions are both broad bands and the maxima are located at about 330 nm ($^1S_0 \rightarrow {^3P_1}$) and 430 nm ($^3P_1 \rightarrow {^1S_0}$), respectively. This behavior is similar to the results reported in previously published paper [82]. Interestingly, the excitation band falls in the NUV region, and the materials emits blue light peaking at 430 nm.
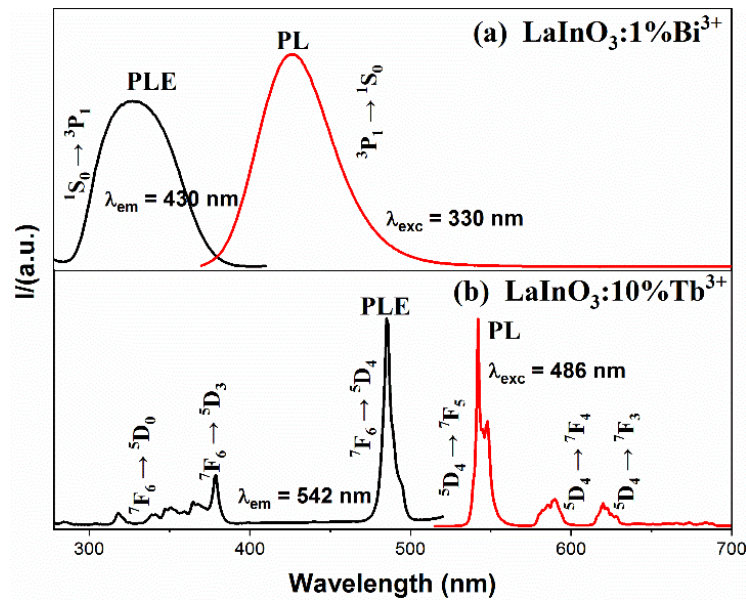
Figure. 4. The excitation and emission spectra of (a) LaInO$_3$: 1%Bi^{3+} and (b) LaInO$_3$: 10%Tb^{3+}.

As shown in Figure. 4(b), the characteristic excitation and emission spectra of Tb^{3+} ion consists of several sharp lines. The excitation spectrum monitoring at 542 nm shows major peaks at 317, 378 and 486 nm, which corresponds to $^7F_6 \rightarrow {}^5D_0$, $^7F_6 \rightarrow {}^5D_3$ and $^7F_6 \rightarrow {}^5D_4$ transitions, respectively. Upon excitation at 486 nm, three main emission peaks located at 543, 589 and 620 nm are detected, corresponding to the $^5D_4 \rightarrow {}^7F_J$ (J = 5, 4, 3) transitions, respectively. Besides, a spectral overlap could be intuitively observed between the emission spectrum of Bi^{3+} and excitation spectrum of Tb^{3+} ions. Thus, the energy transfer process is in principle possible from Bi^{3+} to Tb^{3+} ions in $LaInO_3$ host.

3.2.3. $LaInO_3$: Tb^{3+} co-doped with Bi^{3+} and Eu^{3+} ions

The excitation and emission spectra of $LaInO_3$: $1\%Bi^{3+}/2\%Tb^{3+}$ are shown in Figure. 5.
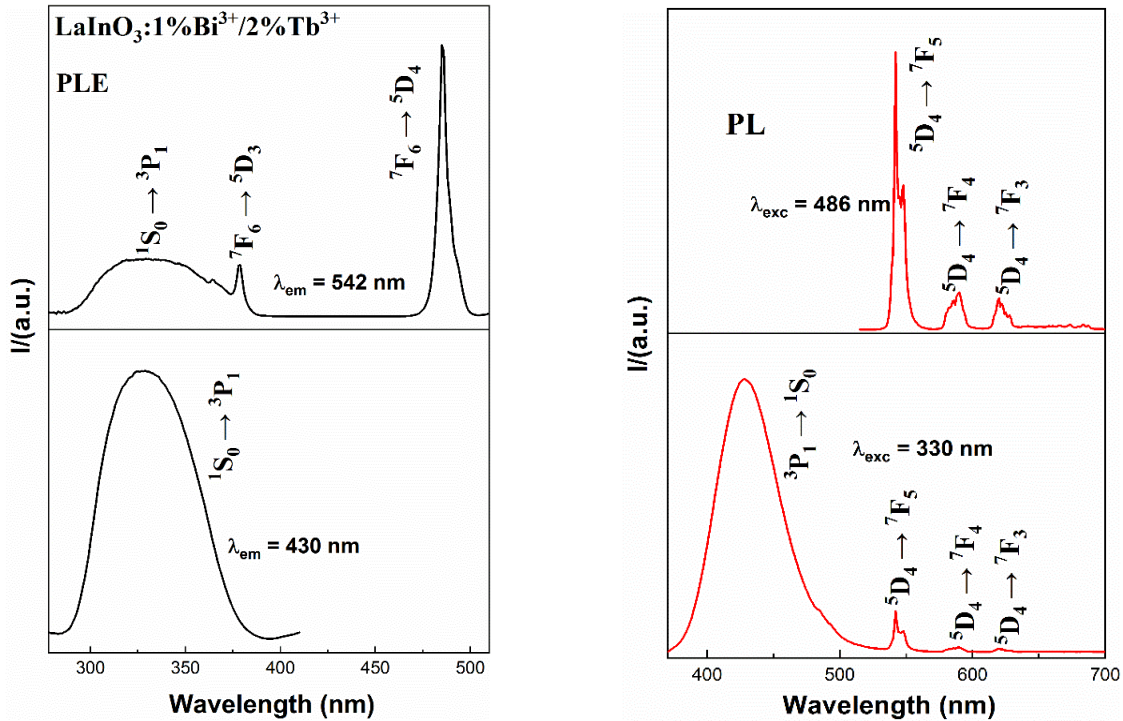
Figure. 5. The excitation (left) and emission (right) spectra of $LaInO_3$: $1\%Bi^{3+}/2\%Tb^{3+}$.

Upon monitoring the emission around 430 nm, only the characteristic excitation band ascribed to Bi^{3+} ions could be observed, whilst upon monitoring the emission of Tb^{3+} around 542 nm, the excitation peaks of both Bi^{3+} and Tb^{3+} are clearly visible around 330 nm ($^1S_0 \rightarrow {}^3P_1$ of Bi^{3+}) and 486 nm ($^7F_6 \rightarrow {}^5D_4$ of Tb^{3+}). Consequently, upon excitation around 330 nm, both the emission peaks of Bi^{3+} and Tb^{3+} are detected. Furthermore, upon excitation at 486 nm, only emission

stemming from Tb^{3+} is observed. This confirms the presence of a unidirectional energy transfer from Bi^{3+} to Tb^{3+} ions.

The excitation and emission spectra of $LaInO_3$: $10\%Tb^{3+}/1\%Eu^{3+}$ are shown in Figure. 6.
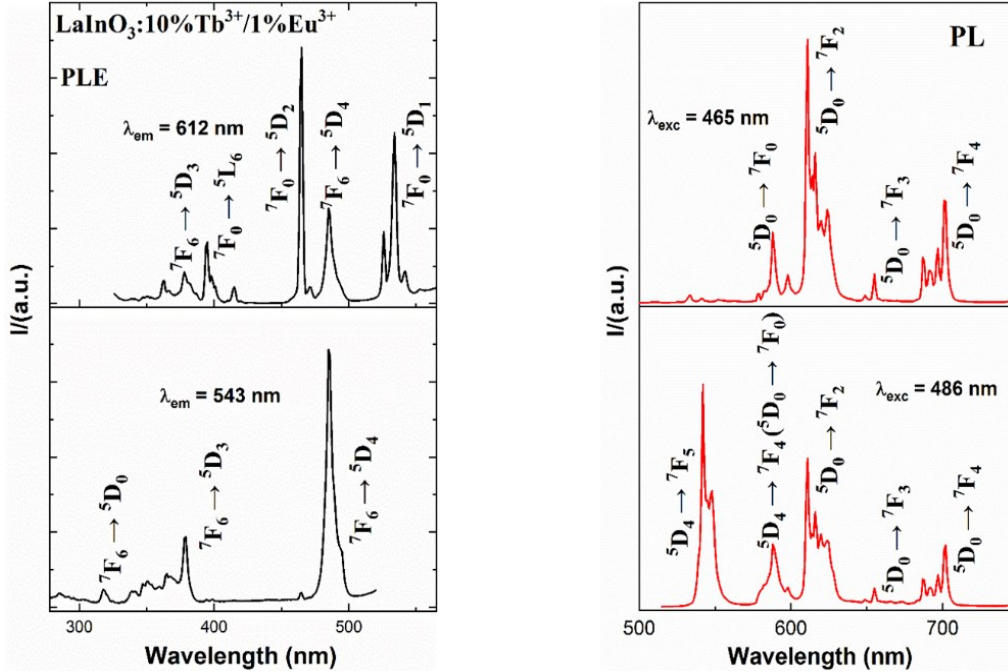
Figure. 6. The excitation (left) and emission (right) spectra of $LaInO_3$: $10\%Tb^{3+}/1\%Eu^{3+}$.

Whilst the Tb^{3+} luminescence around 543 nm could be sensitized only by excitation into the Tb^{3+} excited states ($^5D_0$, $^5D_3$ and $^5D_4$), the Eu^{3+} luminescence around 612 nm is sensitized by both excitation into Tb^{3+} and Eu^{3+} ions excited states ($^5D_3$, $^5D_4$ of Tb^{3+} and $^5L_6$, $^5D_2$ and $^5D_1$ of Eu^{3+}; figure. 6). In agreement, upon excitation at 486 nm (into Tb^{3+} excited state), both luminescence from Tb^{3+} and Eu^{3+} occurs. However, the excitation of Eu^{3+} into the $^5D_2$ state (at 465 nm) results solely in Eu^{3+} with emission at 588 nm ($^5D_0 \rightarrow {}^7F_1$), 612 nm ($^5D_0 \rightarrow {}^7F_2$), 655 nm ($^5D_0 \rightarrow {}^7F_3$) and 700 nm ($^5D_0 \rightarrow {}^7F_4$). This implies the presence of a unidirectional $Tb^{3+} \rightarrow Eu^{3+}$ energy transfer process, as previously discussed by our group [36], [39], [78], [79], [86]–[87].

The emission spectrum of $LaInO_3$: $1\%Bi^{3+}/yTb^{3+}$ ($y = 1\%$, 2% and 3%) under excitation around 330 nm, within the Bi^{3+} absorption band is shown in Figure. 7(a).
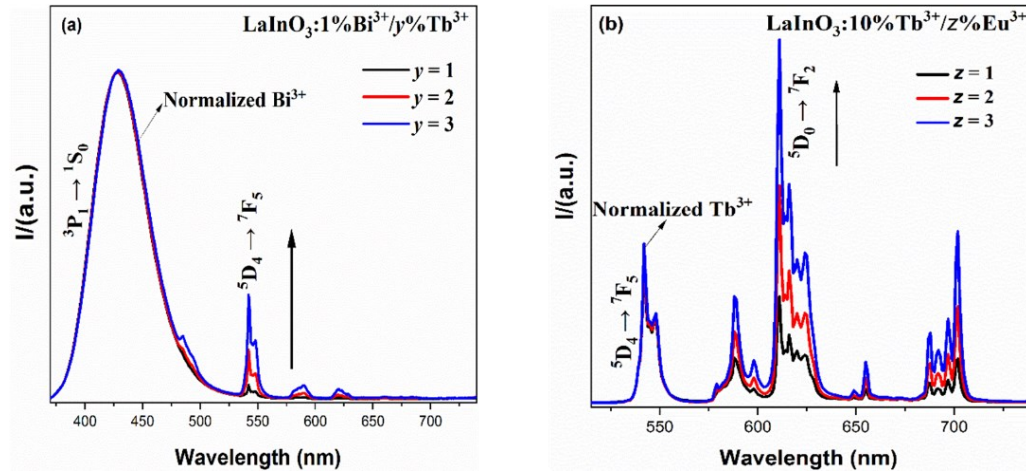
Figure. 7. Relative emission spectra of LaInO$_3$: Tb^{3+} co-doped Bi^{3+} (a) and Eu^{3+} (b). Both spectra are normalized to the Bi^{3+} and Tb^{3+} emission, respectively.

As the concentration of Tb^{3+} increases, the emission intensity increases as well, as expected. The emission spectra of LaInO$_3$: 10%Tb^{3+}/z%Eu^{3+} ($y = 1$, 2 and 3) upon excitation at 486 nm and normalized to the area of the $^5D_4 \rightarrow ^7F_5$ transition of Tb^{3+} is shown in figure 7(b). Also in this case, as the concentration of co-dopant (Eu^{3+}) increases, the intensity of its emission bands increases. All the spectra reported in figure 7 agree with the existence of Bi$^{3+} \rightarrow$ Tb^{3+} and Tb$^{3+} \rightarrow$ Eu^{3+} energy transfer process.

In Figure. 8, the room temperature decay curves of Bi^{3+} (Figure. 8a) and of the $^5D_4$ excited state of Tb^{3+} (Figure. 8b) at are shown for LaInO$_3$: Bi^{3+}/ Tb^{3+} and LaInO$_3$: Tb^{3+}/ Eu^{3+}.
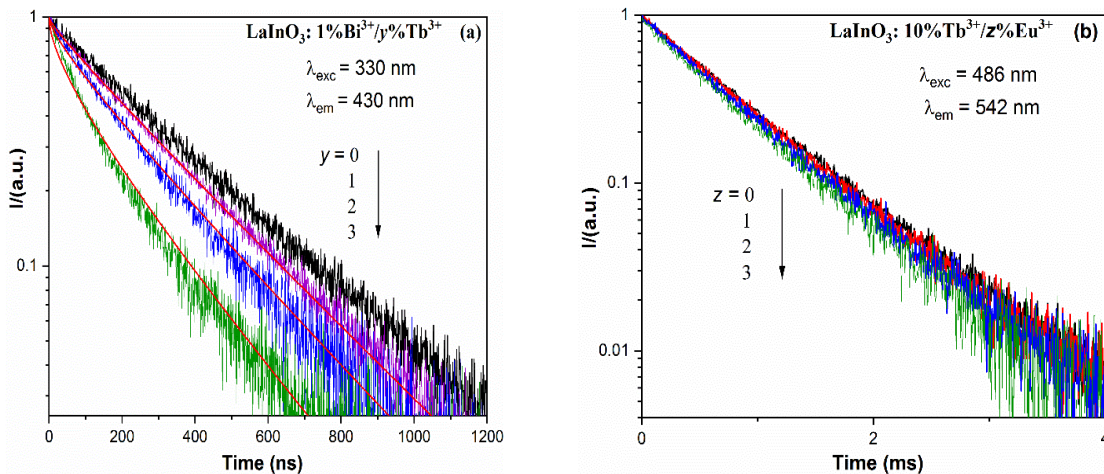
Figure. 8. The decay curves of Bi^{3+} excited state in LaInO$_3$: Bi^{3+}/Tb^{3+} (the solid lines in red color correspond to the Inokuti–Hirayama model with s = 6) (a). The decay curves of $^5D_4$ excited state of Tb^{3+} in LaInO$_3$: Tb^{3+}/ Eu^{3+} (b).

35

It could be seen from the Figure. 8(a) that the decay profile of Bi^{3+} excited state (when $y = 0$) is single exponential with decay constant of 316 ns, which is basically consistent with the results present in the previous published paper about Bi^{3+} in the same host [85]. The deviation from the single exponential behavior is observed with the increment of Tb^{3+} concentration, thus the first *e*-folding time of Bi^{3+} excited state is 273, 213, 130 ns (when $y = 1, 2, 3$), respectively. Moreover, the energy transfer efficiency η_T can be calculated by the following equation [96]:

$$\eta_T = 1 - \frac{\tau_{Bi-Tb}}{\tau_{Bi}} \qquad (1)$$

Here, τ_{Bi} and τ_{Bi-Tb} are the decay time in the absence and presence of Tb^{3+} ions, respectively. Through calculation, the resulting values of η_T are 14%, 32.6% and 58.9%, respectively. As shown in Figure. 8(b), all decay profiles of $^5D_4$ state of Tb^{3+} ions are single exponential with decay constants of 0.76, 0.73, 0.70, 0.68 ms (when $z = 0, 1, 2, 3$), respectively. In this case, the energy migration in the donor subset may become dominant because of the higher concentration of donors, which results in the exponential profile. It has been reported that the decay time of $LaInO_3$: 5%Tb^{3+} is 1.21 ms [80], the lower value for $LaInO_3$: 10%Tb^{3+} (0.76 ms) is reasonably due to concentration quenching. The energy transfer efficiencies η_T determined according to equation. (1) are 3.9%, 7.9% and 10.5%, respectively. Obviously, the energy transfer efficiencies increase with the concentration of Eu^{3+} ions. This is mainly due to a decrease of the Tb/Eu interionic distances, responsible for an increase of the energy transfer probability from the donor to the acceptor optical centers [36]. This applies to all the existing non-radiative energy transfer mechanisms.

To further study the non-exponential nature of decay profiles of the Bi^{3+} in $LaInO_3$: 1%Bi^{3+}/y%Tb^{3+} (when $y = 1, 2, 3$), the Inokuti–Hirayama model is adopted due to the lower concentration of donors. This model is specified for weak donor-donor transfer and negligible migration. The time evolution of the emission intensity I in this model is described by the equation [36]:

$$I(t) = I_0 exp\left(-\frac{t}{\tau_0} - \alpha(\frac{t}{\tau_0})^{3/s}\right) \qquad (2)$$

and

$$\alpha = \frac{4}{3} \pi \Gamma(1 - \frac{3}{s}) N_A R_c{}^3 \qquad (3)$$

where I_0 is the initial intensity, Γ is the gamma function, $s = 6, 8, 10$ for electric dipole-electric dipole (EDD), electric dipole-electric quadrupole (EDQ) and electric quadrupole-electric quadrupole (EQQ) interaction, respectively, and N_A is the acceptor concentration (ions cm^{-3}). R_c is defined as the critical distance, at which the probabilities of transfer and internal decay for the isolated donor $\tau_0{}^{-1}$ are identical. The three transfer mechanisms EDD, EDQ and EQQ have been considered and the fit for s = 6 results much better than those with s = 8 or 10. The values estimated with s = 6 for the critical distance R_c lie in the reasonable range 5.8 - 6.7 Å. Hence, it is possible to propose that non-radiative Bi^{3+} → Tb^{3+} energy transfer is dominated by EDD mechanism.

Based on the recorded luminescence spectra, the Commission International de l'Eclairage (CIE) chromaticity diagram of LaInO$_3$: 1%Bi^{3+}/y%Tb^{3+} upon 330 nm excitation and of LaInO$_3$: 10%Tb^{3+}/z%Eu^{3+} upon 486 nm excitation is reported in Figure. 9.
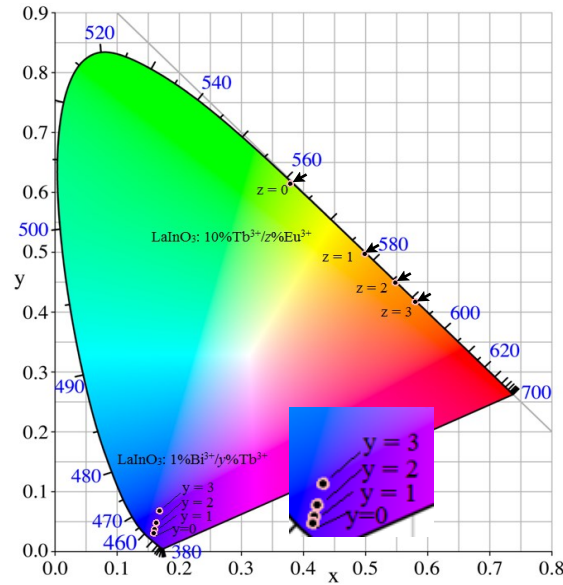
Figure. 9. CIE chromaticity diagram of the LaInO$_3$: 1%Bi^{3+}/y%Tb^{3+} phosphors (y = 0, 1, 2, 3) and LaInO$_3$: 10%Tb^{3+}/z%Eu^{3+} (z = 0, 1, 2, 3).

Inspection of the figure shows that the color of LaInO$_3$: 1%Bi^{3+}/y%Tb^{3+} changes from dark blue to light blue with the increment of Tb^{3+} concentration. Also, the luminescence color of

LaInO$_3$: 10%Tb^{3+}/z%Eu^{3+} is shifted from green to red as the concentration of Eu^{3+} increased. Hence, the energy transfer process is an effective tool to obtain tunable luminescence. The CIE parameters are summarized in Table.1, and the color purity of LaInO$_3$ single-doped with Bi^{3+} and Tb^{3+} are evaluated by the following expression [86]:

$$\text{Color purity} = \left.\sqrt{(X - X_i) + (Y - Y_i)} \middle/ \sqrt{(X_d - X_i) + (Y_d - Y_i)} \right. \times 100\% \qquad (4)$$

where (X, Y) are the CIE coordinates of the LaInO$_3$: 1%Bi^{3+} and LaInO$_3$: 10%Tb^{3+} samples; (X_d, Y_d) are the CIE coordinates at the dominant wavelength of 430 and 542 nm, respectively; (X_i, Y_i) is the CIE coordinate of the standard white illumination. Here, (X_d, Y_d) = (0.1695, 0.0064), (0.2441, 0.7426), respectively. (X_i, Y_i) = (0.313, 0.329). By calculation based on the equation. (4), the color purity was determined to be about 98.5 % for LaInO$_3$: 1%Bi^{3+} and 100% for LaInO$_3$: 10%Tb^{3+}. The results show that LaInO$_3$ single-doped with Bi^{3+} and Tb^{3+} could be useful blue and green-emission materials.

Table. 1 CIE parameters of LaInO$_3$: 1%Bi^{3+}/y%Tb^{3+} materials (y = 0, 1, 2, 3) and LaInO$_3$: 10%Tb^{3+}/z%Eu^{3+} (z = 0, 1, 2, 3)

Samples	CIE coordinate (x, y)
LaInO$_3$: 1%Bi^{3+}	(0.1585, 0.0305)
LaInO$_3$: 1%Bi^{3+}/1%Tb^{3+}	(0.1595, 0.0372)
LaInO$_3$: 1%Bi^{3+}/2%Tb^{3+}	(0.1630, 0.0484)
LaInO$_3$: 1%Bi^{3+}/3%Tb^{3+}	(0.1686, 0.0683)
LaInO$_3$: 10%Tb^{3+}	(0.3783, 0.6144)
LaInO$_3$: 10%Tb^{3+}/1%Eu^{3+}	(0.4984, 0.4973)
LaInO$_3$: 10%Tb^{3+}/2%Eu^{3+}	(0.5479, 0.4491)
LaInO$_3$: 10%Tb^{3+}/3%Eu^{3+}	(0.5803, 0.4175)

3.2.4. LaInO$_3$ triply doped with Bi^{3+}, Tb^{3+} and Eu^{3+}

The excitation spectra of LaInO$_3$: 1%Bi^{3+}/10%Tb^{3+}/1%Eu^{3+} are monitored at the emission of 430, 542 and 612 nm, respectively. Since both Bi^{3+} and Tb^{3+} excitation peaks are present in the excitation spectrum of Eu^{3+} around 612 nm, we could conclude that Eu^{3+} luminescence can be sensitized by Bi^{3+} and Tb^{3+}. As expected, the emission at 430 nm could only be sensitized by Bi^{3+} and no Tb^{3+} and Eu^{3+} excitation peaks are present in the excitation spectrum of Bi^{3+}. The emission spectra in figure 10 are obtained upon excitation at 330 nm, 465 nm, and 486 nm, respectively. The excitation at 486 nm gives rise to the emission of both Tb^{3+} and Eu^{3+} ions, whilst the excitation at 465 nm produces only the Eu^{3+} emission. Upon excitation at 330 nm, the emission bands related to Bi^{3+}, Tb^{3+} and Eu^{3+} are clearly detected, because of the double energy transfer process (Bi^{3+} → Tb^{3+} → Eu^{3+}). What's more, the presence of a Bi^{3+} → Eu^{3+} energy transfer channel cannot be ruled out, which is consistent with a previous paper [87]. This result shows the potential of LaInO$_3$: xBi^{3+}/yTb^{3+}/zEu^{3+} as white light emission material.
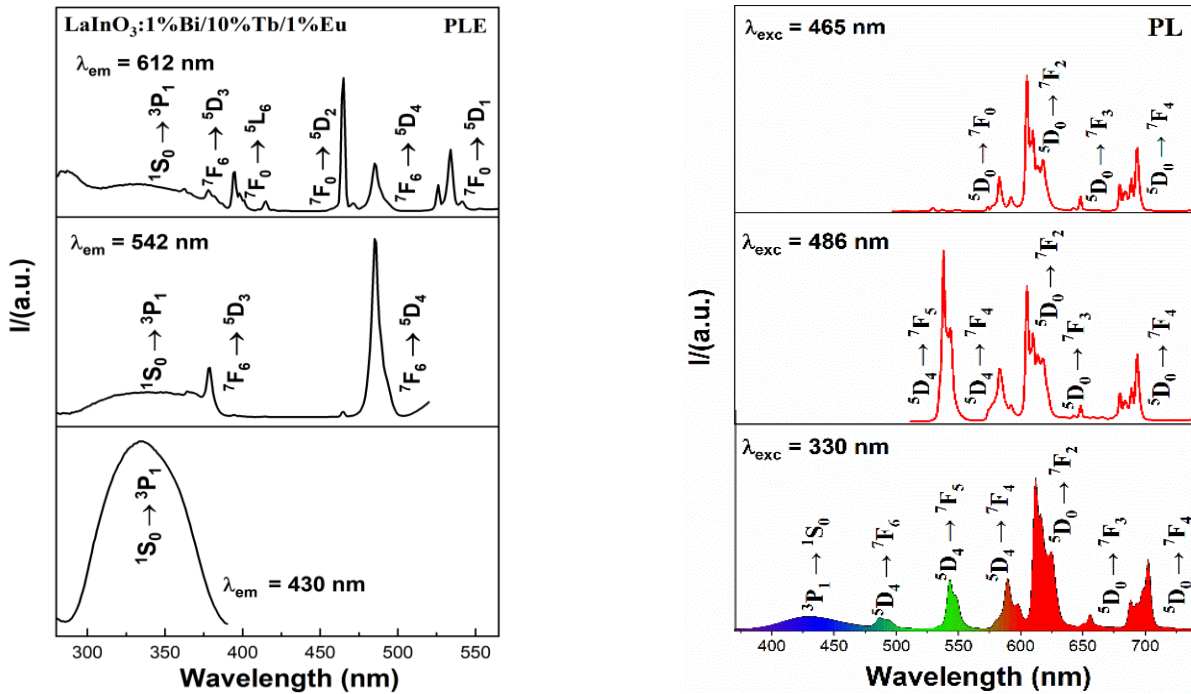
Figure.10. The excitation (left) and emission (right) spectra of LaInO$_3$: 1%Bi^{3+}/10%Tb^{3+}/1%Eu^{3+}.

Based on the obtained results, LaInO$_3$: 1%Bi^{3+}/10%Tb^{3+}/z%Eu^{3+} (z = 0.1, 0.2 and 0.3) samples were prepared. The Commission International de I'Eclairage (CIE) chromaticity diagram is depicted in Figure. 11.
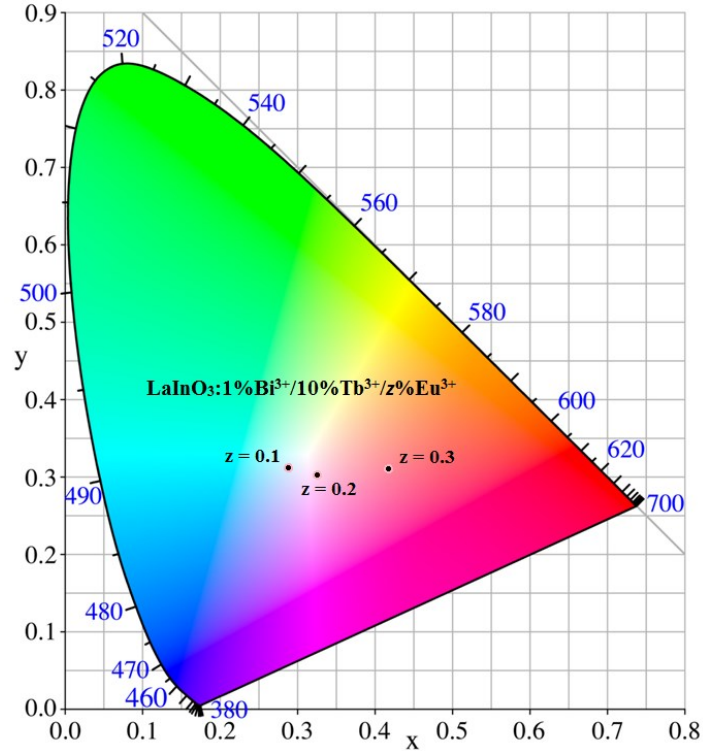
Figure. 11. CIE chromaticity diagram of the LaInO$_3$: 1%Bi^{3+}/10%Tb^{3+}/z%Eu^{3+} (z = 0.1, 0.2, 0.3) upon 330 nm excitation.

It could be seen that the luminescence color changed from blue to red with the increment of Eu^{3+} concentration, and it is close to white at z = 0.2. The CIE parameters of these materials are summarized in Table.2.

Table. 2 CIE parameters of LaInO$_3$: 1%Bi^{3+}/10%Tb^{3+}/z%Eu^{3+} materials (z = 0.1, 0.2, 0.3)

Samples	CIE coordinate (x, y)
Standard white light	(0.313, 0.329)
LaInO$_3$: 1%Bi^{3+}/10%Tb^{3+}/0.1%Eu^{3+}	(0.288, 0.312)
LaInO$_3$: 1%Bi^{3+}/10%Tb^{3+}/0.2%Eu^{3+}	(0.325, 0.303)
LaInO$_3$: 1%Bi^{3+}/10%Tb^{3+}/0.3%Eu^{3+}	(0.417, 0.311)

4. Conclusions

A series of doubly doped $LaInO_3$: Bi^{3+}/Tb^{3+} and $LaInO_3$: Tb^{3+}/Eu^{3+} and triply doped $LaInO_3$: $Bi^{3+}/Tb^{3+}/Eu^{3+}$ samples have been synthesized via a flux solid-state reaction technique. The energy transfer mechanisms $Bi^{3+} \rightarrow Tb^{3+}$ and $Tb^{3+} \rightarrow Eu^{3+}$ ions have been explored in co-doped samples. Besides, the luminescence spectroscopy of triply doped compounds has also been investigated and a double energy transfer processes $Bi^{3+} \rightarrow Tb^{3+} \rightarrow Eu^{3+}$ has been proposed. Upon excitation in the NUV spectral region (at 330 nm), the $LaInO_3$: $1\%Bi^{3+}/10\%Tb^{3+}/0.2\%Eu^{3+}$ sample exhibits an almost white colored luminescence.

Chapter 4

Energy transfer processes in NaBiF$_4$ doped with Tb^{3+} and Eu^{3+} and their luminescence properties in aqueous phase

Abstract：A design of NaBiF$_4$ doped with Tb^{3+} and Eu^{3+} has been proposed, and the samples were synthesized successfully via a facile and fast route at room temperature. And powder X-ray diffraction (PXRD) and luminescence spectroscopy are employed to characterize and investigate samples. Pure hexagonal phase NaBiF$_4$ (PDF card No. 41-0796) is displayed and no extra peaks belonging to impurities are detected. The study of luminescence spectroscopy and decay kinetics of the $^5D_4$ excited state of Tb^{3+} provides strong evidence for Tb^{3+} → Eu^{3+} energy transfer process. Sodium citrate is adopted as a capping agent to facilitate samples dissolving into water completely. The luminescence properties of citrate stabilized samples and corresponding aqueous phase are also monitored, and an enhancement of luminescence for former and severe quenching for latter can be observed.

Keywords: energy transfer, rare earth ion, luminescence, sodium citrate

1. Introduction

NaBiF$_4$ has received appreciable attention these days, which is attributed to its facile synthesis, excellent performance, and low cost for the substitution of expensive rare earth elements with bismuth in host [88]. According to the reported literature, Eu^{3+} and Tb^{3+} ions have been introduced into NaBiF$_4$ to emit red and green light, respectively [89], [90] Based on the previous research in our group, the energy transfer from Tb^{3+} to Eu^{3+} can happen in various hosts, but the advanced efficiency is highly needed and usually associated with diverse factors such as materials structure [39], [40], dopants concentration [79]. Since the brilliant luminescence property of Tb^{3+} and Eu^{3+} has been stated in NaBiF$_4$, the energy transfer Tb^{3+}→Eu^{3+} is supposed to occur. Additionally, no relevant report about Tb^{3+}/Eu^{3+} co-doped NaBiF$_4$ so far.

The numerous published papers have reported the phosphors NaBiF$_4$ doped with rare earth ions mostly possess distinct temperature sensing performance [91], [92], and Tb^{3+} and Eu^{3+} are regarded as important ions pair for optical thermometry because of their different luminescence thermal-quenching trends [93], [94]. As a hot topic, the luminescence properties varied with

temperature of Tb^{3+}/Eu^{3+} co-doped $NaBiF_4$ may be worthy of exploration. Importantly, the poor solubility and extreme hypersensitivity of $NaBiF_4$ to water proposed by other groups [95], limits its potential application in biological fields. Therefore, surface modification is significant for this drawback. An enhancement of water-resistance for Poly (acrylic acid) (PAA)-and citric acid monohydrate (CA)-modified $NaBiF_4$ nanoparticles have been reported [96]. It is interesting to discover more suitable capping agents and explore their effect on luminescence properties.

In this work, samples $NaBiF_4$ doped with Tb^{3+} and Eu^{3+} ions have been successfully synthesized via a facile and fast route at room temperature, and sodium citrate was exploited as capping agent. The materials were characterized by powder X-ray diffraction (PXRD) and optical spectroscopy.

2. Experimental and Characterization

2.1. Material

2.1.1. NaBiF₄: $x\%Tb^{3+}/y\%Eu^{3+}$

The materials were successfully synthesized via a facile and fast method. For samples $NaBi_{1-x}Tb_xF_4$ (x mmol, x = 0.05, 0.1, 0.25, 0.5, 0.7, 1.0), $NaNO_3$ (2 mmol), stoichiometric $Bi(NO_3)_3 \cdot 5H_2O$ and $Tb(NO_3)_3 \cdot 6H_2O$ were dissolved in ethylene glycol (10 mL) by magnetic stirring at room temperature to form homogeneous solution A. Next, NH_4F (22 mmol) was added into ethylene glycol (20 mL) with magnetic stirring at room temperature to form homogeneous solution B. Then solution A was mixed with solution B, and the mixture was vigorously stirred for 1.5 min at 35 °C. Subsequently, the resultants were filtered and washed 2-3 times with anhydrous ethanol and deionized water, respectively. Then, the samples were obtained after air drying for 6 h at 80 °C. For samples $NaBi_{1-x-y}Tb_xEu_yF_4$, the same method was used as described above except a suitable amount of $Eu(NO_3)_3 \cdot 5H_2O$ was added.

2.1.2. Citrate stabilized NaBiF₄: $x\%Tb^{3+}/y\%Eu^{3+}$

The citrate stabilized $NaBiF_4$: $x\%Tb^{3+}/y\%Eu^{3+}$ were prepared with 10 mg bare samples and an excess of sodium citrate. First, an excess of sodium citrate was dissolved completely in 1 mL deionized water, and 10 mg bare samples were added and stirred for few minutes, then the solutions underwent the ultrasonic treatment until clear. Finally, the resultant mixtures were washed to remove the superfluous sodium citrate and the obtained precipitation was dissolved with another 1 mL deionized water for further use.

2.2. Experimental methods

X-ray diffraction (XRD) measurement: XRD patterns were collected using a Thermo ARL X'TRA powder diffractometer, in Bragg-Brentano geometry, with a Cu-anode as X-ray source and a Peltier Si (Li) cooled solid state detector with a scan rate of 1.2°/min and an integration time of 1.5 s in 5-90° 2θ range.

Luminescence spectra and decay curves measurement: A Fluorolog 3 (Horiba-Jobin Yvon) spectrofluorometer is used, and the equipment was composed of a Xe lamp, a double excitation monochromator and a single emission monochromator (mod. HR320). The emitted signal was detected by means of photomultiplier in the photon counting mode. For the measurement of the decay curves, time correlated single photon counting technique (TCSPC) was used, with a xenon microsecond pulsed lamp as excitation source.

Dynamic light scattering (DLS) measurement was performed via Malvern Zetasizer Nano ZS instrument. The electron microscopy was acquired by Transmission Electron Microscope FEI TECNAI G2 (TEM). The infrared absorption spectra were collected by means of a spectrophotometer Perkin-Elmer FT-IR Spectrum Two.

3. Results and discussion

3.1. Structural investigation

The XRD patterns of $NaBiF_4$: x% Tb phosphors (x = 5, 10, 25, 50, 70, 100) and the crystal structure of pure $NaBiF_4$ are shown in Fig. 1.
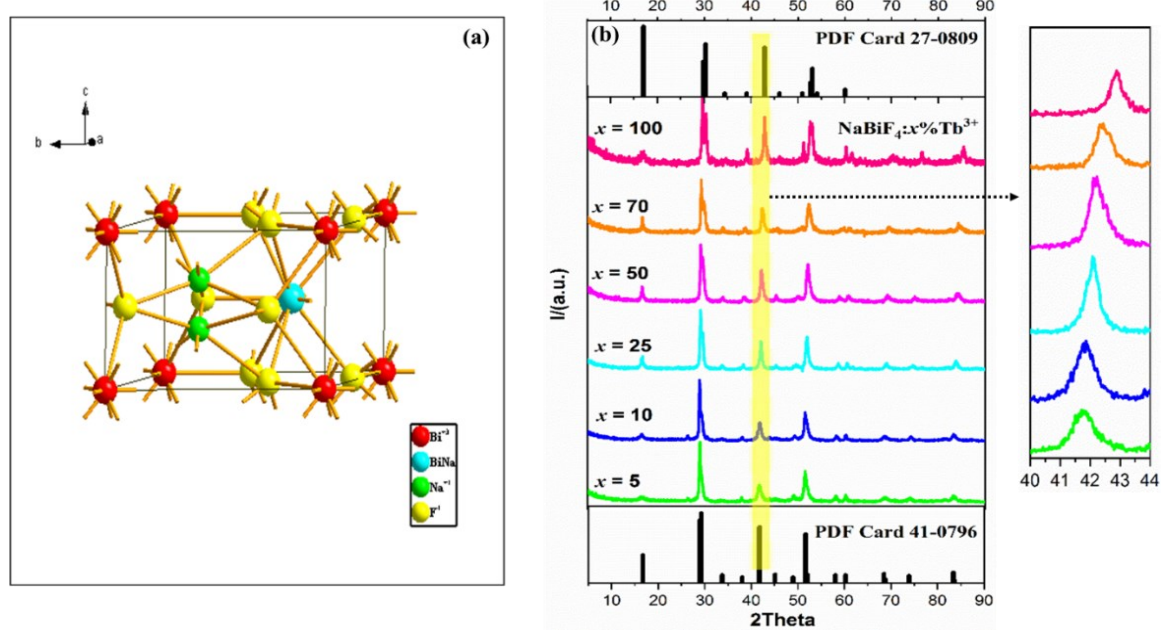
Figure. 1. (a) The crystal structure of NaBiF$_4$; (b) XRD patterns of NaBiF$_4$: x% Tb phosphors (x = 5, 10, 25, 50, 70, 100).

The pure NaBiF$_4$ crystallizes in the hexagonal *P-3* (147) space group [PDF card No. 41-0796]. Two inequivalent Bi^{3+} sites can be seen from Fig. 1(a), one is 9-fold coordinated (site 1a) and occupied by only Bi^{3+}, another one is 9-fold coordinated (site 1f) and it is occupied randomly by 1/2 Na$^+$ and 1/2 Bi^{3+}, and these two sites are of C$_{3h}$ point symmetry. The effective ionic radii of Bi^{3+}, Tb^{3+} and Eu^{3+} are 1.17 Å (CN = 8), 1.095 Å and 1.12 Å (CN = 9), respectively [53]. Therefore, the shift of the diffraction peaks towards higher 2θ values (smaller cell size) is expected when Bi^{3+} ions are replaced by the smaller Tb^{3+}(Eu^{3+}) ions.

XRD patterns of bare NaBiF$_4$: x% Tb phosphors (x = 5, 10, 25, 50, 70, 100) show the peaks for all samples are matched very well with the standard NaBiF$_4$ structure and no extra peaks belonging to impurities are detected. Although the hexagonal phase of NaTbF$_4$ [PDF card No. 27-0809] is exhibited when the content of Tb^{3+} increases to 100 mol%, the similar crystal phase between NaTbF$_4$ and NaBiF$_4$ is noteworthy. Furthermore, as said above, foregoing shift of peaks occurred as the percentage of Tb^{3+} increase (see figure 1(b)), which is in accordance with a shrinking of the crystal lattice result from the smaller ionic radii of Tb^{3+} substituting for Bi^{3+}.

Besides, the evolution of the unit cell parameters (a, b, c, and V) of bare NaBiF$_4$: x% Tb is given in Table 1. The variation of the parameters a and b as a function of x is presented in Fig. 2.

Table 1. The evolution of the unit cell parameters (a, b, c, and V) of bare NaBiF$_4$: x% Tb.

Crystal Parameters	$a = b$ (Å)	c (Å)	V (Å^3)
$x = 5$	6.1477	3.7159	140.4395
$x = 10$	6.1470	3.6992	139.7765
$x = 25$	6.1197	3.6719	137.5153
$x = 50$	6.0965	3.6530	135.7722
$x = 70$	6.0735	3.6142	133.3184
$x = 100$	6.0294	3.5688	129.7390
Theoretical	6.1440	3.7210	140.4630
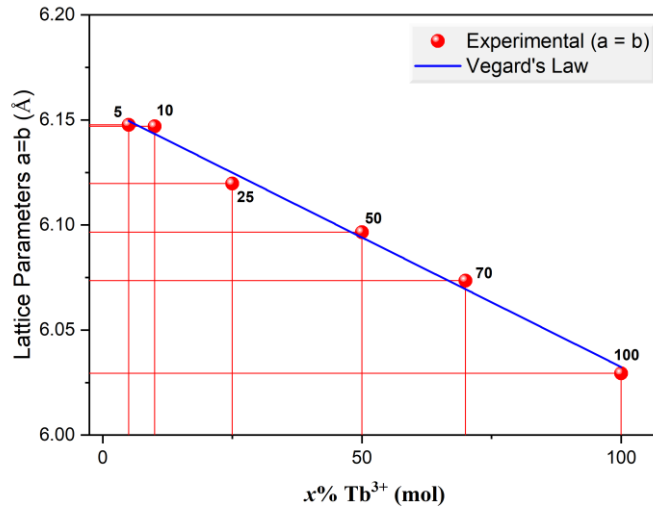
Figure. 2. The variation of the parameters a and b as a function of x in bare NaBiF$_4$: x% Tb. The solid line represents the fitting according to Vegard's law.

The decreasing values of the unit cell parameters a, b, c, and V are observed, which verified the shrinking of the crystal lattice mentioned above. A linear behavior of the cell parameters illustrates that the bare NaBiF4: x% Tb belongs to a continuous iso-structural solid solution, which follows the Vegard's law.
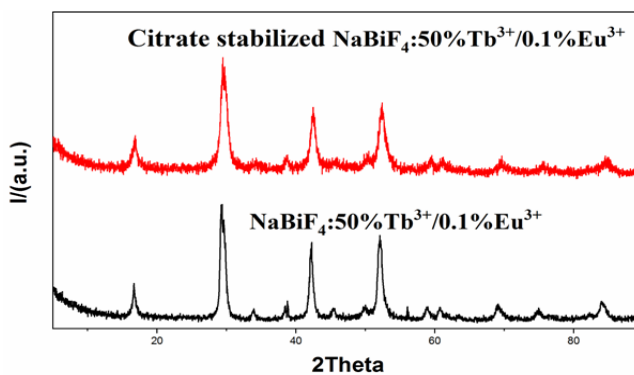
Figure. 3. The XRD patterns of bare and citrate stabilized samples NaBiF$_4$: 50%Tb^{3+}/0.1%Eu^{3+}.

The comparison of diffraction peaks between bare and citrate stabilized samples is applied to reveal the effect of sodium citrate on crystal structure (see figure 3), identical phases could be observed except the relatively big peaks broadening. It is assumed that sodium citrate can contribute to an increasing number of monodisperse crystal particles without structure transformation.

3.2. Dynamic light scattering and Electron microscopy measurement

Simultaneously, the zeta potential was measured to verify the existence of sodium citrate as capping agent in the citrate stabilized sample NaBiF$_4$: 50%Tb^{3+}/0.1%Eu^{3+}, the obtained value of -33.4 ± 0.32 mV signifies the presence of carboxyl groups of citrates on the crystal particles surface. Also, the size distribution was detected, the average size of the nanoparticles is 21 nm (see figure 4 (a)).
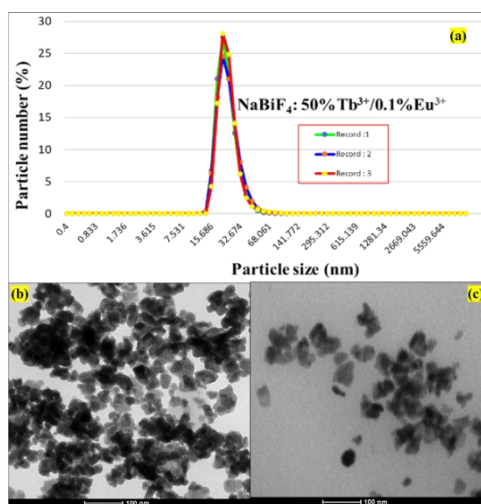
Figure. 4. (a) Hydrodynamic diameter distribution and TEM images of (b) bare and (c) citrate stabilized samples NaBiF$_4$: 50%Tb^{3+}/0.1%Eu^{3+}.

Since crystal particles are regarded as spherical in dynamic light scattering (DLS) measurement, which is not always the case. Electron microscopy was acquired to corroborate the crystal particles size and characterize their morphology. The well-distributed crystal particles are shown in Fig. 4. (b) and (c) for bare and citrate stabilized samples NaBiF$_4$: 50%Tb^{3+}/0.1%Eu^{3+}, respectively. The irregular morphology is presented, and the average size is estimated to be 25 nm, which is close to the above results.

3.3. FT-IR spectrum

FT-IR spectrum is measured to further evidence the presence of sodium citrate as capping agent and provide the information of organic ligands bound to the surface of crystal particles, which is shown in Figure. 5.
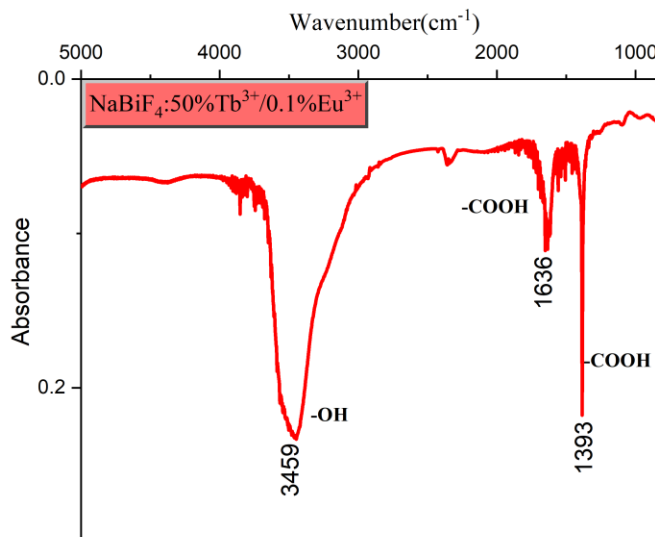
Figure. 5. FT-IR spectrum of citrate stabilized samples NaBiF$_4$: 50%Tb^{3+}/0.1%Eu^{3+}.

The interpretation of FTIR absorption bands has been done with reference spectra of known compounds. An absorption band at around 3459 cm^{-1} is assigned to the stretching vibration of hydroxyl group (O-H). Other bands at 1636 cm^{-1} and 1393 cm^{-1} are attributed to the stretching vibration of carboxyl group (COOH). This result further identifies the presence of organic groups on crystal particles surface, arising from such as water and sodium citrate.

3.4. Luminescence spectroscopy

3.4.1. NaBiF$_4$ singly doped with Tb^{3+} ions

The emission spectra and room temperature decay curves of NaBiF$_4$: x%Tb^{3+} (x = 5, 10, 25, 50, 70, 100) are shown in Figure. 6 (the inset is the excitation spectrum of NaBiF$_4$: 25%Tb).
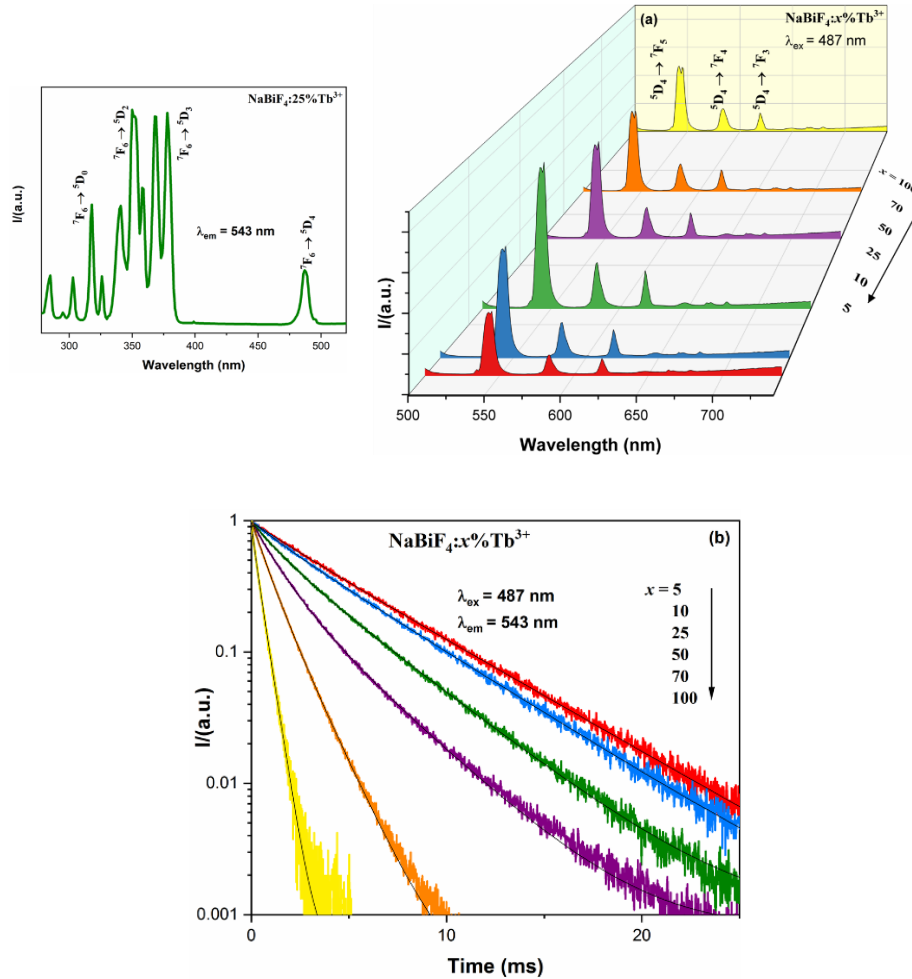
Figure. 6. The emission and excitation spectra and room temperature decay curves of NaBiF$_4$: x%Tb^{3+} (the solid lines in black color correspond to a double exponential decay model).

A representative excitation spectrum of NaBiF$_4$: 25%Tb is shown in Figure. 6(a), the characteristic of Tb^{3+} ion consists of several sharp lines upon emission at 543 nm. And the major peaks are located at 318, 352, 378 and 487 nm, which corresponds to $^{7}F_{6} \rightarrow {}^{5}D_{J}$ transitions (J = 0, 2, 3, 4), respectively. The emission spectra were measured upon excitation at 487 nm, and main peaks at 542 and 545, 584, 619 nm corresponding to the $^{5}D_{4} \rightarrow {}^{7}F_{J}$ (J = 5, 4, 3) transitions are

displayed for all samples, in which $^5D_4 \to {}^7F_5$ transition is always the strongest and accompanied by a certain degree of splitting owing to crystal field effect [97]. Besides, no changes for peak position with the increment of Tb^{3+} content. The green light can be observed by naked eyes for all samples.

As shown in Figure. 6(b), a double exponential model, which is compatible with a multisite emission (2 Tb^{3+} emitting sites), is adopted to fit all decay profiles of $^5D_4$ state of Tb^{3+} ions in a satisfactory way, and the average decay time calculated based on an certain equation [98] are of 4.98, 4.51, 3.46, 2.43, 1.16, 0.44 ms (when x = 5, 10, 25, 50, 70, 100), respectively. Clearly, a downward trend for decay time is presented as the percentage of Tb^{3+} increases. As above discussion, two crystal sites (1a and 1f) could be replaced by RE^{3+} in $NaBiF_4$ and both are of C_{3h} point symmetry. As the energy migration in $^5D_4$ subset of Tb^{3+} is significant when the percentage of Tb^{3+} is higher, a huge decline of decay time would happen until the energy reaching the quenching centers (concentration quenching). Because of the similar crystal phase between $NaTbF_4$ and $NaBiF_4$, the decrease of decay time result from the structure change can be neglected.

3.4.2. NaBiF₄ co-doped with Tb³⁺ and Eu³⁺ ions

The emission spectra and room temperature decay curves of $NaBiF_4$: $25\%Tb^{3+}/y\%Eu^{3+}$ (y = 5, 10, 20, 30) are shown in Figure. 7.
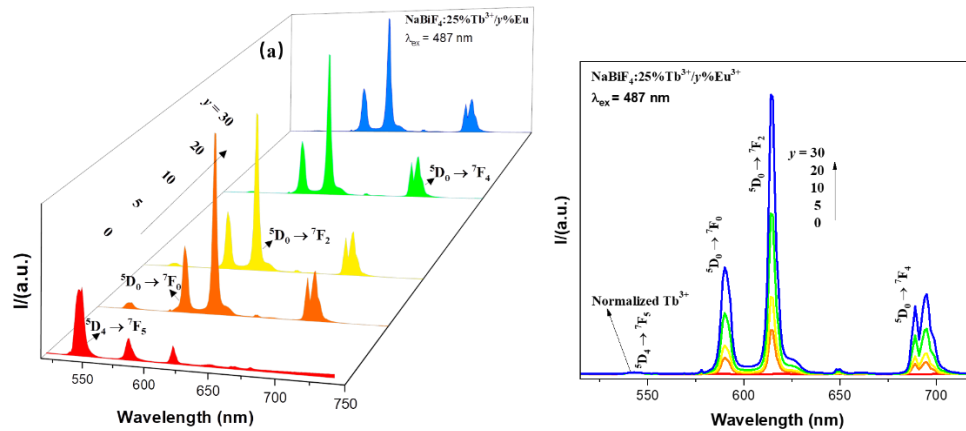
Figure. 7. (a) The emission spectra of $NaBiF_4$: $25\%Tb^{3+}/y\%Eu^{3+}$ (Relative emission spectra are normalized to the $^5D_4 \to {}^7F_5$ transition of Tb^{3+}).

As shown in Figure. 7(a), the $^5D_4 \to {}^7F_5$ transition of Tb^{3+} and $^5D_0 \to {}^7F_J$ (J = 1, 2, 4) transitions of Eu^{3+} are produced upon excitation at 487 nm (Tb^{3+} excited state). Similarly, the splitting of $^5D_0$

$\rightarrow {}^7F_4$ transition of Eu^{3+} corresponding to the peaks at 689 and 695 nm exists. What's more, the intensity of Tb^{3+} ($^5D_4 \rightarrow {}^7F_5$) decreased drastically with the increment of Eu^{3+} content. This suggests the presence of $Tb^{3+} \rightarrow Eu^{3+}$ energy transfer process, but the inevitable effects of quenching groups (O-H and C=O) also need to be considered. An upward trend could be seen for the intensity of Eu^{3+} with concentration in the relative emission spectra of $NaBiF_4$: $25\%Tb^{3+}/y\%Eu^{3+}$ (see figure. 7(a)). This result is highly agreed with the existence of $Tb^{3+} \rightarrow Eu^{3+}$ energy transfer process.

In Figure. 7(b), the room temperature decay curves of the $^5D_4$ excited state of Tb^{3+} are shown for $NaBiF_4$: $25\%Tb^{3+}/y\%Eu^{3+}$.
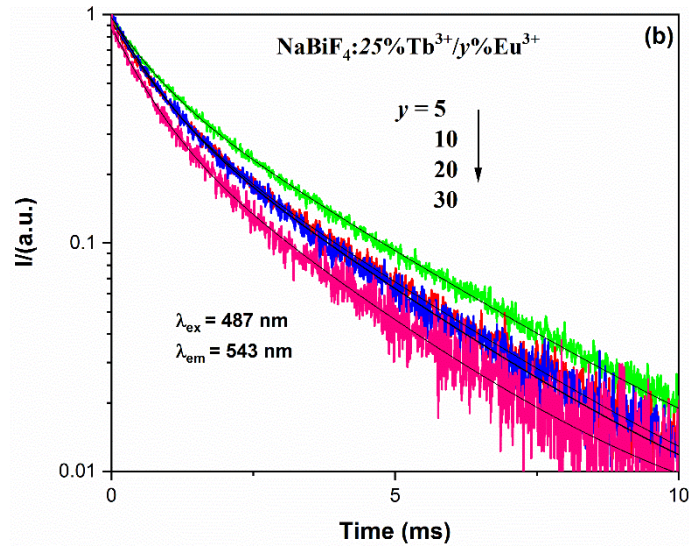
Figure. 7. (b) The room temperature decay curves of $NaBiF_4$: $25\%Tb^{3+}/y\%Eu^{3+}$ (the solid lines in black color correspond to a double exponential decay model).

The decay curve is an efficient tool to confirm the energy transfer process. It could be seen from the Figure. 7(b) that the decay profile of $^5D_4$ state of Tb^{3+} ions are fitted effectively with double exponential model, and an expected downward trend is indicated with decay constants 2.55, 2.24, 2.13, 1.91 ms (when $x = 5, 10, 20, 30$), respectively. In this case, it is assumed that the energy migration of Tb^{3+} and the energy transfer between Tb^{3+} and Eu^{3+} are comparable in efficiency. Furthermore, the energy transfer efficiency η_T can be calculated by the following equation [47]:

$$\eta_T = 1 - {}^{\tau_{Tb-Eu}}\big/_{\tau_{Tb}} \tag{1}$$

Here, τ_{Tb} and $\tau_{Tb\text{-}Eu}$ are the decay time in the absence and presence of Eu^{3+} ions, respectively. The obtained values of η_T are 26.3%, 35.3%, 38.4% and 44.8%, which increase with the concentration of Eu^{3+} ions. It is well known that the efficiency of energy transfer is related to the interionic distances between dopants, and higher concentration of dopant is helpful to shorten these distances and further increase the energy transfer possibility [36].

3.4.3 Citrate stabilized NaBiF$_4$: Tb^{3+} and NaBiF$_4$: Eu^{3+} in aqueous phase

The emission spectra of sodium citrate stabilized NaBiF$_4$: 25%Tb^{3+} and NaBiF$_4$: 20%Eu^{3+} in aqueous phase are shown in Figure. 8.
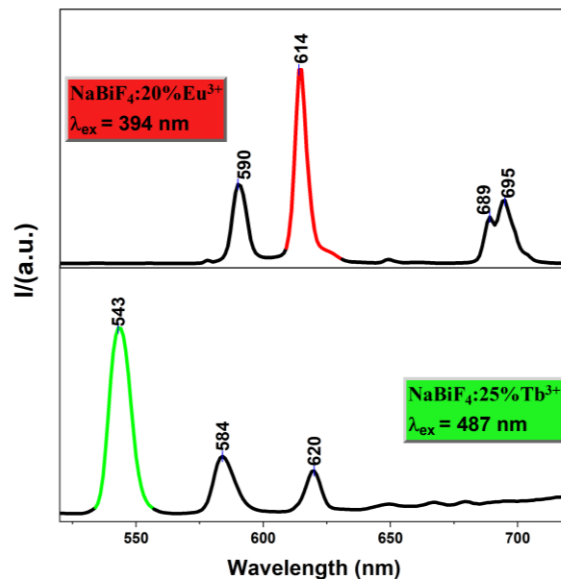
Figure. 8. The emission spectra of sodium citrate stabilized NaBiF$_4$: 25%Tb^{3+} and NaBiF$_4$: 20%Eu^{3+} in aqueous phase.

As shown in Figure. 8, the emission spectra of sodium citrate stabilized NaBiF$_4$: 25%Tb^{3+} and NaBiF$_4$: 20%Eu^{3+} in aqueous phase were measured upon excitation at 487 and 394 nm, respectively. The obtained characteristic emission peaks for Tb^{3+} (543, 584 and 620 nm) and Eu^{3+} (590, 614 and 689, 695 nm) are same to their solid counterparts. Besides, the spectra tend to be relatively broad due to the disorder [99]. A relatively weak intensity as can be expected with respect to the solid counterparts, which is mainly caused by the quenching of O-H vibrations probably bound to the surface of the materials (from water and CA). Since Tb^{3+} and Eu^{3+} can be easily coordinated by O-H groups in aqueous solution, the multiphonon relaxation process can

occur. Notably, the splitting of emission transitions of Tb^{3+} ($^5D_4 \rightarrow {}^7F_5$) and Eu^{3+} ($^5D_0 \rightarrow {}^7F_4$) in aqueous phase are not significant.

3.4.4 Citrate stabilized NaBiF$_4$: Tb^{3+}/Eu^{3+} and corresponding aqueous phase

The emission spectra for citrate stabilized NaBiF$_4$: 50%Tb^{3+}/0.1%Eu^{3+} in the solid state (hereinafter referred to as SC-Tb/Eu) and the corresponding aqueous phase (hereinafter referred to as SC-Tb/Eu aqueous phase) as well as bare (not stabilized by CA) samples upon excitation at 487 nm are shown in Figure. 9.
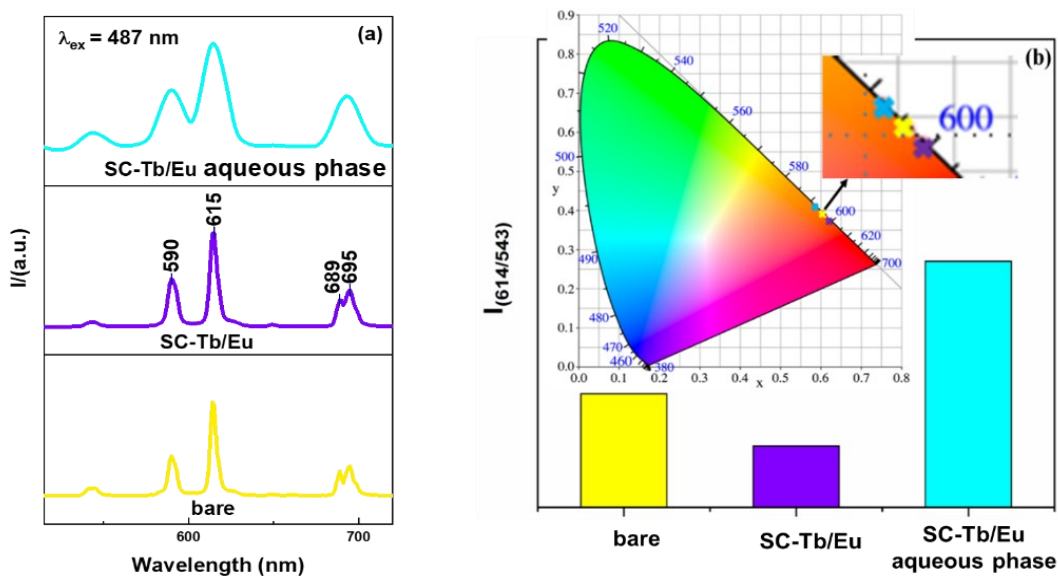
Figure. 9. (a) The emission spectra for citrate stabilized NaBiF$_4$: 50%Tb^{3+}/0.1%Eu^{3+} in solid (SC-Tb/Eu) and corresponding aqueous phase (SC-Tb/Eu aqueous phase)) as well as bare samples; (b) The histogram of the intensity ratio between the Tb^{3+} ($^5D_4 \rightarrow {}^7F_5$, 543 nm) and Eu^{3+} ($^5D_0 \rightarrow {}^7F_2$, 614 nm) transition. (The inset is the CIE chromaticity diagram of three samples).

Upon excitation at 487 nm, the characteristic emission bands related to Tb^{3+} and Eu^{3+} are both clearly detected for three samples. The similar splitting of peaks at 689, 695 nm of Eu^{3+} are took place to bare and SC-Tb/Eu samples yet disappear for SC-Tb/Eu aqueous phase, which probably results from the change of crystal field around nanoparticles. The intensity ratio between the Tb^{3+} ($^5D_4 \rightarrow {}^7F_5$, 543 nm) and Eu^{3+} ($^5D_0 \rightarrow {}^7F_2$, 614 nm) transition was calculated and shown in Figure. 9(b). It could be seen that this value for SC-Tb/Eu is smallest while biggest for SC-Tb/Eu aqueous phase, bare sample displays a middle value. Besides, the change of luminescence color is depicted

in the inset of Fig. 9(b). The change of intensity ratio deserves further investigation. It is important to underline that Eu^{3+}, if compared to Tb^{3+}, suffers from an intrinsic disadvantage of having a weaker luminescence intensity because of a smaller energy gap between the emitting state and the next lower energy level: $\Delta E(^5D_0 \rightarrow {}^7F_6)$ of ca. 12500 cm^{-1} of Eu^{3+} *versus* $\Delta E(^5D_4 \rightarrow {}^7F_0)$ of ca. 14750 cm^{-1} of Tb^{3+} resulting in enhanced non-radiative deactivation processes from X-H vibrators (X = O, N but also C) [101], [102]. Therefore, it is possible that quenching groups on surface can preferentially quench the Eu^{3+} luminescence. In conclusion, the relative Tb/Eu emission intensity is not only affected by the Tb-to-Eu energy transfer efficiency but also to the preferential effect of the multiphonon relaxation on the luminescence efficiency stemming from the two different ions.

As for the luminescence decay times and optical temperature sensing performance for the citrate capped compounds, it is currently under investigation and the results of this research will be presented in due course.

4. Conclusions

A series of $NaBiF_4$ doped with Tb^{3+} and Eu^{3+} ions have been successfully synthesized via a facile and fast route at room temperature. The energy transfer mechanisms $Tb^{3+} \rightarrow Eu^{3+}$ ions have been explored in bare samples. Besides, sodium citrate was added as capping agent and the luminescence spectroscopy of samples with surface modification have also been investigated. And the overall luminescence intensity can be quenched seriously for samples in aqueous phase, but the green light has increased intensity relative to red light. This is maybe due an enhanced non-radiative deactivation processes from O-H vibrators, in the case of Eu^{3+} ion. Besides, this material can have a good potential in optical thermometry.

Chapter 5

Design and properties of novel yellow emission persistent phosphor

(This part of work was made in a secondment in Professor Philippe Smet's lab, Department of Solid-State Science, University of Gent, Belgium)

Abstract：Being motivated by the purpose of developing a new persistent yellow emission phosphor, a novel design has been proposed by making use of an overlap between the blue emission spectrum of persistent phosphor $CaAl_2O_4$: Eu, Nd (CAO) and the excitation spectrum of classic yellow phosphor $Y_3Al_5O_{12}$: Ce (YAG). It involves the radiative energy transfer from CAO to YAG phosphor, in which CAO phosphor plays the role of donor and YAG is regarded as acceptor. The phosphor was deposited as a thin layer, transparent polymer PDMS (polydimethylsiloxane) was used to incorporate it. Two ways were devised to obtain the desired persistent yellow emission, one is to deposit the mixture of CAO and YAG as a single polymer layer (referred to as mixed layers), the other one is to stack the separate pure CAO and YAG polymer layers (referred to as stacked layers). The products have been investigated by persistent luminescence spectroscopy in order to evaluate the emission spectrum and intensity of the persistent luminescence. Results indicate such design could give rise to the prospective persistent yellow emission phosphor. A white emission, predictably, can also be attained in a proper way. This work would make a worthwhile contribution to the success of persistent phosphor emitting other colors.

Keywords: yellow emission, energy transfer, rare earth ion, persistent luminescence

1. Introduction

Within the field of luminescent materials, persistent phosphors have attracted an increasing research interest. Their distinguishing feature is to store energy during excitation and a continued emission of light after ending the excitation. Based on this impressive performance, the persistent phosphors have been utilized in multiple fields, such as displays [103], safety signage [104], optical storage [105]–[107], anti-counterfeiting [108], [109] and so on. The existing green and blue emitting phosphors are remarkably efficient, for instance, $SrAl_2O_4$: Eu, Dy as an important

benchmark has been found to display a long-lasting green afterglow and bright light [110]–[112]. Comparatively, there is a severe shortage of effective persistent phosphors in other emission colors. With a few exceptions such as the already existing red-emitting persistent phosphor CaS: Eu, Dy [113], the orange-emitting $Ca_2Si_5O_8$: Eu, Tm [114] and NIR-emitting $Zn_{1+x}Ga_{2-2x}Ge_xO_4$: Cr [115], [116] have been proved promising for bio-imaging research. There is hence a high need for persistent phosphors with other emission colors, which requires further efforts to explore novel multicolor persistent phosphors with innovative techniques.

Aluminate $CaAl_2O_4$: Eu, Nd (CAO) is widely known as a brilliant blue-emitting persistent phosphor [117]. The broad blue emission peaks at around 440 nm and corresponds to the $4f^6$ $5d{\rightarrow}4f^7$ transitions of Eu^{2+} upon the excitation of UV light. $Y_3Al_5O_{12}$:Ce (YAG) is a classic, non-persistent, yellow phosphor and has been applied successfully to commercial white LED [118], the emission with maximum at 558 nm stems from the 5d to 4f transition of Ce^{3+}, and its major excitation bands fall in the NUV and blue regions. There is a broad overlap between the blue emission of CAO and one of the YAG excitation bands, as shown in Figure. 1, which paves the way for the radiative energy transfer from CAO to YAG. Besides, provided that an excitation wavelength of 380 nm (marked with arrow in Figure. 1) is used, it is possible to exclusively excite CAO as this wavelength is not absorbed by the YAG phosphor. Therefore, a LED with a wavelength of 380 nm can be chosen to charge the persistent phosphors, which is beneficial for the verification that the persistent yellow luminescence is indeed originating from the energy transfer from CAO to YAG. In this way, the high quantum efficiency and broad spectrum of YAG can be used to create yellow light, while the persistent luminescence intensity only relies on the storage capacity of CAO.

Generally, the common energy transfer process is the so-called non-radiative energy transfer, which often happens between two centers, particularly, lanthanide ion pairs such as $Tb^{3+} \rightarrow Eu^{3+}$ [37], [39], $Tm^{3+} \rightarrow Tb^{3+}$ [62] as well as $Tb^{3+} \rightarrow Bi^{3+}$ [119] and also other transition metal ions. But the radiative energy transfer process is assumed in this work, which involves the deexcitation of donor ions by photon emission and the emitted photon is absorbed by acceptor ions, as reported in reference [120], [121]. Notably, the doping concentration of donor and acceptor is absolute key for both of energy transfer processes [36]. In reference [122] it is stated that depositing the phosphor as a polymer layer with a certain thickness is beneficial for the penetration depth of the excitation light, also the incorporation of phosphor into a transparent polymer can ensure the

phosphor is sufficiently spread out, so that the phosphor can be excited homogeneously and effectively. Inspired by these points, different designs have been proposed for the purpose of the obtaining desired persistent yellow emission. One is to deposit the mixture of CAO and YAG as a single polymer layer (referred to as mixed layers), and the other one is to stack the separate pure CAO and YAG polymer layers (referred to as stacked layers), the general schematic view is given in Figure. 2. For the stacked design, a persistent phosphor at the bottom and a color conversion layer on the top. The excitation occurs from the top, and the detection is also from the top, which is the situation in most applications. Besides, the combination of blue and yellow emission color in proper way can potentially yield white light, which greatly expands and enriches the prospective application fields.
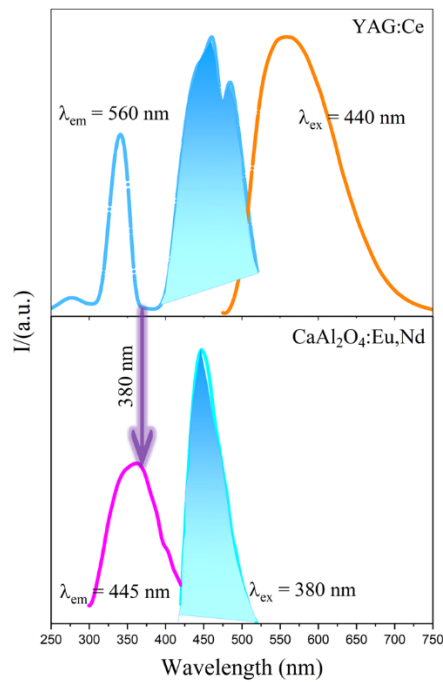
Figure. 1. The excitation and emission spectra of $CaAl_2O_4$: Eu, Nd and $Y_3Al_5O_{12}$: Ce phosphors.
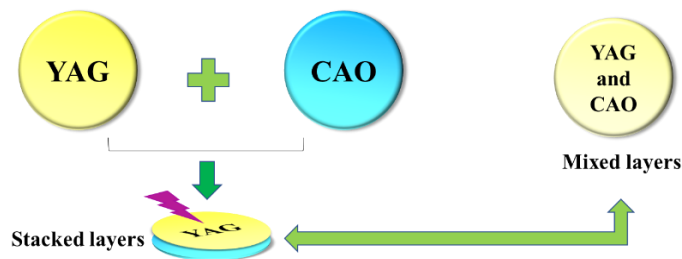
Figure. 2. The general schematic view of different designs.

2. Materials and Methods

Commercial $Y_3Al_5O_{12}$: Ce and $CaAl_2O_4$: Eu, Nd were purchased as raw materials. Transparent polymer PDMS was used to incorporate phosphors, which was fabricated by the mixture of DOWSIL [TM] 184 Silicone Elastomer Base (elastomer) and DOWSIL [TM] 184 Silicone Elastomer Curing agent (binding agent) with mass ratio 8:1. The preparation for polymer layer was preceded by thoroughly immersing the phosphor powders into PDMS polymer, the obtained precursor was subsequently loaded on a circular glass plate with a diameter of 18 mm. More details have been claimed in reference [122]. With the aim to realize optimal persistent yellow emission luminescence, a series of polymer layers were synthesized with various amounts of phosphor powders as shown in Table 1.

Table 1. The phosphor loading for all samples.

		Amount of YAG: Ce (mg)								
		324.0	271.6	223.1	162.0	116.0	81.0	40.5	19.4	0
Amount of $CaAl_2O_4$: Eu,Nd (mg)	324.0	648.0	595.6	547.1	486.0	440.0	405.0	364.5	343.4	324.0
	271.6	595.6	543.2	494.7	433.6	387.6	352.6	312.1	291.0	271.6
	223.1	547.1	494.7	446.2	385.1	339.1	304.1	263.6	242.5	223.1
	162.0	486.0	433.6	385.1	324.0	278.0	243.0	202.5	181.4	162.0
	116.0	440.0	387.6	339.1	278.0	232.0	197.0	156.5	135.4	116.0
	81.0	405.0	352.6	304.1	243.0	197.0	162.0	121.5	100.4	81.0
	40.5	364.5	312.1	263.6	202.5	156.5	121.5	81.0	59.9	40.5
	19.4	343.4	291.0	242.5	181.4	135.4	100.4	59.9	38.8	19.4
	0	324.0	271.6	223.1	162.0	116.0	81.0	40.5	19.4	0

The photoluminescence was recorded with Edinburgh FS920 spectrometer. Persistent luminescence was measured using AvaSpec SensLine instruments, connecting with LED (VL380-5-15) light source by optical fiber. The products were charged under the 380 nm excitation for 10 min, and then the spectra were collected with an integration time of 1s for 5 min after stopping charging. Excitation source and emission detection occurred on the same side of the samples. Calibration lamp was used for further intensity accuracy.

3. Results

The persistent luminescence of the stacked or mixed polymer layers will be composed of the violet-blue emission of CAO and the yellow emission of YAG, with the relative contribution depending on the composition and geometry of the polymer layers. The details are illustrated in Figure 3, in which Figure 3(a) is a display of mixed polymer layers, and Figure 3(b) is the design of stacked polymer layers with less loading amount of YAG while Figure 3(c) is stacked polymer layers with overloading of YAG.
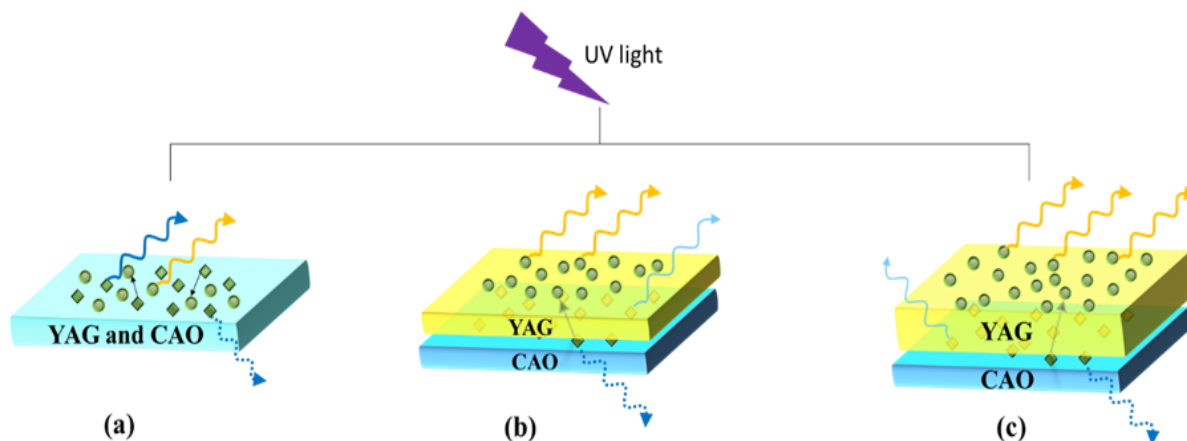
Figure 3. The illustration of the details for persistent luminescence (the arrow size represents the magnitude of the intensity, and the arrow with dash type means the light loss).

3.1 Yellow fraction investigation

To quantify the contribution of each component, a "yellow fraction" is determined, which is defined as the fraction of yellow emission with respect to the total number of emitted photons. The variation of yellow fraction within the quantity of phosphors is reflected in a scatter plot, which is shown in Figure 4. For the convenience of comparison, the identical scale of color bar is adopted.
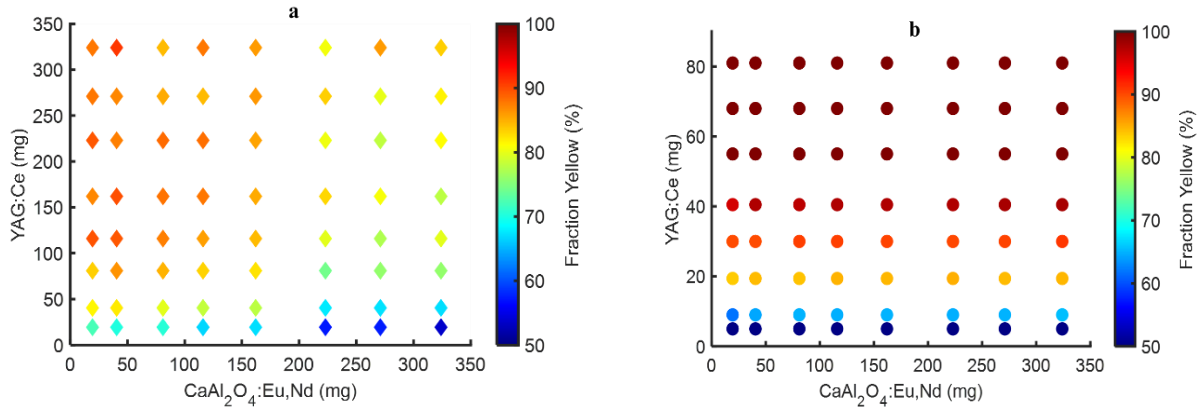
Figure 4. The scatter plot of yellow fraction for mixed (a) and stacked layers (b).

As shown in Figure 4(a), the values of yellow fraction increase with the amounts of YAG phosphors, but it decreases with the amounts of CAO. The red color corresponding to high values emerges after loading 81 mg of YAG, which indicates a large amount of YAG phosphors is demanded for strong persistent yellow emission. As shown in Figure 4(b), the values of yellow fraction increase with the amounts of YAG and remain similar after loading 55 mg of YAG, however, the values almost keep the same with the amounts of CAO, as can be expected for a stacked geometry. Notably, a red color for the data points, indicating a strong absorption of the CAO emission by the YAG phosphor, is observed with a YAG amount of 30 mg in this case, which means the design of stacked layers can efficiently fulfill the persistent yellow emission with much lower amount of YAG phosphors. Furthermore, it also allows to obtain a more saturated yellow emission color, as compared to the mixed design, as the amount of CAO emission can be suppressed.

3.2 Total intensity investigation

Total intensity is conclusively determined by the area of whole emission spectrum, namely the area sum of yellow and blue emission. Since the yellow fraction is heavily affected by the different designs as well as amounts of phosphors, the total intensity must be influenced in parallel.
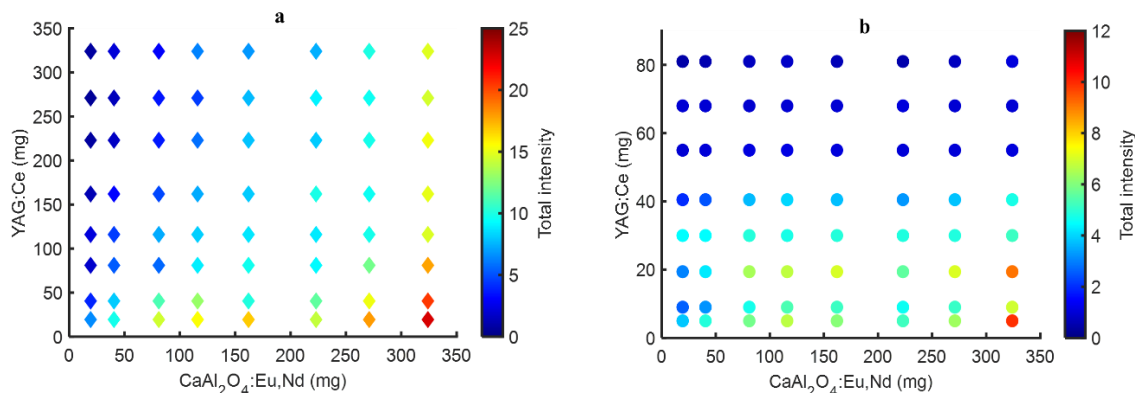
Figure 5. The scatter plot of total intensity for mixed (a) and stacked layers (b).

There is a huge difference in total intensity between mixed and stacked layers, so different scales of color bar are utilized here considering the perceiving clarity for color transform. The red color represents high values of total intensity. For the mixed design, Figure 5a, there are three regions. The top left part of the graph is characterized by a low emission intensity as the fraction of CAO within the total phosphor amount is very limited. Hence excitation light cannot reach the CAO particles very well, and the persistent luminescence intensity is low. For the bottom right part, the amount of CAO is high, leading to high emission intensities, but as there are only limited YAG particles mixed in the polymer layer, the probability for absorption of the CAO emission by YAG is low, leading to whitish emission (see Fig. 5a). If the aim is to have strong yellow emission, compositions slightly above the diagonal should be chosen. For the stacked design (Figure 5b) the emission intensity is obviously highest for the high CAO loading, provided that the YAG concentration is not too high, so that excitation light can reach the CAO particles at the bottom of the stack. Considering that a saturated yellow emission can be obtained for fairly low YAG concentrations, compositions in the lower left part of the graph are to be chosen.

3.3 Persistent luminescence properties

To gain further insight into the behavior resulting from YAG phosphors, the afterglow emission spectra of samples with a fixed loading of 324 mg CAO and different amounts of YAG for mixed and stacked layers are shown in Figure 6, respectively.

Figure 6. The afterglow emission spectra for mixed (a) and stacked layers (b) with a fixed loading of 324 mg CAO and different amounts of YAG. Both spectra are normalized by the area under the curves.

As Figure 6(a) and (b) shown, a growing amount of YAG phosphors facilitates the enhancement of persistent yellow emission, conversely, a diminishing of blue emission, which is an important implication of radiative energy transfer from CAO to YAG. The specified mixed and stacked layers marked with purple color in Figure 6(a) and (b) are taken as examples to intuitively measure their competitive advantages in persistent yellow emission, which because they were loaded with same amount of CAO (324 mg) and YAG (40.5 mg) phosphors and the mass ratio of CAO to YAG is constant and equal to 8. It can be observed that this mixed layer emits stronger blue emission rather than yellow, in turn, the stacked layer dominates yellow emission, which further demonstrates the design of stacked layers is much useful for developing a persistent phosphor with yellow emission. Care should be taken here concerning the shift of wavelength at 440 nm corresponding to the emission of pure CAO persistent phosphors, this blue shift arises after the adding of YAG phosphors and exhibits an increasing level with amount of YAG phosphors. Given the observation that the YAG excitation spectrum does not fully overlap with the CAO emission, the absorption probability for the longer emission wavelength side of CAO is higher and this is absorbed stronger, leading to a shift of the remaining CAO emission to shorter wavelengths.

3.4 The effect of Nd^{3+} absorption on emission spectra

The peculiar dip effect that is visible in afterglow emission spectra is an eye-catching puzzle. It's worth thinking about what that exactly means. It is reasonable suppose that its origin lies in

the Nd^{3+} absorption in accordance with the published paper [123]. To investigate the specific reason, the afterglow emission spectra for mixed and stacked layers with a fixed loading of 40.5 mg YAG and different amounts of CAO persistent phosphors are shown in Figure 7, respectively.
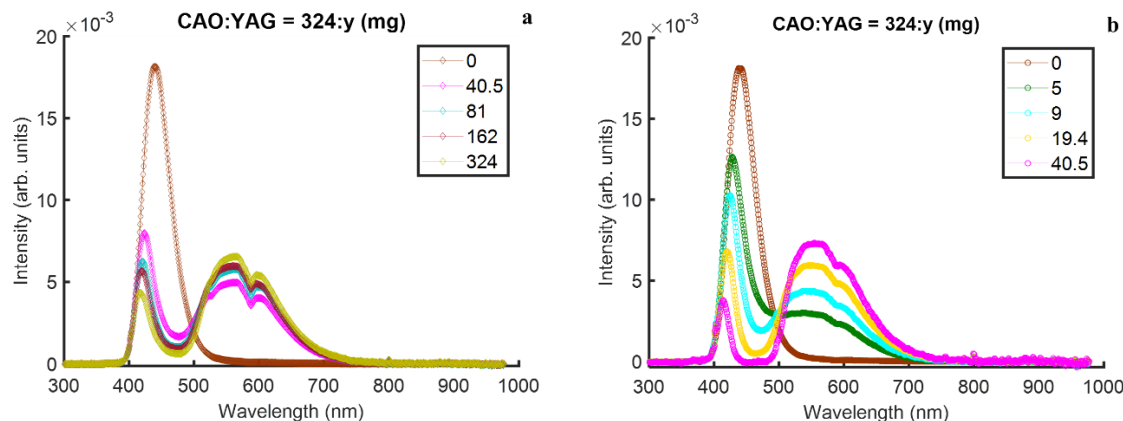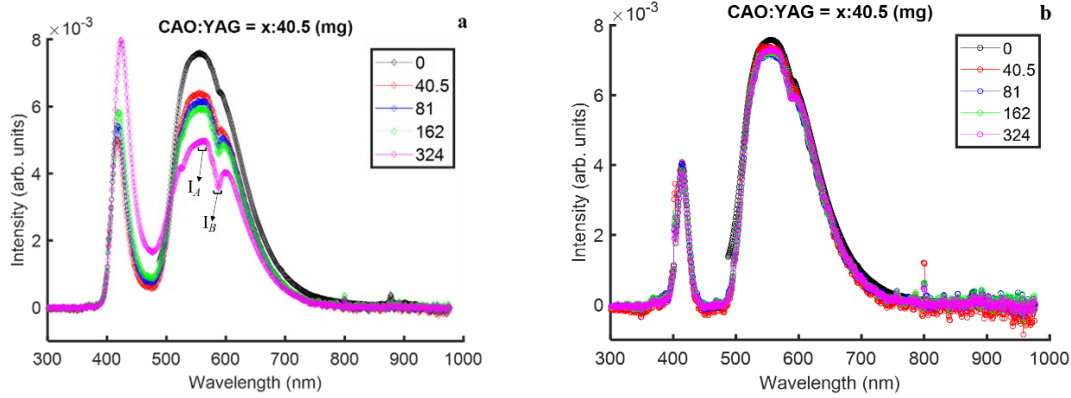

Figure 7. The afterglow emission spectra for mixed (a) and stacked layers (b) with a fixed loading of 40.5 mg YAG and different amounts of CAO. Both spectra are normalized by the area under the curve.

The Nd^{3+} ion is contained in CaAl$_2$O$_4$: Eu, Nd persistent phosphors, which acts as co-dopant to promote the formation of electron traps [124]. It possesses an intrinsic absorption band at around 588 nm corresponding to the $^4I_{9/2}$ - $^4G_{5/2}$+$^2G_{7/2}$ transition, which can cause the occurrence of reabsorption at the corresponding wavelength of YAG emission. As Figure 7(a) shows, the dip in spectrum becomes more severe with the amount of CAO phosphors, which because the amount of Nd^{3+} ion is also increasing along with numerous CAO phosphors. Thus, the above speculation is verified. However, the dip effect existed in stacked layers shown in Figure 7(b) is quite weak even can be neglected. In a mixed layer, a lot more emitted photons from YAG are directed towards the CAO particles, leading to scattering, but also to absorption by color centers, which can lead to optically stimulated detrapping - and/or by Nd^{3+} ions. For the stacked design, the main driver in the outcoupling of YAG emission, which is not directed out of the layers, is by scattering at the YAG particles, so that the Nd absorption dips are less prominent in the stacked design.

Besides, the average values of luminescence intensity corresponding to the wavelength range from 550 to 570 nm (where optimal persistent yellow emission resides in), and 585 to 590 nm (where the dip effect remains) are calculated and named with I_A and I_B, respectively, as shown in Figure 7. The value of I_B/I_A is a critical indicator to effectively assess the reabsorption of Nd^{3+} at

wavelength of 588 nm corresponding to the YAG emission, the result is shown in Figure 8. For the convenience of comparison, the identical scale of color bar is adopted.
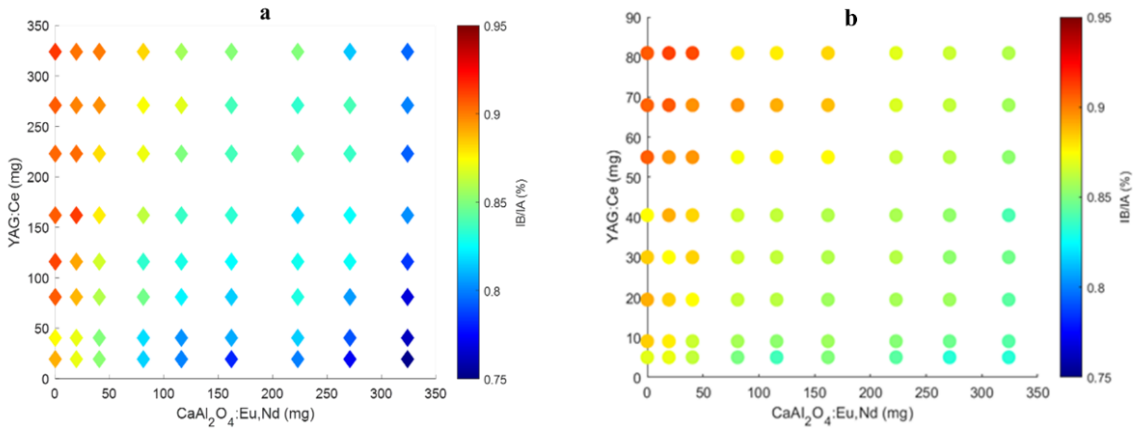
Figure. 8. The scatter plot of the values of I_B/I_A.

A red color signifies a higher value of I_B/I_A, and the higher value indicates the weaker reabsorption of Nd^{3+} at wavelength of 588 nm. As shown in Figure 8(a) and (b), higher values of I_B/I_A are observed for a series of pure YAG phosphors, which because the absence of CAO persistent phosphor. By contrast, a diminishing value of I_B/I_A is presented after adding different amount of the CAO, which implies the occurrence of reabsorption of Nd^{3+} ions at wavelength of 588 nm. Moreover, the lower value of I_B/I_A is marked with a shallow blue color in Figure 8(b) but a deep blue color in Figure 8(a). Consequently, it is reasonable to accept the fact that the design of stacked layers is benefit for reducing the probability of this reabsorption phenomenon.

3.5 The shift of peak wavelength of blue emission band

A blue shift of the maximum emission wavelength of CAO can be observed in Figure 6 for some samples. To understand this phenomenon, the peak wavelengths of blue emission band for all samples are shown in Figure 9. The maximum blue emission intensity is referred as index to describe the variation of wavelength resulting from the quantity of CAO and YAG phosphors.
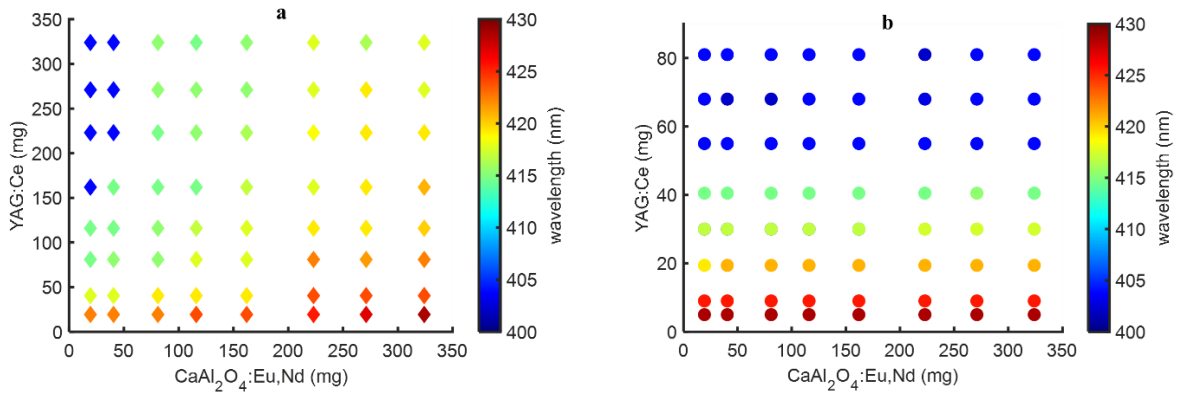
Figure 9. The scatter plot of the peak wavelength of blue emission band for mixed (a) and stacked layers (b).

An evolution of color from red to blue (or green) is shown in Figure 9(a) and (b) with the amount of YAG, which corresponds to a blue shift of the emission of pure CAO at 440 nm. This phenomenon is the consequence of a non-optimal overlap between the blue emission by CAO and the absorption by YAG, which can be seen from Figure 1. However, the impact of CAO on the peak wavelength of blue emission is different in Figure 9(a) and (b), a rather more subtle blue shift towards higher loading amount of CAO is displayed for stacked layers instead of a considerable shift for mixed layers.

3.6 The dependence upon luminescence intensity and charging time

All persistent luminescence spectra were collected after charging 10 min (marked with arrow in Figure. 10) with 380 nm LED light. However, given the inherent time dependency of the emission intensity of a persistent phosphor it raises a question about the effect of charging time on luminescence intensity which is explored here. The elected products (mixed layer with mass ratio CAO:YAG = 40.5:81 mg and stacked layer with mass ratio CAO:YAG = 116:19.4 mg) were charged with various time (1, 2, 8, 16, 32 and 60 minutes) to check the optimal charging time, and the dependence upon charging time and luminescence intensity is displayed in Figure 10.
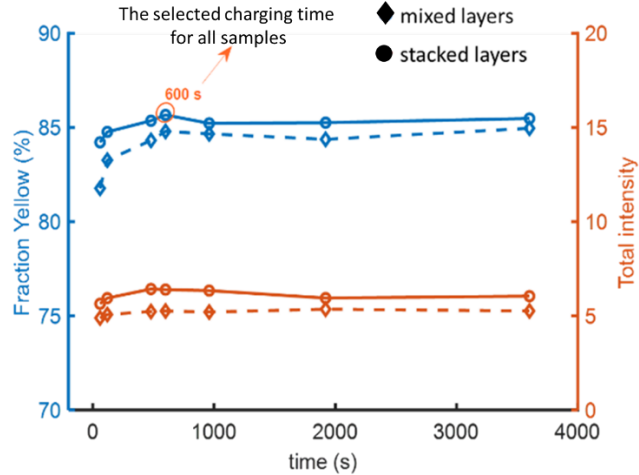
Figure 10. The yellow fraction and total intensity as a function of charging time for mixed (CAO:YAG = 40.5: 81 mg) and stacked layers (CAO:YAG = 116:19.4 mg).

An initial rise can be seen, it does not last long time and is succeeded by a fixed value with slight fluctuation after 10 min. As reported in reference [125], this first rising is assumed to be the particular "charging behavior" of CAO persistent phosphor, so the most obvious rising for mixed layers is anticipated due to the abundant absorption of excitation light. Besides, a slow rising in the stacked layers is probably also related to a lower excitation density at the level of the bottom CAO layer, due to scattering by the top YAG layer. A constant intensity with the increasing levels of charging time reveals the saturation of storage capacity of CAO. With the extension of charging time, a similar value of yellow fraction is kept at around 85% for mixed (CAO:YAG = 40.5:81 mg) and stacked layers (CAO:YAG = 116:19.4 mg). Meanwhile, a minor difference in total intensity between mixed and stacked layers is shown. This result demonstrates the possibility of achieving superior yellow emission as well as an eminent total intensity at the same time.

3.7 CIE chromaticity diagram

Except for the desirable yellow emission, the likelihood of white light is worthy of investigation here. Mixed layers with fixed CAO loading of 271 mg and different amount of YAG (19.4, 40.5, 81, 162 and 324 mg) are selected as preferable reference. Based on the recorded afterglow emission spectra, the Commission International de I'Eclairage (CIE) chromaticity diagram is depicted in Figure. 11. The variation of luminescence color from blue to white, then to yellow with the increasing amount of YAG is observed, which settles the probability of white light.
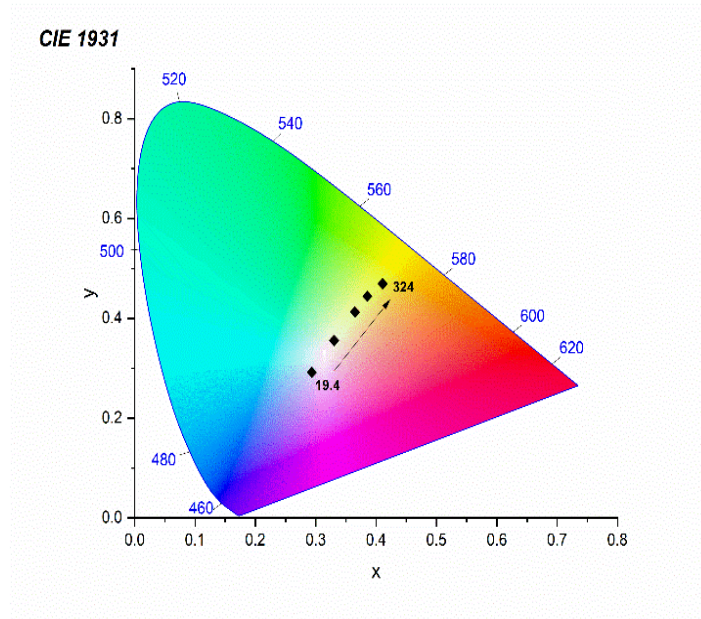
Figure 11. The CIE chromaticity diagram of mixed layers with fixed loading of 271 mg CAO and different amount of YAG based on the recorded afterglow emission spectra upon 380 nm excitation.

4. Discussion

It must be mentioned here, experimental or measurement errors always happens naturally, that's why a smooth transformation of colors is sometimes not presented in scatter plots. There is a limitation to the loading amount of phosphors powders. One reason is that a relatively rough surface can be found for the products with overloading amounts of phosphors due to the reduced solubility in a certain dosage of PDMS, which can eventually cause a part of light loss. Another reason is that the rising amount of phosphor powders is harmful for the penetration depth of excitation light, thus the emission intensity can be further affected.

The composition and geometry of the polymer layers are crucial factors for yielding ideal persistent yellow emission. The mixed layer features with sufficient absorption of excitation light, which is in favor of a profitable blue emission of CAO. The CAO phosphor performs the roles of donors as well as emitters, a high concentration of YAG makes an important contribution on increasing the chances of CAO emission reaching YAG. A strong blue emission can be monitored due to its direct exposure to detector. In the meantime, a considerable total intensity relating to

the blue and yellow emission could be foreseen. Besides, the white light persistent emission might suppose to be implemented by adjusting the mass ratio of CAO and YAG phosphors properly.

The way of stacking layers has several characteristics. On one hand, the UV light absorption by CAO persistent phosphors is impaired due to the extended irritation distance. In other words, the penetration depth of excitation light is relatively reduced. As a result, the CAO layer could not be excited efficiently, further the blue emission is correspondingly decreased. On the other hand, the relative concentration of CAO and YAG must be controlled in a strict way, otherwise an unfriendly shadow effect will be produced. In the case of a relatively less loading amount of YAG phosphors, CAO plays the major role of donors due to the way of stacking. The excitation light can also reach the CAO particles at the bottom of the stack, which ensures a good probability for absorption of the CAO emission by YAG. A significant enhancement of persistent yellow emission can be realized with the increase of YAG amount, and a saturation can be reached with a optimal amount of YAG. A continuous loading of YAG after the achievement of a saturated persistent yellow emission, which can bring about an unfavorable shadow effect. The penetration depth of excitation light is badly cut down, and the CAO phosphors almost play the sole role of donors. A nearly pure persistent yellow emission can be observed, but a considerable reduction of total intensity could not be neglected as well. Nevertheless, a remarkable yellow emission could take place in a proper stacking way.

5. Conclusions

An uncommon yellow emission persistent phosphor design using stacked phosphors has been proven to be feasible in this paper. As a result, the persistent yellow emission could be obtained by adding higher amount of YAG in mixed layers, and white emission is also possible. The distinguishing design of stacked layers could bring about a pleasing yellow emission with a relatively lower loading amount of YAG. Care should be taken to prevent the excessive loading amount of YAG in stacked layers, which is detrimental to the adequate exposure of CAO to excitation light due to an accompanying shadow effect.

Additionally, the blue shift of peak at 440 nm caused by the reabsorption of blue emission pertaining to CAO by YAG phosphors has been discovered. In like manner, a dip effect concerning the reabsorption of emission wavelength at 588 nm of YAG by CAO phosphors has been elucidated as the intrinsic absorption band corresponding to the $^4I_{9/2}$ - $^4G_{5/2}+^2G_{7/2}$ transition of Nd^{3+} ion. Moreover, the yellow fraction and total intensity as a function of charging time have

been investigated, the results reveal the saturation of storage capacity of CAO has been reached after charging time of 10 min. This work ultimately laid the foundations of persistent phosphor with other emission colors, has unique values.

Curriculum vitae

Xiaowu Hu

Personal Information:

Date of Birth: 15/5/1991

Nationality: People's Republic of China

Gender: Female

Address: Strada Le Grazie 15, Verona VR, Verona University, Verona City, Italy

Email: xiaowu.hu@univr.it

Education:

October 1st, 2019, ~ Present: PhD Candidate in Program "Nanoscience and Advanced Technologies", Verona University, Italy.

September 1st, 2016, ~ June 2019: Master Candidate in Inorganic Chemistry, School of Chemistry and Chemical Engineering, Hunan University, China.

September 1st, 2012 ~ June 2016: Bachelor of Applied Chemistry, School of Chemistry and Chemical Engineering, Shanxi Institute of Lv Liang, China.

Research Experiences:

May 1st ~ August 31st, 2022: Exchange PhD student, Optical properties of Persistence Phosphors.

Supervisor: Professor Philippe Smet, Department of Solid-State Science, University of Gent, Belgium.

October 1st, 2019, ~ Present: PhD Program, Synthesis and Luminescence spectroscopy of doped inorganic materials.

Supervisor: Professor Marco Bettinelli and Fabio Piccinelli, Department of Biotechnology, Verona University, Italy.

September 1st, 2016, ~ June 2019: Graduate Research, Lanthanide co-doped nanoparticles applied in Biomedical Sciences, Ceramics, Coating, and display device.

Supervisor: Professor Dongcai Guo, School of Chemistry and Chemical Engineering, Hunan University, China.

List of Publications

The investigations described in this thesis and related studies have been or will be published in the following papers:

Paterlini V, Hu X, Piccinelli F, et al. Energy transfer processes in $Sr_3Tb(PO_4)_3$ eulytite-type materials singly doped with Nd^{3+} and Sm^{3+}[J]. Optical Materials X, 2021, 11(2):100074.

Hu X, Piccinelli F, Bettinelli M. White light emission and energy transfer processes in $LaInO_3$ doped with Bi^{3+}, Tb^{3+} and Eu^{3+}[J]. Journal of Alloys and Compounds, 2022, 899:163344.

Energy transfer between Tb^{3+} and Tm^{3+} in eulytite materials of the type $Sr_3Ln(PO_4)_3$ [Ln=trivalent lanthanide ion(s)], Special issue of «Optics and Spectroscopy» dedicated to the anniversary of professor Marina Popova.

Energy transfer processes leading to NIR-to-red upconversion in ytterbium concentrated $Sr_3Yb_{0.98}Er_{0.02}(PO_4)_3$. (manuscript)

Energy transfer processes in $NaBiF_4$ doped with Tb^{3+} and Eu^{3+} and their luminescence properties in aqueous phase. (manuscript)

Design and properties of novel yellow emission persistence phosphor. (manuscript)

REFERENCE

[1] G. Blasse, B.C. Grabmaier Luminescent Materials Springer-Verlag (1994), Chapter 1.

[2] G. Blasse, B.C. Grabmaier Luminescent Materials Springer-Verlag (1994), Chapter 5.

[3] Dexter D . A Theory of Sensitized Luminescence in Solids. Journal of Chemical Physics, 1953, 21(5):836-850.

[4] Becker P C , Olsson N A , Simpson J R . Rare Earth Ions—Introductory Survey - ScienceDirect. Erbium-Doped Fiber Amplifiers, 1999:87-129.

[5] G. Blasse, B.C. Grabmaier Luminescent Materials Springer-Verlag (1994), Chapter 2.

[6] Elmanharawy M S , Eid A H , Kader A A . Spectra of europium-doped yttrium oxide and yttrium vanadate phosphors. Czechoslovak Journal of Physics B, 1978, 28(10):1164-1173.

[7] C. W , Struck, W. H , et al. Role of the charge-transfer states in feeding and thermally emptying the 5D states of Eu^{3+} in yttrium and lanthanum oxysulfide[J]. Journal of Luminescence, 1970.

[8] Levine A K , Palilla F C. A New, Highly Efficient Red-Emitting Cathodoluminescent Phosphor (YVO_4:Eu) for Color Television. Applied Physics Letters, 1964, 5(6):118-120.

[9] Weiyi Jia, Huabiao Yuan, Lizhu Lu, Huimin Liu, William M Yen, Crystal growth and characterization of Eu^{2+}, Dy^{3+}:$SrAl_2O_4$ and Eu^{2+}, Nd^{3+}:$CaAl_2O_4$ by the LHPG method, Journal of Crystal Growth, Volume 200, Issues 1–2, 1999, Pages 179-184.

[10] T. Aitasalo *et al.*, Persistent luminescence phenomena in materials doped with rare earth ions, *J. Solid State Chem.*, vol. 171, no. 1–2, pp. 114–122, 2003.

[11] Y. H. Lin, Z. Dang, Y. Deng, and C. W. Nan, Studies on mechanoluminescence from $SrAl_2O_4$:Eu, Dy phosphor, *Mater. Chem. Phys.*, vol. 80, no. 1, pp. 20–22, 2003.

[12] H. Nakagawa, K. Ebisu, M. Zhang, and M. Kitaura, Luminescence properties and afterglow in spinel crystals doped with trivalent Tb ions, *J. Lumin.*, vol. 102–103, no. SPEC, pp. 590–596, 2003.

[13] X.B. Chen, M.X. Li, K. Li, Y. Feng, S.Z. Bi, G.Y. Zhang, Y.G. Sun, Nonresonant up-conversion energy transfer directly achieved through a kind of coupling state quasi-clusters of rare-earth ions, Optics Communications, Volume 160, Issues 4–6, 1999, Pages 3.

[14] J. Qiu and Y. Kawamoto, Highly efficient blue up-conversion of Tm^{3+} in Nd^{3+}-Yb^{3+}-Tm^{3+} co-doped ZrF_4-based fluoride glass, *J. Fluor. Chem.*, vol. 110, no. 2, pp. 175–180, 2001.

[15] A. Tverjanovich, Y. G. Grigoriev, S. V. Degtyarev, A. V. Kurochkin, A. A. Man'shina, and Y. S. Tver'yanovich, Up-conversion fluorescence in Er-doped chalcogenide glasses based on GeS_2-Ga_2S_3 system, *J. Non. Cryst. Solids*, vol. 286, no. 1–2, pp. 89–92, 2001.

[16] I. Sokólska, S. Kück, G. Dominiak-Dzik, and M. Baba, The up-conversion processes in Ho^{3+} doped $LiTaO_3$, *J. Alloys Compd.*, vol. 323–324, pp. 273–278, 2001.

[17] Z.Y. Xie, J. Feng, J.S. Huang, S.Y. Liu, Y. Wang, J.C. Shen, Tuning of chromaticity in organic

multiple-quantum well white light emitting devices, Synthetic Metals, Volume 108, Issue 1, 2000, Pages 81-84.

[18] J. S. Kim, K. T. Lim, Y. S. Jeong, P. E. Jeon, J. C. Choi, and H. L. Park, Full-color $Ba_3MgSi_2O_8$:Eu^{2+}, Mn^{2+} phosphors for white-light-emitting diodes, *Solid State Commun.*, vol. 135, no. 1–2, pp. 21–24, 2005.

[19] J. A. Gonzalez-Ortega, E. M. Tejeda, N. Perea, G. A. Hirata, E. J. Bosze, and J. McKittrick, White light emission from rare earth activated yttrium silicate nanocrystalline powders and thin films, *Opt. Mater. (Amst).*, vol. 27, no. 7, pp. 1221–1227, 2005.

[20] A. Mills, Feature markrt analysis III-Vs review the advanced semiconductor magazine, vol 18-no. 3-APRIL 2005 Phosphors development for LED lighting, vol. 18, no. 3, pp. 32–34, 2005.

[21] F. K. Yam and Z. Hassan, Innovative advances in LED technology, *Microelectronics J.*, vol. 36, no. 2, pp. 129–137, 2005.

[22] P.M. Sommeling, H.C. Rieffe, J.A.M. van Roosmalen, A. Schönecker, J.M. Kroon, J.A. Wienke, A. Hinsch, Spectral response and IV-characterization of dye-sensitized nanocrystalline TiO_2 solar cells, Solar Energy Materials and Solar Cells, Volume 62, Issue 4.

[23] J. Wu, G. Xie, J. Lin, Z. Lan, M. Huang, and Y. Huang, Enhancing photoelectrical performance of dye-sensitized solar cell by doping with europium-doped yttria rare-earth oxide, *J. Power Sources*, vol. 195, no. 19, pp. 6937–6940, 2010.

[24] F. Zhao, Y. Liang, J. B. Lee, and S. J. Hwang, Applications of rare earth Tb^{3+}-Yb^{3+} co-doped down-conversion materials for solar cells, *Mater. Sci. Eng. B Solid-State Mater. Adv. Technol.*, vol. 248, no. October 2017, p. 114404, 2019.

[25] Dongyu Li, Yuxiao Wang, Xueru Zhang, Kun Yang, Lu Liu, Yinglin Song, Optical temperature sensor through infrared excited blue upconversion emission in Tm^{3+}/Yb^{3+} codoped Y_2O_3, Optics Communications, Volume 285, Issue 7, 2012, Pages 1925-1928.

[26] I. E. Kolesnikov, D. V. Mamonova, M. A. Kurochkin, V. A. Medvedev, and E. Y. Kolesnikov, Ratiometric dual-center Gd_2O_3:Tb^{3+}/Eu^{3+} nanothermometers with enhanced thermometric performances, *J. Alloys Compd.*, vol. 922, p. 166182, 2022.

[27] L. Wortmann, S. Suyari, T. Ube, M. Kamimura, and K. Soga, Tuning the thermal sensitivity of β-$NaYF_4$: Yb^{3+}, Ho^{3+}, Er^{3+} nanothermometers for optimal temperature sensing in OTN-NIR (NIR II/III) biological window, *J. Lumin.*, vol. 198, no. December 2017, pp. 236–242, 2018.

[28] A. F. Pereira, K. U. Kumar, W. F. Silva, W. Q. Santos, D. Jaque, and C. Jacinto, Yb^{3+}/Tm^{3+} co-doped $NaNbO_3$ nanocrystals as three-photon-excited luminescent nanothermometers, *Sensors Actuators, B Chem.*, vol. 213, pp. 65–71, 2015.

[29] T. Cao, T. Yang, Y. Gao, Y. Yang, H. Hu, and F. Li, Water-soluble $NaYF_4$:Yb/Er upconversion

nanophosphors: Synthesis, characteristics and application in bioimaging, *Inorg. Chem. Commun.*, vol. 13, no. 3, pp. 392–394, 2010.

[30] J. Zhou, Y. Sun, X. Du, L. Xiong, H. Hu, and F. Li, Dual-modality in vivo imaging using rare-earth nanocrystals with near-infrared to near-infrared (NIR-to-NIR) upconversion luminescence and magnetic resonance properties, *Biomaterials*, vol. 31, no. 12, pp. 3287–3295, 2010.

[31] Hongbo Zhu, Yaoxin Li, Runqi Qiu, Lei Shi, Weitai Wu, Shuiqin Zhou, Responsive fluorescent Bi_2O_3@PVA hybrid nanogels for temperature-sensing, dual-modal imaging, and drug delivery, Biomaterials, Volume 33, Issue 10, 2012, Pages 3058-3069.

[32] I. Khan, M. Shoaib, Norah Salem Alsaiari, S.M. Wabaidur, G. Rooh, N. Srisittipokakun, I. Ullah, J. Kaewkhao, Spectroscopic investigation of alkaline-earth borosilicate glasses doped with Sm_2O_3 for display devices application, Optik, Volume 269, 2022.

[33] Forster T . Intermolecular energy transfer and fluorescence. Ann.phys.leipzig, 1948, 2.

[34] D. L. Andrews, A unified theory of radiative and radiationless molecular energy transfer, *Chem. Phys.*, vol. 135, no. 2, pp. 195–201, 1989.

[35] B. Di Bartolo, Ed., *Energy Transfer Processes in Condensed Matter*, vol. 114. Boston, MA: Springer US, 1984.

[36] Irene Carrasco, Fabio Piccinelli, Marco Bettinelli, Luminescence of Tb-based materials doped with Eu^{3+}: case studies for energy transfer processes, Journal of Luminescence, Volume 189, 2017, Pages 71-77.

[37] M. Bettinelli, A. Speghini, F. Piccinelli, J. Ueda, and S. Tanabe, Energy transfer processes in $Sr_3Tb_{0.90}Eu_{0.10}(PO_4)_3$, *Opt. Mater. (Amst).*, vol. 33, no. 2, pp. 119–122, 2010.

[38] M. Bettinelli, F. Piccinelli, A. Speghini, J. Ueda, and S. Tanabe, Excited state dynamics and energy transfer rates in $Sr_3Tb_{0.90}Eu_{0.10}(PO_4)_3$, *J. Lumin.*, vol. 132, no. 1, pp. 27–29, Jan. 2012.

[39] V. Paterlini, F. Piccinelli, and M. Bettinelli, $Tb^{3+} \rightarrow Eu^{3+}$ energy transfer processes in eulytite $A_3Tb(PO_4)_3$ (A=Sr, Ba) and silico-carnotite $Ca_3Tb_2Z_3O_{12}$ (Z=Si, Ge) materials doped with Eu^{3+}, *Phys. B Condens. Matter*, vol. 575, Dec. 2019.

[40] A. N. Carneiro Neto *et al.*, Theoretical and Experimental Investigation of the $Tb^{3+} \rightarrow Eu^{3+}$+ Energy Transfer Mechanisms in Cubic $A_3Tb_{0.90}Eu_{0.10}(PO_4)_3$ (A = Sr, Ba) Materials, *J. Phys. Chem. C*, vol. 124, no. 18, pp. 10105–10116, May 2020.

[41] Blasse G . New compounds with eulytine structure: Crystal chemistry and luminescence. Journal of Solid State Chemistry, 1970, 2(1):27-30.

[42] Barbier J . Structural refinements of eulytite-type $Ca_3Bi(PO_4)_3$ and $Ba_3La(PO_4)_3$. Journal of Solid State Chemistry, 1992, 101(2):249-256.

[43] I.L. Botto, A correlation between crystallographic and spectroscopic data for some eulytite-type

phosphates containing bismuth Spectrochim. Acta, Part A, 43 (1987), pp. 119-121.

[44] K. Nakazawa and S. Shionoya, Energy transfer between trivalent rare-earth ions in inorganic solids, *J. Chem. Phys.*, vol. 47, no. 9, pp. 3267–3270, 1967.

[45] G. Blasse and B. C. Grabmaier, Luminescent Materials (Springer-Verlag, Berlin, Germany), 1994.

[46] Reisfeld R , Kalisky Y . Energy transfer between Bi^{3+} and Nd^{3+} in germanate glass. Chemical Physics Letters, 1977, 50(2):199-201.

[47] R. Reisfeld and N. Lieblich-Soffer, Energy transfer from UO_2^{2+} to Sm^{3+} in phosphate glass, *J. Solid State Chem.*, vol. 28, no. 3, pp. 391–395, 1979.

[48] Z. Yang, D. Xu, and J. Sun, Synthesis and luminescence properties of $Ba_3Lu(PO_4)_3$:Sm^{3+} phosphor for white light-emitting diodes, *Opt. Express*, vol. 25, no. 8, p. A391, Apr. 2017.

[49] L. qi Yao, G. hua Chen, T. Yang, Y. Luo, and Y. Yang, Optical properties and energy transfer in Tb^{3+}/Sm^{3+} co-doped Na_2O-CaO-P_2O_5-B_2O_3-ZrO_2 glasses, *J. Alloys Compd.*, vol. 692, pp. 346–350, 2017.

[50] A. Herrera *et al.*, Visible-NIR emission and structural properties of Sm^{3+} doped heavy-metal oxide glass with composition B_2O_3-PbO-Bi_2O_3-GeO_2, *J. Lumin.*, vol. 171, pp. 106–111, Mar. 2016.

[51] X. Sun, Z. Huang, Y. Guo, S. Zhou, and K. Liu, Tb^{3+}→Sm^{3+} energy transfer induced tunable luminescence in $Ba_3MgSi_2O_8$:Tb^{3+}/Sm^{3+} phosphors, *J. Lumin.*, vol. 219, Mar. 2020.

[52] W.T. Carnall, H. Crosswhite, H.M. Crosswhite, Energy level structure and transition probabilities in the spectra of the trivalent lanthanides in LaF_3 (Report ANL-78-XX-95, Argonne National Lab. (ANL), Argonne, IL (United States) 1978).

[53] R. D. Shannon, Revised effective ionic radii and systematic studies of interatomic distances in halides and chalcogenides, *Acta Crystallogr. Sect. A*, vol. 32, no. 5, pp. 751–767, 1976.

[54] K. Tonooka, K. Yamada, N. Kamata, and F. Maruyama, Role of the dipole-quadrupole interaction in fluorescence of RE glasses estimated by Monte Carlo simulation, *J. Lumin.*, vol. 60–61, no. C, pp. 864–866, 1994.

[55] Kreuzer K , Rockstroh J K , Sauerbruch T , et al. High-order multipole interaction in nanosecond Nd-Nd energy transfer. Journal of Luminescence, 1996, 69(4).

[56] W.G.J.H.M. van Sark, Meijerink A , Schropp R . Solar Spectrum Conversion for Photovoltaics Using Nanoparticles. InTech, 2012.

[57] Kuznetsov A S , A. Nikitin V K T , Shestakov M V , et al. Ultraviolet-driven white light generation from oxyfluoride glass co-doped with Tm^{3+}-Tb^{3+}-Eu^{3+}. Applied Physics Letters, 2013, 102(16):4-6.

[58] Song F , Ming C , An L , et al. Tm^{3+}/Tb^{3+}/Mn^{2+} tri-doped phosphate glass ceramic for enhanced white-light-emitting material. Materials Letters, 2011, 65(19-20):p.3140-3142.

[59] Yahiaoui Z , Hassairi M A , Dammak M , et al. Tunable luminescence and near white-light emission

of YPO$_4$:Eu^{3+},Tb^{3+},Tm^{3+} phosphors. Journal of Alloys & Compounds, 2018, 763:56-61.

[60] Zhang P , Huang X , Rui W , et al. Enhanced 1.4 μm emissions of Tm^{3+} via Tb^{3+} deactivation in (Gd$_{0.5}$Lu$_{0.5}$)$_2$SiO$_5$ crystal. Optical Materials Express, 2018, 8(3):668.

[61] Siyuan, Zhang, and, et al. Energy transfer between Tb^{3+} and Tm^{3+} ions in Tb$_x$Tm$_y$Y$_{1-x-y}$P$_5$O$_{14}$ crystals. Journal of Luminescence, 1988.

[62] Bettinelli M , Ingletto G . Energy transfer between Tb^{3+} and Tm^{3+} in a lead silicate glass. Journal of Luminescence, 1989, 43(2):115-119.

[63] M. Bettinelli, F.S. Ermeneux, R. Moncorge, E. Cavalli. Fluorescence dynamics of YVO$_4$:Tm^{3+}, YVO$_4$:Tm^{3+}, Tb^{3+} and YVO$_4$:Tm^{3+}, Ho^{3+} crysta J. Phys. C: Condensed Matter, 10, 8207 (1998).

[64] T Vega-Durán, L A Díaz-Torres, Meneses-Nava M A , et al. Optimal co-doping concentrations and dynamics of energy transfer processes for Tm^{3+}-Tb^{3+}and Tm^{3+}-Eu^{3+} in LiYF$_4$ crystal hosts. Journal of Physics D: Applied Physics, 2001.

[65] L. Huang, Z. Hong, J. Zhuang. Chinese Journal of Lasers B (English Edition), 10, 450 (2001).

[66] J. Pisarska, M. Slezok, M. Zelechower, S. Serkowski, T. Goryczka, W.A. Pisarski, W. Ryba-Romanowski. Proc. SPIE --- The International Society for Optical Engineering, 5028, 181 (2003).

[67] Dong J L , Heo J , Park S H . Energy transfer and 1.48 μm emission properties in chalcohalide glasses doped with Tm^{3+} and Tb^{3+}. Journal of Non-Crystalline Solids, 2003, 331(1-3):184-189.

[68] Shen S , Jha A , Zhang E , et al. Tm^{3+}-Ho^{3+} and Tm^{3+}-Tb^{3+} energy transfer in tellurite glass. Journal of Luminescence, 2007, 126(2):434-440.

[69] Yang H , Dai Z , Zu N . Dynamics of excited state relaxation and frequency upconversion in Tm^{3+} and Tm^{3+}/Tb^{3+} doped ZBLAN glass. Journal of Non-Crystalline Solids, 2008, 354(15-16):1796-1800.

[70] Sasikala, T, Moorthy R , et al. Photoluminescence properties of singly doped Tm^{3+} and co-doped Tm^{3+}/Tb^{3+} ions in tellurite glasses. OPTICS COMMUNICATIONS, 2014.

[71] A. Castañeda-Miranda, V. M. Castaño. Modeling of the Dynamics of Non-radiative Energy Transferin Tm^{3+}, Tb^{3+}: LiYF$_4$-Based Electronic Materials. Journal of Electronic Materials, 2017.

[72] Guo J , Zhao L , Tang Q, et al. Spectral study on energy transfer of the LiMgPO$_4$ phosphor doped with Tm^{3+} and Tb^{3+}. Journal of Luminescence, 2020, 228(3):117613.

[73] Wu X , Du L , Zheng Y, et al. Tm^{3+}→Tb^{3+} energy transfer induced color-tunable in double-doped LiLaSiO$_4$ phosphors. Journal of Luminescence, 2021, 235:118027.

[74] V. Paterlini, X. Hu, F. Piccinelli, and M. Bettinelli, Energy transfer processes in Sr$_3$Tb(PO$_4$)$_3$ eulytite-type materials singly doped with Nd^{3+} and Sm^{3+}, *Opt. Mater. X*, vol. 11, 2021.

[75] Chrysochoos J , Qusti A H . Intense blue luminescence spectra and lifetimes of Tm^{3+} in POCl$_3$:SnCl$_4$. Journal of the Less Common Metals, 1986, 126(none):161-167.

[76] Chrysochoos J , Qusti A H . Cross-relaxation of the ^{1}G$_4$ state of Tm^{3+} in POCl$_3$:SnCl$_4$. Journal of The

Less-Common Metals, 1989, 148(1-2):253-257.

[77] Ki-Soo, Lim, and, *et al*. Optical spectroscopy of thulium-doped oxyfluoroborate glass. Journal of Alloys and Compounds, 2004.

[78] P. Solarz and W. Ryba-Romanowski, Energy transfer processes in $K_5Li_2GdF_{10}$:Eu, Pr, *Radiat. Meas.*, vol. 42, no. 4–5, pp. 759–762, 2007.

[79] I. Carrasco, K. Bartosiewicz, M. Nikl, F. Piccinelli, and M. Bettinelli, Energy transfer processes in $Ca_3Tb_{2-x}Eu_xSi_3O_{12}$ (x = 0-2), *Opt. Mater. (Amst).*, vol. 48, pp. 252–257, 2015.

[80] X. Liu and J. Lin, Synthesis and luminescent properties of $LaInO_3$: RE^{3+} (RE = Sm, Pr and Tb) nanocrystalline phosphors for field emission displays, *Solid State Sci.*, vol. 11, no. 12, pp. 2030–2036, 2009.

[81] J. Liu, Xiaoming ; Yan, Liushui ; Lin, Tunable Photoluminescence and Cathodoluminescence Properties of Eu^{3+}-Doped $LaInO_3$ Nanocrystalline Phosphors, *J. Electrochem. Soc. Vol. 156, Issue 1, pp. P1*.

[82] G. Singh, A. S. Anand, R. Selvamani, V. S. Tiwari, and A. K. Karnal, THE LUMINESCENCE OF Bi^{3+} IN $LaInO_3$, AND SOME OTHER PEROVSKITES, *Mater. Res. Bull.*, vol. 167, no. il, pp. 61–65, 2019.

[83] A. M. Srivastava *et al.*, Spectroscopy of Mn^{4+} in orthorhombic perovskite, $LaInO_3$, *J. Lumin.*, vol. 206, pp. 398–402, 2019.

[84] N. A. M. Saeed, E. Coetsee, R. E. Kroon, M. Bettinelli, and H. C. Swart, Photoluminescence of Bi^{3+} doped in YOF phosphor as an activator, *Opt. Mater. (Amst).*, vol. 119, 2021.

[85] C. S. Kamal *et al.*, Unravelling the energy transfer mechanism in bismuth co-activation of $LaInO_3$:Sm^{3+}/Ho^{3+} nanophosphor for color-tunable luminescence, *RSC Adv.*, vol. 7, no. 16, pp. 9724–9731, 201.

[86] Han, B., Zhang, J., Li, P.J. et al. $KBaBP_2O_8$:Tm^{3+}: a novel blue-emitting phosphor with high color purity. Jetp Lett. 99, 561–564 (2014).

[87] A. Tang, D. Zhang, L. Yang, and X. Wang, Luminescent properties of a new red-emitting phosphor based on $LaInO_3$ for LED, *Optoelectron. Adv. Mater. Rapid Commun.*, vol. 5, no. 10, pp. 1031–1034, 2011.

[88] P. Lei *et al.*, Ultrafast Synthesis of Novel Hexagonal Phase $NaBiF_4$ Upconversion Nanoparticles at Room Temperature, *Adv. Mater.*, vol. 29, no. 22, 2017.

[89] P. Du, X. Huang, and J. S. Yu, Facile synthesis of bifunctional Eu^{3+}-activated $NaBiF_4$ red-emitting nanoparticles for simultaneous white light-emitting diodes and field emission displays, *Chem. Eng. J.*, vol. 337, pp. 91–100, 2018.

[90] Du, Peng and Hua, Yongbin and Yu, Jae Su, Room-temperature synthesis of near-ultraviolet light-

excited Tb^{3+}-doped NaBiF$_4$ green-emitting nanoparticles for solid-state lighting, RSC Adv, 2018.

[91] P. Lei *et al.*, Benefits of surfactant effects on quantum efficiency enhancement and temperature sensing behavior of NaBiF$_4$ upconversion nanoparticles, *J. Mater. Chem. C*, vol. 5, no. 37, pp. 9659–9665, 2017.

[92] Y. Guo *et al.*, The enhanced up-conversion green by Yb-Mn dimer in NaBiF$_4$:Yb^{3+}/Er^{3+}/Mn^{2+} for optical fiber temperature sensor, *J. Alloys Compd.*, vol. 888, 2021.

[93] Xia W , Li L , Yang P , et al. Synthesis of color-tunable Sr$_8$MgLa(PO$_4$)$_7$:Eu^{3+}/Tb^{3+} phosphors for designing dual-model thermometers. Journal of Luminescence: An Interdisciplinary Journal of Research on Excited State Processes in Condensed Matter, 2021.

[94] D. V. M. Paiva *et al.*, Investigation on luminescence based optical temperature sensing behavior of Sr$_3$MOO$_6$:Eu^{3+}/Tb^{3+}, *Optik (Stuttg).*, vol. 246, 2021.

[95] P. Lei and Y. Zhang, Hollow upconversion nanoparticles: Synthesis and luminescence in comparison with their solid counterparts, *Chem. Eng. J.*, vol. 426, 2021.

[96] Y. Chen, J. Xiang, M. Jin, Z. Zhang, and C. Guo, Anhydrous synthesis and organic waterproof skin of NaBiF$_4$: Yb^{3+}/Er^{3+} microspheres, *Opt. Mater. (Amst).*, vol. 112, 2021.

[97] Jiang X , Cong C , Wei F , et al. Nd^{3+}-doped LiYF$_4$ nanocrystals for bio-imaging in the second near-infrared window. Journal of Materials Chemistry B, 2015, 4.

[98] J. W. Chung, J. Y. Park, and H. K. Yang, Ultra-fast synthesis and photoluminescence properties of red-emitting NaBiF$_4$:Eu^{3+} nanophosphors by various NH$_4$F concentrations, *J. Lumin.*, vol. 211, pp. 176–182, 2019.

[99] M. G. Ivanov, I. V. Krutikova, U. Kynast, M. Lezhnina, and I. S. Puzyrev, Laser-synthesized Y$_2$O$_3$:Eu^{3+} nanophosphors and their stabilization in water suspensions, *Opt. Mater. (Amst).*, vol. 74, pp. 67–75, 2017.

[100] T. Wang and H. Li, A simple and green strategy for preparing luminescent Tb^{3+} complex-based nanocomposite with stable luminescence in water, *Mater. Res. Bull.*, vol. 93, pp. 28–34, 2017.

[101] K. Lunstroot *et al.*, Visible and near-infrared emission by samarium(III)-containing ionic liquid mixtures, *Inorg. Chem.*, vol. 48, no. 7, pp. 3018–3026, 2009.

[102] E. Kreidt, L. Arrico, F. Zinna, L. Di Bari, and M. Seitz, Circularly Polarised Luminescence in Enantiopure Samarium and Europium Cryptates, *Chem. - A Eur. J.*, vol. 24, no. 51, pp. 13556–13564, 2018.

[103] B. Verma, R. N. Baghel, D. P. Bisen, N. Brahme, and V. Jena, Microstructural, luminescence properties and Judd-Ofelt analysis of Eu^{3+} activated K$_2$Zr(PO$_4$)$_2$ phosphor for lighting and display applications, *Opt. Mater. (Amst).*, vol. 129, Jul. 2022.

[104] L. Xu, Z. Chen, X. Li, and F. Xiao, Performance, environmental impact and cost analysis of marking

materials in pavement engineering, the-state-of-art, *Journal of Cleaner Production*, vol. 294. Elsevier Ltd, Apr. 20, 2021.

[105] J. Zhang, L. Yuan, Y. Jin, H. Wu, L. Chen, and Y. Hu, Regulating electron traps of Eu^{2+}-doped $Ba_{1.6}Ca_{0.4}SiO_4$ persistent and optically stimulated luminescence phosphor toward optical data storage, *J. Lumin.*, vol. 241, Jan. 2022.

[106] R. Hu, Y. Zhang, Y. Zhao, X. Wang, G. Li, and C. Wang, UV–Vis-NIR broadband-photostimulated luminescence of $LiTaO_3$:Bi^{3+} long-persistent phosphor and the optical storage properties, *Chem. Eng. J.*, vol. 392, Jul. 2020.

[107] X. Lai, Z. Fang, J. Zhang, B. Wang, W. Zhu, and R. Zhang, Structure and luminescence properties of Ce^{3+}-activated $BaLu_2Al_2Ga_2SiO_{12}$ persistent phosphors for optical information storage, *Opt. Mater. (Amst).*, vol. 120, Oct. 2021.

[108] M. Zhang *et al.*, A novel differential display material: $K_3LuSi_2O_7$: Tb^{3+}/Bi^{3+} phosphor with thermal response, time resolution and luminescence color for optical anti-counterfeiting, *J. Colloid Interface Sci.*, vol. 608, pp. 758–767, Feb. 2022.

[109] J. Wang *et al.*, Long persistent luminescence property of green emitting $Sr_3Ga_4O_9$: Tb^{3+} phosphor for anti-counterfeiting application, *J. Lumin.*, vol. 250, Oct. 2022.

[110] Matsuzawa T , Aoki Y , Takeuchi N , et al. A New Long Phosphorescent Phosphor with High Brightness, $SrAl_2O_4$:Eu^{2+},Dy^{3+}. Journal of the Electrochemical Society, 1996, 143.

[111] X. Hu *et al.*, Preparation and properties of Eu and Dy co-doped strontium aluminate long afterglow nanomaterials, *Ceram. Int.*, vol. 44, no. 7, pp. 7535–7544, May 2018.

[112] Jia W , Lu L , Liu H , et al. Phosphorescent dynamics in $SrAl_2O_4$: Eu^{2+}, Dy^{3+} single crystal fibers. Journal of Luminescence: An Interdisciplinary Journal of Research on Excited State Processes in Condensed Matter, 1998:76/77.

[113] D. C. Rodríguez Burbano, S. K. Sharma, P. Dorenbos, B. Viana, and J. A. Capobianco, Persistent and Photostimulated Red Emission in CaS: Eu^{2+},Dy^{3+} Nanophosphors, *Adv. Opt. Mater.*, vol. 3, no. 4, pp. 551–557, Apr. 2015.

[114] K. Van den Eeckhout, P. F. Smet, and D. Poelman, Luminescent afterglow behavior in the $M_2Si_5N_8$: Eu family (M = Ca, Sr, Ba), *Materials (Basel).*, vol. 4, no. 6, pp. 980–990, 2011.

[115] S. Das, S. K. Sharma, and J. Manam, Near infrared emitting Cr^{3+} doped $Zn_3Ga_2Ge_2O_{10}$ long persistent phosphor for night vision surveillance and anti-counterfeit applications, *Ceram. Int.*, vol. 48, no. 1, pp. 824–831, Jan. 2022.

[116] Z. Pan *et al.*, Facilitating Low-Energy Activation in the Near-Infrared Persistent Luminescent Phosphor $Zn_{1+x}Ga_{2-2x}Sn_xO_4$:Cr^{3+} via Crystal Field Strength Modulations, *J. Phys. Chem. C*, vol. 124, no. 15, pp. 8347–8358, 2020.

[117] Katsumata T, Sasajima K , Matsuzawa T, et al. Growth and characteristics of long persistent $SrAl_2O_4$- and $CaAl_2O_4$-based phosphor crystals by a floating zone technique. Journal of Crystal Growth, 1998(3):183.

[118] G. W. Berkstresser and J. Shmulovich and T. C. D. Huo and G. Matulis. Growth Parameter Optimization and Tb^{3+} Sensitization of Ce^{3+} Activated $Y_3Al_5O_{12}$ Phosphor, vol 134, no.10, 1987.

[119] X. Hu, F. Piccinelli, and M. Bettinelli, White light emission and energy transfer processes in $LaInO_3$ doped with Bi^{3+}, Tb^{3+} and Eu^{3+}, *J. Alloys Compd.*, vol. 899, Apr. 2022.

[120] Y. L. and Q. Q. Wenbo Chen Yuhua Wang, Wei Zeng, Shaochun Han, Gen Li, Haijie Guo, Long persistent composite phosphor $CaAl_2O_4$:Eu^{2+}, Nd^{3+}/$Y_3Al_5O_{12}$:Ce^{3+}: A novel strategy to design the multicolor of persistent luminescence, *J. Mater. Chem. C*, vol. 3, pp. 10715–10722, 2015.

[121] Y. Xia, H. Ou, W. Li, G. Han, and Z. Li, Efficient blue to red afterglow tuning in a binary nanocomposite plastic film, *Nanomaterials*, vol. 8, no. 4, pp. 1–11, 2018.

[122] D. Van der Heggen, J. J. Joos, D. C. Rodríguez Burbano, J. A. Capobianco, and P. F. Smet, Counting the photons: Determining the absolute storage capacity of persistent phosphors, *Materials (Basel).*, vol. 10, no. 8, Jul. 2017.

[123] J. Ueda, T. Shinoda, and S. Tanabe, Photochromism and near-infrared persistent luminescence in Eu^{2+}-Nd^{3+}-co-doped $CaAl_2O_4$ ceramics, *Opt. Mater. Express*, vol. 3, no. 6, p. 787, Jun. 2013.

[124] Hajime, Yamamoto, and, et al. Mechanism of long phosphorescence of $SrAl_2O_4$:Eu^{2+}, Dy^{3+} and $CaAl_2O_4$:Eu^{2+}, Nd^{3+}. Journal of Luminescence, 1997.

[125] J. Botterman, J. J. Joos, and P. F. Smet, Trapping and detrapping in $SrAl_2O_4$:Eu,Dy persistent phosphors: Influence of excitation wavelength and temperature, *Phys. Rev. B - Condens. Matter Mater. Phys.*, vol. 90, no. 8, Aug. 2014.